

# **Dissociation properties of biomolecules under an externally applied force**

**Dissertation**

**Faculty of Physics  
Ludwig-Maximilians-Universität München**



**presented by**

**Julia Louise Zimmermann**

**14 February 2008**

---

First referee: Prof. Dr. Hermann E. Gaub  
Second referee: Prof. Dr. Joachim Rädler  
Viva voce: 17 April 2008

---

## Table of contents

<b>1 Summary</b> .....	5
<b>2 Introduction</b> .....	7
<b>3 Force spectroscopy</b> .....	9
3.1 Theory .....	9
3.1.1 Theory of molecular interactions in the absence of an external force .....	9
3.1.2 Theory of molecular interactions in the presence of an external force .....	12
3.2 Techniques for the application and detection of molecular forces .....	17
3.2.1 Overview .....	17
3.2.2 The atomic force microscope (AFM).....	22
<b>4 Site-specific and covalent immobilization of biomolecules to surfaces</b> .....	24
<b>5 Analysis of different types of biological interactions with the AFM</b> ...	26
5.1 DNA-DNA interactions .....	26
5.1.1 Background and state of the art .....	26
5.1.2 Summary of the performed measurements .....	32
5.1.2.1 Detection of the B-S transition .....	32
5.1.2.2 Measurement of repetitive sequences .....	32
5.2 Antibody-antigen interactions .....	34
5.2.1 Background and state of the art .....	34
5.2.2 Summary of the performed measurements .....	37
5.2.2.1 Analysis of the influence of mutations on the binding potential .....	37
5.2.2.2 Analysis of the influence of the direction of the applied force on the binding potential .....	37
<b>6 Applications</b> .....	39
6.1 Model system for the force-based manipulation of the enzymatic activity of Lipase B from <i>Candida antarctica</i> (CalB).....	39
6.2 Single-molecule cut-and-paste surface assembly .....	42
<b>7 References</b> .....	45

---

<b>8 Publications</b> .....	53
8.1 “Force-Based Analysis of Multidimensional Energy Landscapes: Application of Dynamic Force Spectroscopy and Steered Molecular Dynamics Simulations to an Antibody-Peptide Complex” .....	55
8.2 “Site-specific and covalent immobilization of biomolecules for single molecule experiments” .....	104
8.3 “Affinity-Matured Recombinant Antibody Fragments Analyzed by Single Molecule Force Spectroscopy” .....	132
8.4 “B-S Transition in Short Oligonucleotides” .....	141
8.5 “Force-Induced DNA Slippage” .....	152
8.6 “Site-Specific Immobilization of Genetically Engineered Variants of <i>Candida antarctica</i> Lipase B” .....	160
8.7 “Functional Expression of <i>Candida antarctica</i> Lipase B in <i>Escherichia coli</i> ” .....	164
<b>9 Curriculum vitae</b> .....	175
<b>10 Acknowledgements</b> .....	176

## 1 Summary

Within the scope of this work, the dissociation properties and unbinding pathways of various examples of receptor ligand interactions were analyzed using high-resolution single molecule force spectroscopy.

1. The molecular interactions between short complementary oligonucleotides, consisting of 20 and 30 base pairs, were analyzed with dynamic force spectroscopy. It was shown that the gained force-extension curves for a 30 base pair long duplex exhibit a region of constant force (plateau) at 65 pN. This force plateau corresponds to the transition from B-DNA into the highly overstretched S-DNA (B-S transition), which until now has only been found for long double stranded  $\lambda$ -DNA. Oligonucleotides, containing 20 base pairs, exhibited rupture forces below 65 pN and did not show any evidence of a B-S transition.

2. The dissociation properties of short oligonucleotides with repetitive DNA sequences were analyzed. Whereas in the above-mentioned example the externally applied force defines the dissociation pathway by inducing the B-S transition, here internal factors, i.e. the repetitive DNA sequence, open up an additional unbinding pathway as has been shown with simulations. The DNA can form bulge loops, which diffuse through the DNA backbone. As soon as one bulge loop reaches the end of the strand, it annihilates, resulting in a displacement of the strands relative to each other. Utilizing a newly developed measurement protocol the existence of this so-called slipping process was proven. The slipping process is characterized by a critical threshold force of 35-40 pN and depends on the applied retract velocity.

3. The third example consists of three closely related recombinant antibody fragments which were taken from different steps of an affinity maturation process. Differing only in a few amino acids, these antibody fragments again allow the analysis of the influence of internal modifications in the molecule on the binding potential. Using a 33 amino acid long peptide antigen, dynamic force spectroscopy experiments were performed showing that this molecular

interaction can be described with a simple mechanothermally activated transition in a two-level system. Whereas the potential width was found to be identical for all three antibody fragments, the dissociation rates of two of the analyzed antibody fragments differ significantly, leading to the conclusion that, in this example, the mutations cause differences in the height of the activation barrier.

4. The above-mentioned antibody-peptide system was slightly modified to be able to analyze the influence of external modifications on the unbinding pathway. Experiments were performed where the attachment points of the 12 amino acid long peptide were varied. These measurements yielded clearly distinguishable dissociation rates and potential widths, proving that the direction of the applied force determines the unbinding pathway. The results suggest that the change in the direction of the applied force allows a more detailed exploration of the energy landscape.

Whereas the analysis of the unbinding pathways and threshold forces of DNA-DNA and antibody-antigen interactions is very interesting in itself and can yield valuable information about the stability and function of biological interactions, it also opens up the possibility of using these biological interactions as tools to analyze and manipulate other nanoscale objects.

One potential application is also part of this thesis. A model system was designed which allows the force-based manipulation of the activity of the enzyme Lipase B from *Candida antarctica* (CalB). This model system uses the above-mentioned antibody-antigen interaction as a “molecular fuse” to prevent unfolding of the enzyme during analysis. The realization of this measurement set-up required several preliminary steps, which are all part of this thesis. These include the preparation and characterization of enzyme variants with the attached peptide sequence.

## 2 Introduction

In general, biomolecules can be regarded as soft materials which, due to thermal fluctuations, sample a large ensemble of slightly different conformations around their average structure. This picture can be easily described by using multidimensional energy landscapes that define the relative probabilities of the conformational states and the energy barriers between them (1). The corresponding rates, and therefore the equilibrium between these conformations, can be influenced by a variety of internal and external factors, such as phosphorylation, mutations, ligand binding, or even the action of external forces on the molecule. All these factors can alter the relative energy barrier height between different substates or even generate new local substates. In general, these different substates are characterized by slightly different properties of the biomolecule. These multidimensional energy landscapes determine folding and unfolding pathways as well as binding and unbinding processes (2,3). Furthermore, it has been shown that these multidimensional energy landscapes are the source of fluctuations in the activity of enzymes (4-8). Since the application of an external force is known to modify the energy landscape of biological systems (9-11), it is an established approach to apply forces to biological molecules and to analyze their response in order to obtain information about the energy landscape (12-14).

One of the most powerful techniques to apply forces and to manipulate biological systems is the atomic force microscope (AFM) (15-17). This is mainly the result of the very high spatial resolution which allows addressing of single molecules and the (theoretical) possibility of obtaining additional information about the corresponding energy landscape. In the case of (un)folding or (un)binding processes, the response of the biological system can be detected directly with the AFM as a change in force or length or simply by the rupture of the bond of interest. The analysis of unbinding processes of different biological systems has been the main objective of this thesis (chapter 5).

The detailed knowledge of the unbinding pathways of different biological interactions is very interesting in itself, but more importantly it allows the usage of a well-characterized interaction as a molecular tool. These molecular

---

interactions can serve as reversible connectors, which can be used to transmit forces between a transducer (such as the cantilever of an AFM) and another biomolecule of interest. By using appropriately designed and well-characterized connectors, the biomolecule of interest can be efficiently manipulated without damaging it, and its response to externally applied forces can be analyzed. This strategy has been used to manipulate the activity of an enzyme and is explained in more detail in chapter 6.1.

Furthermore, based on the knowledge of the unbinding characteristics of several biological interactions, a system of hierarchical forces can be built up. One biological interaction can pick up a biomolecule of interest and release it at a defined position. Due to the high spatial resolution of an atomic force microscope, the accuracy of the positioning is in the nanometer range. When repeating this cycle many times, this strategy, which is described in more detail in chapter 6.2, can be used for bottom up approaches in nanotechnology.

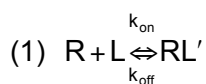
## 3 Force spectroscopy

Before presenting the results and their potential applications in detail, the models, which describe the stability of biological interactions in the absence and presence of an externally applied force, are summarized in chapter 3.1. Furthermore, various techniques for the application and detection of molecular forces are introduced (chapter 3.2). Finally, atomic force microscopy, the technique which has been used within the scope of this work, is explained in more detail.

### 3.1 Theory

#### 3.1.1 Theory of molecular interactions in the absence of an external force

Many biological interactions can be described with a very simplified model containing two states only (two-state model). These two states represent a receptor ligand system in its bound (RL') and unbound (R+L) state and are separated by a transition state characterized by an energy barrier. The transition between these two states occurs with the rate constants  $k_{on}$  and  $k_{off}$  (figure 1).



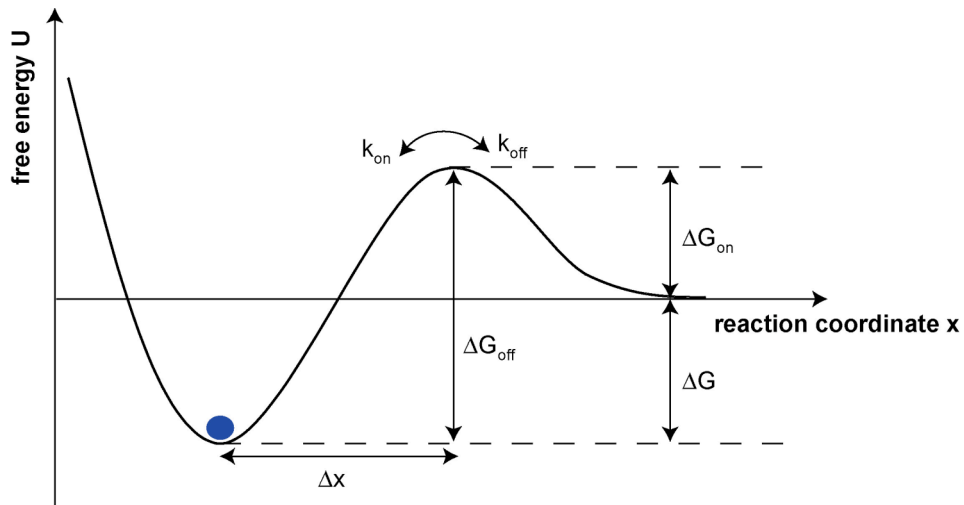


**Figure 1. 1-dimensional energy landscape of a bound receptor ligand complex (blue) without an externally applied force. The free energy  $\Delta G$  between the bound (blue) and the unbound state is composed of the difference between the energy barrier  $\Delta G_{\text{off}}$  and the activation energy  $\Delta G_{\text{on}}$ . Thermal fluctuations enable the ligand to overcome the energy barrier  $\Delta G_{\text{off}}$  (and  $\Delta G_{\text{on}}$ ).  $k_{\text{off}}$  and  $k_{\text{on}}$  represent the natural dissociation and association rate respectively.  $\Delta x$  reflects the potential width.**

The rate constants  $k_{\text{off}}$  and  $k_{\text{on}}$  thereby depend on the attempt frequency and the height of the respective energy barriers ( $\Delta G_{\text{off}}$  or  $\Delta G_{\text{on}}$ ) between the two states (bound and unbound) (Van't Hoff-Arrhenius law).

$$(2) \quad k_{\text{off}} = \nu_{\text{off}} \cdot e^{\frac{-\Delta G_{\text{off}}}{k_B \cdot T}}$$

$$k_{\text{on}} = \nu_{\text{on}} \cdot e^{\frac{-\Delta G_{\text{on}}}{k_B \cdot T}}$$

where  $\nu_{\text{off}}$  and  $\nu_{\text{on}}$  represent the attempt frequency according to Kramers,  $k_B$  is the Boltzmann constant and  $T$  is the absolute temperature.

The constant  $K_D$ , which represents a measure for the strength of a bond in equilibrium, is given by the ratio of the concentrations of the products ( $RL'$ ) and the educts ( $R+L$ ) in stationary equilibrium and therefore reflects the ratio of the natural dissociation and association rate.

$$(3) K_D = \frac{k_{\text{off}}}{k_{\text{on}}} = \frac{[R] \cdot [L]}{[RL']}$$

With (4)  $\Delta G_{\text{off}} = \Delta G_{\text{on}} + \Delta G$  and  $\frac{v_{\text{off}}}{v_{\text{on}}} \approx 1$ , the equilibrium constant equals:

$$(5) K_D = e^{\frac{-\Delta G}{k_B \cdot T}}$$

### 3.1.2 Theory of molecular interactions in the presence of an external force

A model for the force-induced dissociation of a molecular bond was first developed by Bell (18) and later by Evans et al. (9). This now well-established Bell-Evans model describes the tilt of the potential landscape, brought up by the external force (which is applied along the reaction coordinate  $x$ ), which results in a reduction of the energy barrier by  $-F \cdot x$  (figure 2). In addition, one assumes, that no reverse reaction occurs, due to the application of the external force.

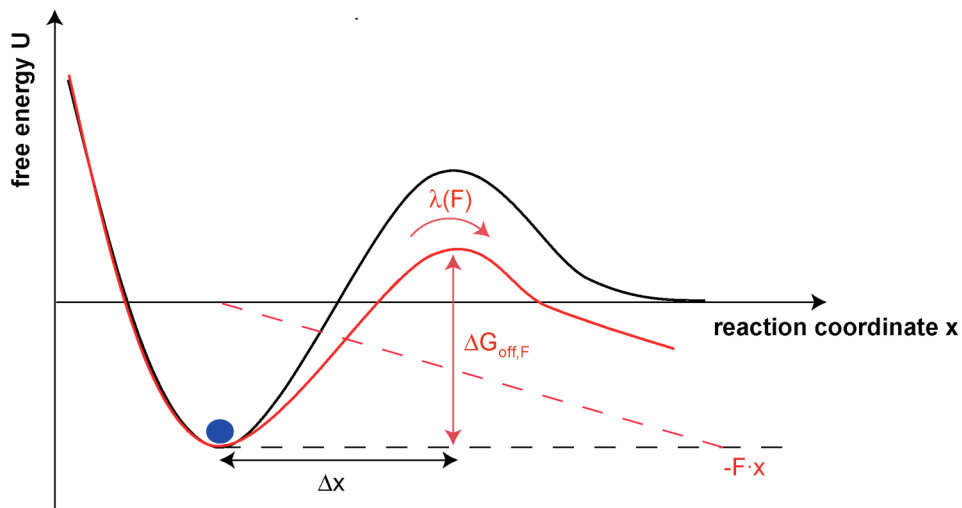


**Figure 2. Comparison of the 1-dimensional energy landscape of a bound receptor ligand complex without an externally applied force (black curve) and when an externally applied force is acting on the complex (red curve). The applied force  $F$  leads to a reduction of the energy barrier by  $-F \cdot x$  (dashed red line).**

The reduction of the energy barrier leads to a decrease of the life time of a receptor ligand complex and therefore to an increase in the dissociation rate  $\lambda(F)$ :

$$(6) \quad \lambda(F) = \nu_{\text{off}} \cdot e^{-\frac{\Delta G_{\text{off}} - F \cdot \Delta x}{k_B \cdot T}}$$

Starting point for the determination of the force dependent dissociation rate  $\lambda(F)$  is the Van't Hoff-Arrhenius law, described in equation (2):

$$(7) \quad k_{\text{off}} \equiv \lambda(F=0) = v_{\text{off}} \cdot e^{-\frac{\Delta G_{\text{off}}}{k_B \cdot T}}$$

Taking into account that the applied force is a function of time, the time dependent change in the number of bound receptor ligand systems  $N_B(t)$  can be displayed with first order kinetics:

$$(8) \quad \frac{dN_B(t)}{dt} = -\lambda(t) \cdot N_B$$

By integrating equation (8), the number of bound receptor ligand systems at the time  $t$  can be calculated:

$$(9) \quad N_B(t) = e^{-\int_0^t dt' \lambda(t')}$$

The number of bound receptor ligand systems is normalized with respect to the total number of binding partners. Therefore the number of dissociated receptor ligand systems can be calculated with the following equation:

$$(10) \quad N_D(t) = 1 - N_B(t) = 1 - e^{-\int_0^t dt' \lambda(t')}$$

Using the assumption, that the force is a continuously reversible function of the time, the time can be replaced by the force:

$$(11) \quad N_D(F) = 1 - e^{-\int_0^F df \lambda(f) \cdot \frac{1}{\dot{f}}}$$

with  $\dot{f} = \frac{df}{dt}$  = time dependent change of the force = the loading rate

---

Therefore, the probability that a receptor ligand complex dissociates under a certain externally applied force  $F$  equals:

$$(12) \quad p(F) = \frac{dN_D}{dF}(F) = \lambda(F) \cdot \frac{1}{F} \cdot e^{-\int_0^F \frac{\lambda(f)}{f} df}$$

Kramers formed the equation of motion for a receptor ligand bond in a potential and solved it for large and small damping. For large damping, the motion of the ligand can be described by means of the Langevin equation:

$$(13) \quad M \cdot \ddot{x} = -\frac{dU(x)}{dx} - \gamma \cdot \dot{x} + \xi(t)$$

with  $M$  the mass of the ligand,  $x$  the distance between receptor and ligand,  $U(x)$  the potential,  $\gamma$  the friction constant and  $\xi(t)$  a fluctuating force, which corresponds to the thermal noise. If an external force  $F$  is applied to the system, the following equation is obtained in equilibrium:

$$(14) \quad -\frac{dU(x)}{dx} = F$$

In order to break up the receptor ligand bond, the ligand has to cover the distance  $\Delta x$ . Using equation (13), the time  $\tau$ , which the ligand needs to overcome the distance  $\Delta x$ , can be calculated:

$$(15) \quad \tau = \frac{2 \cdot \pi \cdot \gamma}{\omega_{\min} \cdot \omega_{\max}} \cdot e^{\frac{\Delta G_{\text{off}} - F \cdot \Delta x}{k_B \cdot T}}$$

Equation (15) holds for small forces  $F$ .  $\omega_{\min}$  and  $\omega_{\max}$  equal the root of the curvature of the new potential  $\Delta G_{\text{off}} - F \cdot \Delta x$  at the minimum and maximum. In the following, it is assumed, that  $\omega_{\min}$  and  $\omega_{\max}$  do not depend on the force.

---

With  $\lambda(F) = \frac{1}{\tau}$ , the Kramers relation is obtained:

$$(16) \quad \lambda(F) = \frac{\omega_{\min} \cdot \omega_{\max}}{2 \cdot \pi \cdot \gamma} \cdot e^{-\frac{\Delta G_{\text{off}} - F \cdot \Delta x}{k_B \cdot T}}$$

If the applied force  $F$  equals 0, the Kramers relation is reduced to:

$$(17) \quad k_{\text{off}} = \frac{\omega_{\min} \cdot \omega_{\max}}{2 \cdot \pi \cdot \gamma} \cdot e^{-\frac{\Delta G_{\text{off}}}{k_B \cdot T}} \quad (\text{see equation 2})$$

As stated in chapter 3.1.1 this relation defines the natural dissociation rate  $k_{\text{off}}$ . The force dependent dissociation rate  $\lambda(F)$  can therefore be written in terms of the natural dissociation rate  $k_{\text{off}}$  as follows:

$$(18) \quad \lambda(F) = k_{\text{off}} \cdot e^{\frac{F \cdot \Delta x}{k_B \cdot T}}$$

With equation (18), the probability  $p(F)$  that a receptor ligand complex dissociates in a certain force interval  $[F, F+dF]$  can be calculated:

$$(19) \quad p(F) = k_{\text{off}} \cdot e^{\frac{F \cdot \Delta x}{k_B \cdot T}} \cdot \frac{1}{\dot{F}} \cdot e^{-k_{\text{off}} \int_0^F e^{\frac{f \cdot \Delta x}{k_B \cdot T}} \cdot \frac{1}{\dot{f}} df}$$

By differentiating equation (19),

$$(20) \quad \frac{d}{dF} p(F) = 0$$

the most probable rupture force  $F^*$  can be determined:

---

$$(21) F^* \left( \dot{F} \right) = \frac{k_B \cdot T}{\Delta x} \cdot \ln \left( \frac{\dot{F}}{k_{\text{off}}} \cdot \frac{\Delta x}{k_B \cdot T} \right)$$

From equation (21) it is obvious, that the most probable force  $F^*$  depends linearly on the logarithm of the loading rate  $\dot{F}$ . This can be imagined as follows. At slow loading rates, the receptor ligand complex has more time to overcome the energy barrier by thermal fluctuations than at high loading rates. Therefore, at slow loading rates, the transition will occur at smaller rupture forces. In addition equation (21) relates the most probable rupture force  $F^*$  with the natural dissociation rate  $k_{\text{off}}$ . The potential width  $\Delta x$  of the respective receptor ligand complex can also be obtained. Both values,  $k_{\text{off}}$  and  $\Delta x$ , can be determined from a plot of the most probable rupture force versus the logarithm of the corresponding loading rate (see equation (21)). For a two level system this plot shows a straight line. The potential width  $\Delta x$  can therefore be gained from the slope and the dissociation rate from the intersection of this straight line with the x-axis at zero force.

## 3.2 Techniques for the application and detection of molecular forces

Having introduced the theoretical background which describes the stability of receptor ligand interactions in the absence and presence of an externally applied force, the following chapter summarizes the most common techniques used for the application and measurement of forces (chapter 3.2.1) including a detailed description of the atomic force microscope (chapter 3.2.2).

### 3.2.1 Overview

In the last few years several new techniques for the investigation of molecular forces have been developed. These techniques cover a huge dynamic range and possess different sensitivities. Therefore they are suitable for the exploration of various different biological systems. Table 1 shows a short overview and contains the most common force spectroscopy techniques, their force, spatial and time resolution.

technique	force resolution	spatial resolution	time resolution
optical tweezers (OT)	0.1 pN – 150 pN	> 1 nm	10 ms
magnetic tweezers	10 fN – 100 pN	> 10 nm	1 s
biomembrane force probe (BFP)	1 pN – 1000 pN	> 5 nm	1 ms
atomic force microscope (AFM)	> 5 pN	> 0.1 nm	10 ms

**Table 1. Summary of the techniques used in single molecule force spectroscopy.**

#### Optical tweezers

The basic principle of optical tweezers relies on the momentum transfer of photons associated with bending light (19). If a laser beam encounters a particle, the light will be deflected and therefore changes its direction. This leads to a change of the momentum of the laser beam. Conservation of momentum requires that the particle has to undergo an equal and opposite momentum change. The sum of the changes in momentum for particles with a

---

diameter at most half as large as the wavelength of the laser light causes a net force which can be split into two components: the scattering force  $F_{\text{scattering}}$  and the gradient force  $F_{\text{gradient}}$  (figure 3). The scattering force points to the direction of the incident laser light (z-direction). The gradient force, originating from the Gaussian intensity profile of the laser, points towards the center of the laser beam (in the x-y plane).  $F_{\text{gradient}}$  is a restoring force and therefore pushes the particle, which has a higher refractive index than its surrounding medium, towards the largest intensity of light. If the contribution to the scattering force of the refracted rays is larger than the contribution of the reflected rays, a restoring force is also created along the z-axis and a stable trap will exist. The restoring force of an optical trap works like an optical spring and therefore is proportional to the displacement of the particle out of the trap. Optical tweezers are often used in biological sciences, for example to analyze molecular motors (20-23) or to mechanically unzip double stranded DNA (24). The latter experiment was carried out by binding one end of the DNA duplex of interest via a biotin streptavidin complex to the particle. The other end of the duplex was bound to a surface thereby using the anti-digoxigenin system for coupling. By lateral displacement of the surface, the force, which is necessary to unzip the duplex, is applied to the particle and therefore can be measured.

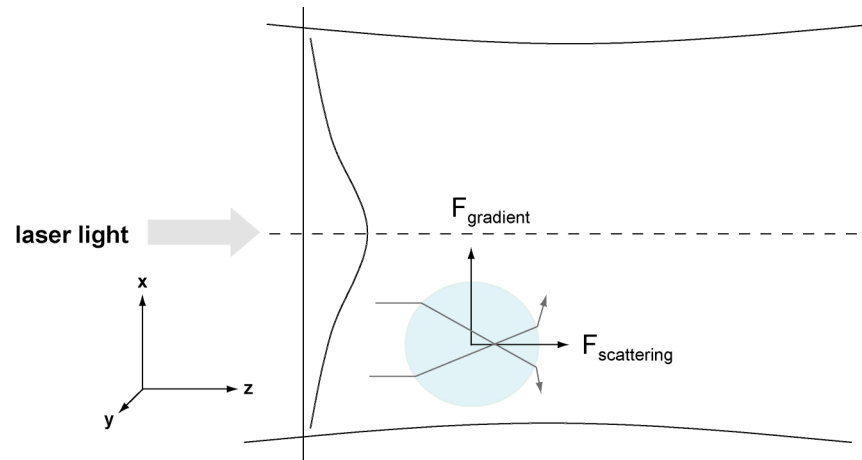


**Figure 3. Basic principle of optical tweezers (OT). A particle in a laser beam experiences two force components: the scattering force, which acts along the propagation direction of the laser light and originates from radiation pressure and the gradient force, which drives the particle towards the laser beam center and can be explained with the light gradient.**

#### Magnetic tweezers

Another force spectroscopic measurement instrument are magnetic tweezers. They utilize a magnetic field gradient to manipulate micrometer-sized paramagnetic fluorescent beads (25) (figure 4). As shown in figure 4 a molecule of interest is attached to the paramagnetic fluorescent bead and a surface. The inhomogeneous magnetic field exerts a force on the bead and the molecule of interest is stretched. By rotating the magnetic field, torque can be applied to twist the molecule. Therefore the response of molecules to torsion forces can be analyzed. Strick et al. (26) used this technique to analyze DNA uncoiling by a type II topoisomerase.

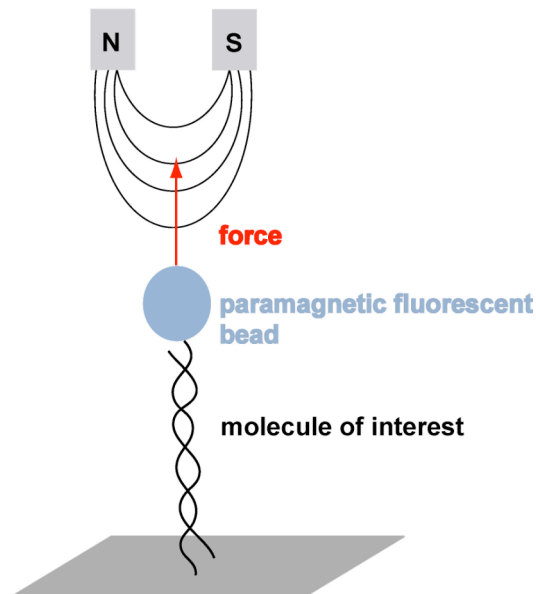


**Figure 4. Basic principle of magnetic tweezers. A fluorescent paramagnetic bead in an inhomogeneous magnetic field experiences a force. By attaching the biomolecule of interest to the paramagnetic bead and the surface, it can be stretched.**

#### Biomembrane force probe

The biomembrane force probe was pioneered by Evans et al. (10). A red blood cell, which is very elastic compared to other cells, is sucked into a micropipette. The generated depression determines the membrane rigidity and therefore the spring constant. On the opposite side of the red blood cell, a micrometer-sized bead is attached. If a force is applied to this micrometer-sized bead, the membrane of the red blood cell is deformed. This deformation can be converted into a force. Merkel et al. used this technique for the loading rate dependent measurement of streptavidin (or avidin) and biotin, and for the first time probed bond formation over six orders of magnitude. These measurements revealed that the bond strength depends on how fast they are loaded.

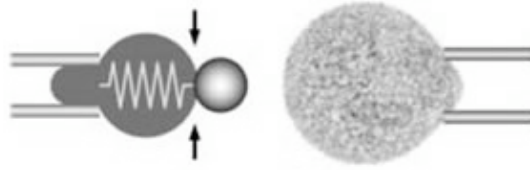


**Figure 5. Principle of a biomembrane force probe (BFP). A red blood cell, functionalized with a small bead is sucked into a micropipette. The membrane of the red blood cell is deformed if a complementary surface contacts the micrometer-sized bead. This deformation is used to determine the applied force (picture from <http://www.bme.ucdavis.edu/profile/vheinrich/index.html>).**

### 3.2.2 The atomic force microscope (AFM)

The atomic force microscope, originally invented by Binnig, Quate and Gerber (27) for the characterization of surfaces, has become an important tool for the detection of unbinding- and stretching-forces of individual biomolecules (15,28-30). A schematic setup of an AFM is shown in figure 6.

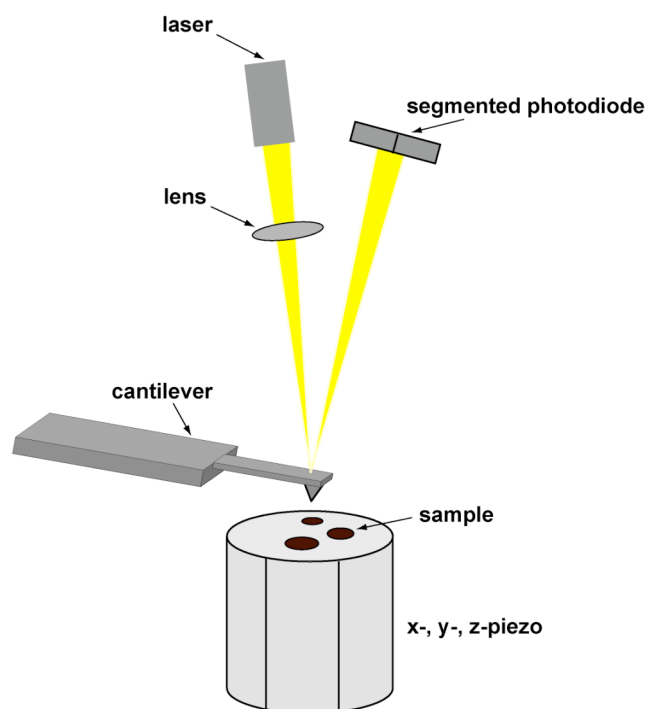


**Figure 6. Schematic setup of an atomic force microscope (AFM).** The key-part of an atomic force microscope is a microscopic small cantilever, which acts as a sensitive force sensor. If the cantilever bends, due to the establishment of an interaction between the nanoscopic small tip of the cantilever and the mounted sample on the surface, the laser is deflected. This deflection can be detected with a two-segmented photodiode. A z-piezo regulates the distance between the cantilever tip and the surface.

For the analysis of biomolecular interactions one binding partner is coupled to the cantilever and the second binding partner is immobilized on the surface. If the cantilever tip and the surface are brought into contact, an interaction between the molecules attached to the tip and the surface immobilized molecules is established. In the next step, the sample is retracted, thereby

applying a force to the established interaction. The cantilever bends until the applied force is higher than the force of the established interaction. This bending is analyzed with the laser which is focused onto the cantilever and thereby reflected. The change in the reflected laser beam (caused by the bending of the cantilever) is detected with a two-segmented photodiode. Based on the obtained difference in voltage, the distance between the cantilever tip and the surface is calculated. Using this information, the force which is applied to the interaction between the cantilever tip and the surface is calculated from the determined deflection and the spring constant of the used cantilever. Thus, the applied force is known throughout the whole process.

Using the knowledge of the force and the distance (obtained from the movement of the z-piezo) between the cantilever tip and the surface, so-called force-extension curves are recorded. From these curves the rupture force (the force at which the established interaction ruptures) and the rupture length (length at which the rupture of the established interaction occurs) can be determined. The corresponding loading rate can be calculated from the slope of the force versus time curve at the moment of the rupture event.

As stated earlier, the dissociation of a molecular interaction is influenced by thermal fluctuations. This leads to the conclusion, that one single rupture event is a stochastic process. To obtain sufficient statistics many force-extension curves containing single rupture events have to be recorded. The obtained values for the rupture forces and corresponding loading rates are then plotted in histograms and fitted with a Gaussian distribution. The maxima of these distributions represent the most probable rupture force and the corresponding loading rate. As described in chapter 3.1.2, the natural dissociation rate  $k_{\text{off}}$  and the potential width  $\Delta x$  can be determined from a plot of the most probable rupture force versus the logarithm of the corresponding loading rate.

## 4 Site-specific and covalent immobilization of biomolecules to surfaces

As has already been stated in chapter 3.2.2, AFM-based single molecule force spectroscopy measurements require the attachment of the biomolecules of interest to the surface and the cantilever. Considering the picture of multidimensional energy landscapes, site-specific in contrast to random attachment protocols are highly desired because the attachment at different positions might favor different unbinding pathways. Furthermore, coupling at different positions might result in slightly different conformations of the biomolecules of interest. In addition a covalent immobilization of the biomolecules is of advantage, leading to a high interaction frequency and therefore allows the measurement of a high number of interactions in a reasonable time, which is required to obtain good statistics. The immobilization procedure should therefore generate stable surfaces with low non-specific binding, but a high number of reactive sites to allow a high dynamic range in order to adjust the density of the biomolecules on the surface as desired.

Within the scope of this work an immobilization protocol (see publication P2) was developed which meets these demands. The immobilization procedure generated during this thesis relies on poly(ethylene glycol) (PEG) as the spacer between the biomolecules and the surfaces and cantilevers respectively (31). Due to its properties, PEG provides protein-resistant surfaces and therefore reduces the probability of non-specific binding events (32-34). In more detail, the protocol utilizes hetero-bifunctional poly(ethylene glycol) (PEG) spacers, which carry a N-hydroxy succinimide (NHS) group on one end and a maleimide group on the other end. After coupling the PEG via its NHS group to an amino-functionalized surface, the relatively stable but highly reactive maleimide group allows the coupling of biomolecules, which carry a free thiol group. Thiol groups can be incorporated into oligonucleotides and peptides during solid phase synthesis. For proteins the usage of thiols relies on the presence of a free cysteine in the molecule, which can either be present naturally or can be introduced by site-directed mutagenesis at a desired position. This protocol has been shown to work for a broad range of amino-functionalized surfaces (glass

---

(35-38), Si<sub>3</sub>N<sub>4</sub> cantilevers (36-38) and even PDMS) and many different types of biomolecules (oligonucleotides (36,37,39), peptides (38), recombinant antibody fragments (38) and enzymes (35)). This protocol has been used for all the force spectroscopic measurements of receptor ligand interactions described in chapter 5.

## **5 Analysis of different types of biological interactions with the AFM**

Using the atomic force microscope as described in chapter 3.2.2 and the immobilization protocol summarized in chapter 4, the unbinding pathways of various types of biological interactions were analyzed. The physical and biochemical properties of the used biomolecules - DNA and antibodies - are described in detail in chapter 5.1.1 and 5.2.1. The results of the force spectroscopic measurements are summarized in chapter 5.1.2 and 5.2.2.

### **5.1 DNA-DNA interactions**

#### **5.1.1 Background and state of the art**

The primary structure of DNA consists of nucleotides which are coupled together, building a linear polymer. A nucleotide contains one of the four universal bases adenine (A), thymine (T), guanine (G) and cytosine (C), the monosaccharide desoxyribose and a mono-, di- or triphosphate. The phosphate is attached to the 5' carbon atom and one of the four bases is linked to the 1' carbon atom of the desoxyribose respectively. In the polymer one nucleotide is linked via the OH-group at the 3' end of the desoxyribose and to the (mono)phosphate at the 5' carbon atom of the next nucleotide (figure 7). Therefore single stranded DNA possesses directionality (from 5' end to 3' end).

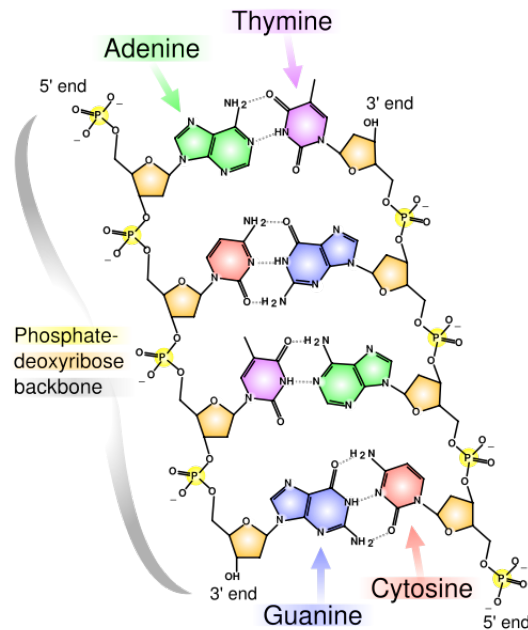


**Figure 7. Primary structure of a DNA double strand. The bases adenine (A), thymine (T), cytosine (C) and guanine (G) are linked to the phosphate-deoxyribose backbone. Two hydrogen bonds are formed between A and T, three hydrogen bonds between C and G (picture from <http://en.wikipedia.org/wiki/Dna>).**

Naturally occurring DNA almost always forms a double stranded helix. The secondary structure of this DNA double helix was determined by Watson and Crick in 1953. It consists of two reverse complementary base sequences, where the two DNA strands with opposite directionality wind around each other and form hydrogen bonds between the complementary bases. The complementary bases adenine and thymine form two and the complementary bases cytosine and guanine form three hydrogen bonds (figures 7 and 8). Mediated by hydrophobic interactions between neighboring bases, their heteroaromatic rings align and expel water from the space between two base pairs. This so-called base stacking and the formation of hydrogen bonds between two bases (Watson-Crick base pair) stabilize the helical structure of the DNA.

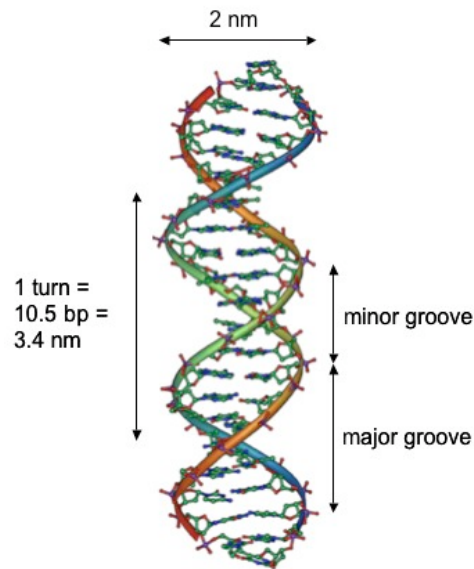


**Figure 8. Helical structure of the B-DNA.** Under physiological conditions, the double stranded DNA adopts the right-handed B-form, which exhibits a diameter of 2 nm, a 2.2 nm wide major groove and a 1.2 nm wide minor groove (picture from <http://en.wikipedia.org/wiki/Dna>).

The elastic and mechanical behavior of double stranded DNA has been investigated with a variety of techniques using long DNA molecules from phage  $\lambda$  ( $\lambda$ -DNA). For these long DNA molecules an equal distribution of the different bases is assumed. Stretching experiments, covering a broad range of forces, were carried out with magnetic tweezers (25), optical traps (40,41) and the atomic force microscope (42). At 65-70 pN, the DNA molecule exhibits a highly cooperative transition, which refers to the conversion of B-DNA into an overstretched conformation called S-DNA (B-S transition) (figure 9). Hereby the DNA molecule stretches up to a factor of 1.7 of its B-form contour length. If the force is increased further, a second transition – the so-called melting transition – occurs. During this transition, the double stranded DNA is split into two single strands. Upon further extension, the force increases drastically until the remaining single stranded DNA finally ruptures (42). Besides force spectroscopy experiments, molecular dynamics simulations and various theoretical approaches give detailed insights into the process of this so-called B-S Transition (43-50).

---

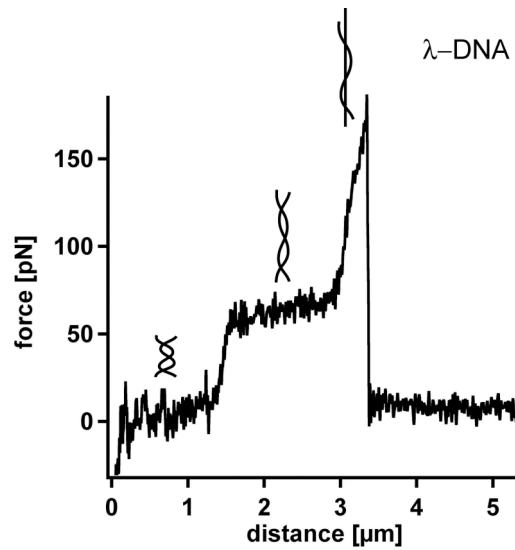


**Figure 9.** Force-extension curve of long double stranded  $\lambda$ -DNA, recorded with an AFM (picture from Morfill et al. (37)).  $\lambda$ -DNA was adsorbed non-specifically to a gold surface and picked up with a cantilever tip. Upon retraction, the double stranded  $\lambda$ -DNA, which is attached between the cantilever tip and the gold surface, is stretched until the DNA finally ruptures. At a force of 65-70 pN the well-known highly cooperative B-S transition is observed. In this specific force extension curve no breakage of the single strand can be observed. Most likely the DNA detaches from the surface before the remaining single strand melts off.

Whereas Smith, Wang and Rief et al. carried out experiments with long double stranded DNA, Strunz (51) and Pope et al. (52) used short oligonucleotides for their experiments. Short oligonucleotides have several advantages compared with long  $\lambda$ -DNA. First, during solid phase synthesis, specific reactive groups can be attached to the ends of the oligonucleotides, which can be used for specific coupling to surfaces (e.g. cantilever tips) or other biomolecules. Second, when using oligonucleotides the sequence and the length of the DNA can be designed as desired. In addition to the described unbinding mechanism via the B-S transition additional mechanisms have been discovered (figure 10), some of them only for short DNA oligonucleotides.

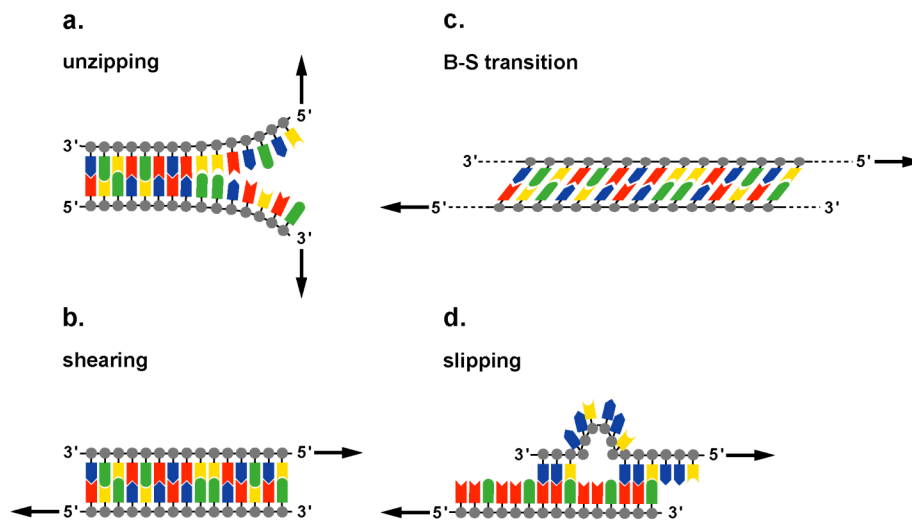


**Figure 10. Different unbinding mechanisms of DNA if an external force is applied to the duplex (picture from the dissertation from Kerstin Blank). The unbinding mechanism is dependent on the length and the sequence of the considered DNA duplex, as well as the direction and the rate of the externally applied force.**

In figure 10a an external force is applied to the 5' end of one strand of a DNA duplex and to the 3' end of the other. This leads to a sequential hydrogen bond breakage between the complementary base pairs, which therefore open up just like a zipper (“unzipping-geometry”). The forces required to unzip a DNA duplex depend on the sequence composition and are independent of the applied loading rate. In single molecule force spectroscopy experiments Rief et al. (42) and Krautbauer et al. (53) revealed unbinding forces of  $(20 \pm 3)$  pN for a G-C base pair and  $(9 \pm 3)$  pN for an A-T base pair.

In figure 10b the external force is applied to both strands at the 5' end. In this geometry all hydrogen bonds between the base pairs have to open up at the same time. The DNA duplex is sheared apart (“shear-geometry”). This process is presumed to occur only for short oligonucleotides with unbinding forces below 65 pN. Above this value the previously described B-S transition is expected (figure 10c). Strunz et al. (51) performed experiments, which show that the measured unbinding forces to shear short oligonucleotides apart (30, 20 and 10 base pairs) are a function of the applied loading rate and the number of base pairs. However, due to experimental noise, no B-S transition was

observed in these experiments. Within the scope of this thesis, single molecule force spectroscopy measurements have been performed which prove the existence of the B-S transition in short oligonucleotides of 30 base pairs. The results are summarized in chapter 5.1.2.1 (publication P4).

In figure 10d an external force is applied to the 5' ends of repetitive DNA. This leads to the formation of bulge loops which propagate along the DNA strand. As soon as one bulge loop reaches the end of the strand, it annihilates, resulting in a displacement of the strands relative to each other. This so-called slipping mechanism was predicted theoretically by Neher et al. (54) and should result in a defined length increase of the DNA duplex. It can theoretically occur with and without an externally applied force. Within the scope of this thesis, single molecule force spectroscopy measurements have been performed which prove the existence of this slipping mechanism for three different oligonucleotide sequences. Chapter 5.1.2.2 contains a short summary of the performed experiments (publication P5).

## **5.1.2 Summary of the performed measurements**

### **5.1.2.1 Detection of the B-S transition**

As indicated in chapter 5.1.1, high-resolution AFM-based single molecule force spectroscopy was employed to explore the unbinding mechanism of short complementary DNA duplexes consisting of 20 and 30 base pairs in the shear geometry (see publication P4).

For the 30 base pair long duplex, 30 % of the obtained force-extension curves showed a deviation from the two-state FJC-fit (freely jointed chain) and exhibited a region of constant force (plateau) at 65 pN, which corresponds to the transition from B-DNA into a highly overstretched S-DNA (see chapter 5.1.1). During this so-called B-S transition, the DNA duplex lengthens by a factor of 1.7, which results in a theoretical length value of 6.3 nm for a 30 base pair long DNA duplex. The observed force plateaus resulting from this length increase showed values between 3 nm and 7 nm. This plateau length distribution indicates that the dissociation of a 30 base pair duplex mainly occurs during the B-S transition. Loading rate dependent measurements were additionally performed to explore the unbinding pathway further. These measurements resulted in a dissociation rate of  $9.6 \cdot 10^{-28} \text{ s}^{-1}$  and a potential width of 4.6 nm for the 30 base pair long DNA duplex.

In contrast, the measured force-extension curves for a 20 base pair long DNA duplex exhibited rupture forces below 65 pN and did not show any evidence of a B-S transition. Loading rate dependent measurements revealed a dissociation rate of  $8.1 \cdot 10^{-14} \text{ s}^{-1}$  and a potential width of 2.9 nm.

### **5.1.2.2 Measurement of repetitive sequences**

To prove the existence of the slipping process for repetitive DNA sequences (see figure 10d in chapter 5.1.1) predicted theoretically by Neher et al. (54,55), high-resolution single molecule force spectroscopy measurements were performed to analyze the response of short repetitive DNA duplexes with dinucleotide and trinucleotide repeat units to an externally applied force. As described in chapter 5.1.1, repetitive sequences display richer dynamics compared with heterogeneous DNA sequences, which theoretically results in

---

additional unbinding pathways, caused by the formation, diffusion and annihilation of bulge loops at the ends of the DNA strands. The measurements, performed within the scope of this work, show that repetitive DNA duplexes indeed exhibit a different unbinding behavior and elongate under an applied shear force. Furthermore, they dissociate at significantly lower forces than heterogeneous sequences (see publication P5). Due to the introduction of a new measurement protocol, which sets the DNA duplex under constant force and then measures the relaxation of the molecule, the progressive lengthening of the repetitive DNA duplex could be verified experimentally.

The slipping threshold force, which is defined as the applied force value beyond which the DNA duplex starts to slip, equals 35-40 pN and depends on the retract velocity. Further experiments were carried out to examine the dependence of the slipping process on the length of the repeat unit. It could be shown that the slipping threshold force has a weaker dependence on the retract velocity for dinucleotide than for trinucleotide repeat units. Therefore the slipping mobility is slower for a sequence containing trinucleotides.

To obtain a more detailed behavior of the slipping process near the slipping threshold force, a constant force was applied to the repetitive DNA duplex, so that the duplex elongates and hereupon the force drops to the slipping threshold force. At this force the DNA duplex fluctuates in equilibrium, resulting in multiple back and forth slipping events. At a threshold force of 39 pN, a 30 base pair long repetitive DNA duplex with trinucleotide repeat units exhibits mean lifetimes of 0.031 s for the fully hybridized state and 0.022 s for the lengthened state.

These experiments prove in an impressive way that an externally applied force tilts the energy landscape of a biological interaction allowing the establishment of conditions where the two states in a two state system have almost equal probabilities.

## **5.2 Antibody-antigen interactions**

### **5.2.1 Background and state of the art**

Considered from a structural point of view, antibodies belong to the group of immunoglobulins, whose composition is summarized in the following by means of the IgG antibody molecule (figure 11). The IgG molecule consists of four polypeptide chains - two identical heavy chains and two identical light chains, which are connected via disulfide bonds. These disulfide bonds contribute to the stability of the IgG molecule. The structure of the IgG molecule represents the most common format of monoclonal antibodies – the Y format. The base of this Y-format, called Fc fragment, consists of the C-terminal part of the two heavy chains, which also are connected via disulfide bonds. This part of the molecule determines the immunoglobulin class of the antibody – in this case class G. The two arms of the Y-format are identical and each arm consists of the N-terminal half of one heavy chain and one light chain. This part of the molecule is called Fab fragment. It can either be generated by enzymatic cleavage of IgG molecules or with recombinant methods. Each Fab fragment is composed of two constant domains (one from the light chain and one from the heavy chain) and two variable domains (one from the light chain and one from the heavy chain). These two variable domains make up the so-called Fv fragment, which is able to bind the antigen. Each domain of the Fv fragment contains three complementarity determining regions (CDRs), which form the antigen binding site and are therefore responsible for the specificity of the antibody. Fv fragments are the smallest part of the antibody molecule, which is still capable of binding the antigen.

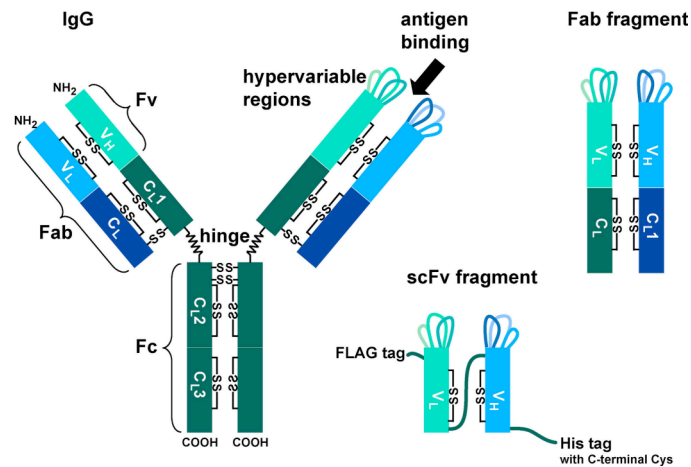


**Figure 11. Overview of different types of antibody molecules. The IgG molecule on the left side consists of one Fc fragment and two identical Fab fragments. The Fc part represents the base of the Y-format and is involved in the immune response for a given antigen. Each Fab fragment is composed of 4 different domains: one constant and one variable domain from each heavy and light chain of the antibody. The variable domains of the heavy and light chain form the Fv fragment. Fab fragments and Fv fragments (right side) can be produced with recombinant methods. In the case of Fv fragments the two domains are often connected with a peptide linker on the genetic level to increase the stability of the molecule resulting in a so-called single chain Fv fragment (scFv).**

Antibodies are available from many different sources. Monoclonal antibodies, for example in the IgG format, are produced by one type of hybridoma cell and recognize one specific and unique antigen. Recombinant antibodies, such as Fab and single chain Fv (scFv) fragments (figure 11), are selected from large libraries using e.g. phage display (56) or ribosome display (57). The usage of recombinant antibodies has several advantages. First, they provide more flexibility since they can be selected *in vitro*. Second, they can be manufactured in *E. coli* and therefore can be modified on the genetic level (58). Within the scope of this work, only single chain Fv fragments with known equilibrium constants (59,60) were used. To facilitate their purification a N-terminal FLAG- and a C-terminal His-tag was fused to the scFv fragments on the genetic level. In addition two glycines and a cysteine have been attached to

the C-terminus after the His-tag allowing site-specific immobilization of the scFv fragments (see chapter 4).

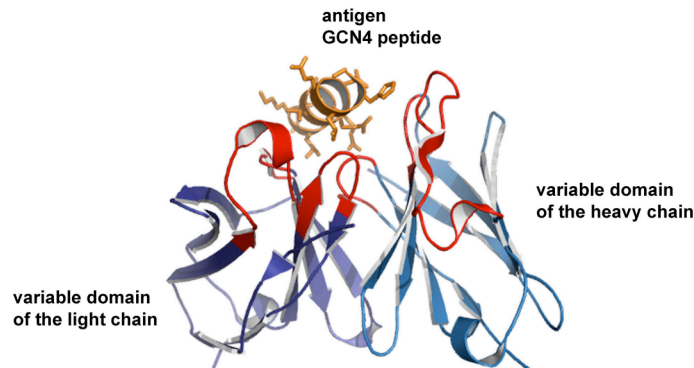


**Figure 12. Crystal structure of one of the used scFv fragments in complex with its peptide antigen (PDB no. 1P4B). The variable domains of the light and the heavy chain are shown in dark and light blue. The loops of the complementarity determining regions (CDRs) are illustrated in red. The bound 12 amino acid long peptide (yellow) adopts an  $\alpha$ -helical structure in complex with the antibody fragment (picture from the dissertation from Kerstin Blank).**

Figure 12 shows the crystal structure of one of the scFv fragments used in the AFM measurements. In total, 4 variants of one type of scFv fragment, which all bind the same peptide antigen, have been used for the experiments. These variants only differ in a few amino acids and have originally been generated against a 33 amino acid long peptide derived from the yeast transcription factor GCN4 (59-61). However, the crystal structure shows that the antibody only binds to a part of the peptide. Two different series of experiments have been performed using this system. For the first series the 33 amino acid long version of the peptide has been used to investigate the influence of mutations on the binding properties of the different scFv variants (chapter 5.2.2.1 and publication P3). For the second series the shortened 12 amino acid long peptide was used to demonstrate the dependence of the unbinding pathway on the direction of the applied force (chapter 5.2.2.2 and publication P1).

## **5.2.2 Summary of the performed measurements**

### **5.2.2.1 Analysis of the influence of mutations on the binding potential**

Within the scope of this work, single molecule force spectroscopy measurements were performed to analyze the unbinding pathway of three variants of the described antibody scFv fragment and the 33 amino acid long peptide (see chapter 5.2.1). The variants were taken from different steps of an affinity maturation process (see publication P3). Since they only differ from each other by a few mutations, the antibody-peptide system is a good model system for the investigation of the influence of mutations on the binding potential. The simplest level of analysis, which is based on a mechanothermally activated transition in a two-level system, provides a satisfactory description of the measured unbinding process. The most remarkable finding is that the different variants have a more or less identical potential width of 0.90 nm. Although the potential width is only a rough measure of how far the binding complex can be stretched and deformed until it finally ruptures, this finding leads to the conclusion that neither the geometry of the binding site nor the unbinding pathways of the three variants were significantly affected by the mutations during the affinity-maturation process. However, two of the examined variants exhibit clearly distinguishable dissociation rates of  $3.9 \cdot 10^{-3} \text{ s}^{-1}$  and  $4.9 \cdot 10^{-4} \text{ s}^{-1}$ . This difference in the dissociation rate is the consequence of one single point mutation, which obviously changes the depth of the binding potential.

### **5.2.2.2 Analysis of the influence of the direction of the applied force on the binding potential**

In publication P1 the unbinding pathway of one variant of the recombinant scFv fragments and the 12 amino acid long peptide was analyzed with AFM-based single molecule force spectroscopy and Steered Molecular Dynamics (SMD) simulations. The shortened version of the peptide was used for two reasons. First, the crystal structure in figure 12 is the starting point for the SMD simulations and therefore the AFM experiments were carried out with the same molecules. Second, it was intended to vary the attachment point of the peptide.

---

It was considered that the 12 amino acid long peptide is more suitable for these experiments since it represents the part which is effectively bound by the antibody.

The attachment of the peptide at different positions allows the analysis of the influence of the direction of the applied force on the unbinding pathway. Whereas the scFv fragment was again attached to the surface via its C-terminus, the peptide was attached to the tip of the cantilever, either via its N-terminus (setup N), its C-terminus (setup C) or via position 8 (in the middle) of the peptide sequence (setup M). Therefore three different setups were measured for a broad range of loading rates to gain information about the unbinding process. For setup N a dissociation rate of  $16.9 \cdot 10^{-3} \text{ s}^{-1}$  and a potential width of 0.82 nm was obtained. Setup C yielded a 13 fold slower dissociation rate of  $1.3 \cdot 10^{-3} \text{ s}^{-1}$  and a potential width of 1.10 nm. Finally setup M provided values of  $7.6 \cdot 10^{-3} \text{ s}^{-1}$  for the dissociation rate and 0.95 nm for the potential width. A detailed error analysis proved that the dissociation rates and the potential widths could be clearly separated leading to the conclusion that the direction of the applied force determines the unbinding pathway.

Complementary atomistic SMD simulations were performed, which also show that the unbinding pathways of the antibody-peptide system are dependent on the pulling direction. However, the main barrier to be crossed was independent of the pulling direction and is represented by a backbone hydrogen bond between GLY<sup>H</sup>-H40 of the antibody fragment and GLU<sup>O $\epsilon$</sup> -6<sub>peptide</sub> of the peptide. Furthermore, although the SMD simulations were performed at loading rates exceeding the experimental ones by orders of magnitude due to computational limitations, a detailed comparison of the barriers, which were crossed in the SMD simulations with the data obtained from the AFM unbinding experiments showed excellent agreement.

## 6 Applications

The detailed knowledge of the unbinding forces and threshold values of DNA-DNA and antibody-antigen interactions has several applications. For example, these interactions can be employed to build up systems of hierarchical forces, thereby allowing more sophisticated approaches for the analysis and manipulation of biological systems at the single molecule level. If such a well-characterized interaction is introduced between the cantilever tip of an AFM and a molecule of interest, it will transmit the force up to a certain threshold value and then open up, thereby defining the maximum force that the molecule of interest will experience. This chapter describes two examples where this concept is used. In the first example (chapter 6.1) a system has been developed which allows the manipulation of an enzyme with an externally applied force while monitoring its activity. In the second example (chapter 6.2) the above-mentioned concept has been applied for the bottom-up assembly of nano-scale functional units in an aqueous ambient medium (39).

### **6.1 Model system for the force-based manipulation of the enzymatic activity of Lipase B from *Candida antarctica* (CaIB)**

In this example the concept of hierarchical forces has been used to apply a force to the enzyme Lipase B from *Candida antarctica* (CaIB) while monitoring its activity. Crucial for this type of experiment is that the applied force does not lead to unfolding of the enzyme. In order to prevent damage on the enzyme due to (irreversible) unfolding, the used antibody-antigen interaction acts as a “fuse”. This fuse was introduced between the cantilever tip and the enzyme thereby ensuring that the fuse will open up before the enzyme unfolds:

$$F_{\text{unfolding}} > F_{\text{fuse}}$$

To real-time monitor the enzymatic turnover while applying the external force, a combined AFM-TIRF (total internal reflection fluorescence microscope) setup was used. The previously characterized 12 amino acid long peptide was

---

attached to CalB, which was immobilized site-specifically to a glass surface. The antibody, which in complex with the peptide represents the fuse, was attached to the tip of a cantilever. Using this measurement set-up, which is sketched in figure 13, CalB can be manipulated by an externally applied force with the AFM. Simultaneously, the fluorescence resulting from single turnover events of the enzyme can be monitored with the TIRF.

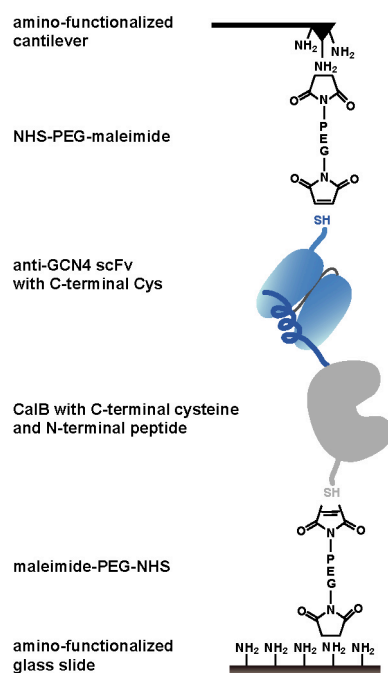


**Figure 13. Measurement set-up for the force-based manipulation of the activity of CalB. The first part of the fuse - the scFv antibody fragment - is attached to the tip of the cantilever. The second part of the fuse - the 12 amino acid long peptide – was attached to the N-terminus of CalB on the genetic level. CalB, which possesses a C-terminal cysteine, is covalently immobilized to the surface.**

The establishment of this complex set-up required several different steps. First, CalB was cloned and expressed in *Escherichia coli*. These results are published in publication P7. Second, a cysteine residue was introduced to the C-terminus of the enzyme, to ensure site-specific and covalent immobilization via a PEG spacer to the glass surface (see chapter 4). The optimized protocol for enzymes is summarized in publication P6. Third, one part of the fuse - the 12 amino acid long peptide – was attached to the N-terminus of CalB. Fourthly,

the second part of the fuse – the antibody scFv fragment – was coupled to the tip of the cantilever again via a PEG spacer. The molecular interaction between the 12 amino acid long peptide and the antibody fragment was analyzed in publication P1 in detail and exhibits threshold forces between 35 pN and 56 pN for loading rates from 50 pN/s to 14350 pN/s. The analysis of the antibody-peptide interaction with a conventional AFM, where the peptide was attached to CalB, showed that CalB does not unfold for these forces, thereby proving that the concept works and that this strategy can be used to perform the desired experiments. The fluorescence measurements with and without an externally applied force have been carried out and will soon be published. In summary, the manipulation of CalB with an externally applied force leads to a higher probability for CalB being in its active state. The performed measurements revealed that CalB turns into its active state 4-5 s after the appliance of an external force.

## 6.2 Single-molecule cut-and-paste surface assembly

In the second example the concept of hierarchical forces has been applied to transfer DNA oligonucleotides from one position on a surface to another, thereby assembling structures with nanometer resolution. These experiments, which are based on the detailed knowledge of the unbinding pathways and threshold forces of oligonucleotides, have recently been published in the paper “Single molecule, Cut-and-Paste Surface Assembly” by Kufer et al. (39).

In more detail, Kufer et al. introduced a new method for the bottom-up assembly of biomolecular structures using single molecule force and fluorescence microscopy. Using the following hierarchy of forces  $F_{\text{depot}} < F_{\text{transfer}} < F_{\text{target}}$  functional units could be picked up from a so-called depot area and transferred to a so-called target area, thereby using complementary DNA strands and an AFM cantilever tip (figure 14).

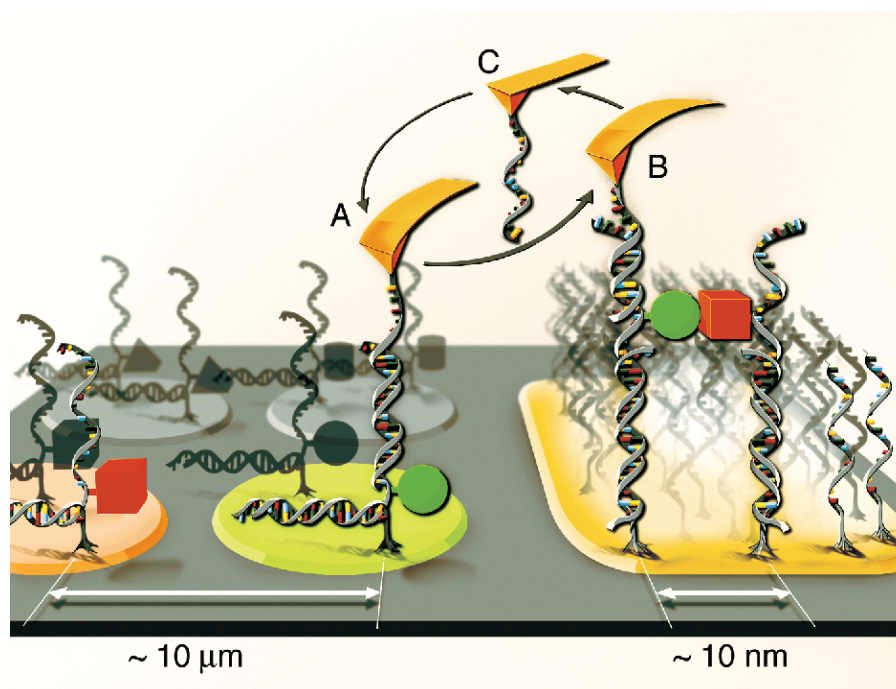


**Figure 14.** Functional units are picked up from discrete storage sites (depot area) with a DNA oligonucleotide attached to the tip of an AFM cantilever and transferred to the target area where they are deposited with high spatial precision (picture from Kufer et al. (39)). A, B and C mark the different steps of the transport. In A, the handle DNA, which is bound to the tip of a cantilever, is hybridized to the target DNA, which in addition is hybridized to a surface bound oligonucleotide in the depot area. In B, the handle DNA still is hybridized to the transfer DNA, which now is hybridized to the target DNA in the target area. C shows the handle DNA bound to the cantilever tip.

These measurements were performed as follows. First, a short DNA oligonucleotide with 30 bases was bound to a surface, containing covalently attached PEG (depot area). This immobilization procedure was carried out as described in publication P2 and P4. Second, a complementary oligonucleotide with an overlap of 20 bases (transfer DNA) containing a covalently bound functional unit (here: the fluorophore rhodamine green), was hybridized to the surface bound DNA in the so-called “unzip-geometry” (see chapter 5). Third, the surface was approached with the tip of a cantilever containing DNA with 20 bases (handle DNA), which is complementary to the overlap of the transfer DNA. This way a duplex can be formed in the so-called “shear-geometry”. If the

cantilever tip is retracted from the surface, the hybridized 30 base pair long DNA duplex in the “unzip-geometry” will open up base pair by base pair at forces of 9-20 pN (42,53) (see chapter 5.1.1), whereas the 20 base pairs of the DNA transfer - DNA handle duplex in the “shear geometry” are loaded in parallel. As stated in chapter 5.1.2.1 and publication P4, the rupture forces of 20 base pair long oligonucleotides revealed loading rate dependent unbinding forces ranging from 45 pN to 55 pN. Therefore, upon retraction of the cantilever tip, the duplex in the “unzip-geometry” will break open with a much higher probability and the transfer DNA, carrying the functional unit, will be bound to the cantilever tip. Once a functional unit is bound to the cantilever tip, it can be moved to a new position (target area). The target area was functionalized with a similar surface chemistry (compared with the depot area) – a PEG spacer and a DNA oligonucleotide with 30 bases (target DNA). The target DNA was chosen to bind to the transfer DNA in “shear-geometry” and to form a duplex, which is longer than the DNA transfer - DNA handle duplex, when the cantilever tip is lowered. Upon retraction of the cantilever tip, both DNA duplexes (20 and 30 base pairs) are set under a gradually increasing force until with a higher probability the weaker of the two complexes ruptures. In publication P4 rupture forces of a 30 base pair long DNA duplex revealed loading rate dependent unbinding forces ranging from 55 pN to 75 pN. In addition, Albrecht et al. (62) showed that a length difference of 10 base pairs is sufficient to make the rupture of the shorter DNA transfer - DNA handle duplex (20 base pairs) more likely by one order of magnitude than the rupture of the longer anchor-duplex (30 base pairs). With this technique, functional units can be transferred and deposited in different locations with high spatial precision. This can be used for the assembly of basic geometrical structures with nanometer resolution from a variety of biomolecular building blocks in order to create new functions (63,64), such as artificial signaling cascades or synergetic combinations of enzymes.

## 7 References

1. Henzler-Wildman, K. and D. Kern. 2007. Dynamic personalities of proteins. *Nature* 450:964-972.
2. Tsai, C. J., B. Ma, Y. Y. Sham, S. Kumar, and R. Nussinov. 2001. Structured disorder and conformational selection. *Proteins* 44:418-427.
3. Kumar, S., B. Ma, C. J. Tsai, N. Sinha, and R. Nussinov. 2000. Folding and binding cascades: dynamic landscapes and population shifts. *Protein Sci* 9:10-19.
4. De Cremer, G., M. B. Roeffaers, M. Baruah, M. Sliwa, B. F. Sels, J. Hofkens, and D. E. De Vos. 2007. Dynamic disorder and stepwise deactivation in a chymotrypsin catalyzed hydrolysis reaction. *J Am Chem Soc* 129:15458-15459.
5. Lu, H. P., L. Xun, and X. S. Xie. 1998. Single-molecule enzymatic dynamics. *Science* 282:1877-1882.
6. Edman, L., Z. Foldes-Papp, S. Wennmalm, and R. Rigler. 1999. The fluctuating enzyme: a single molecule approach. *Chemical Physics* 247:11-22.
7. Velonia, K., O. Flomenbom, D. Loos, S. Masuo, M. Cotlet, Y. Engelborghs, J. Hofkens, A. E. Rowan, J. Klafter, R. J. Nolte, and F. C. de Schryver. 2005. Single-enzyme kinetics of CALB-catalyzed hydrolysis. *Angew. Chem. Int. Edit.* 44:560-564.
8. English, B. P., W. Min, A. M. van Oijen, K. T. Lee, G. Luo, H. Sun, B. J. Cherayil, S. C. Kou, and X. S. Xie. 2006. Ever-fluctuating single enzyme molecules: Michaelis-Menten equation revisited. *Nat Chem Biol* 2:87-94.

9. Evans, E. and K. Ritchie. 1999. Strength of a weak bond connecting flexible polymer chains. *Biophys. J.* 76:2439-2447.
10. Merkel, R., P. Nassoy, A. Leung, K. Ritchie, and E. Evans. 1999. Energy landscapes of receptor-ligand bonds explored with dynamic force spectroscopy. *Nature* 397:50-53.
11. Bustamante, C., Z. Bryant, and S. B. Smith. 2003. Ten years of tension: single-molecule DNA mechanics. *Nature* 421:423-427.
12. Nevo, R., V. Brumfeld, R. Kapon, P. Hinterdorfer, and Z. Reich. 2005. Direct measurement of protein energy landscape roughness. *EMBO Rep* 6:482-486.
13. Barsegov, V. and D. Thirumalai. 2005. Probing protein-protein interactions by dynamic force correlation spectroscopy. *Phys Rev Lett* 95:168302.
14. Kessler, M., K. E. Gottschalk, H. Janovjak, D. J. Muller, and H. E. Gaub. 2006. Bacteriorhodopsin folds into the membrane against an external force. *J Mol Biol* 357:644-654.
15. Rief, M., M. Gautel, F. Oesterhelt, J. M. Fernandez, and H. E. Gaub. 1997. Reversible unfolding of individual titin immunoglobulin domains by AFM. *Science* 276:1109-1112.
16. Oesterhelt, F., D. Oesterhelt, M. Pfeiffer, A. Engel, H. E. Gaub, and D. J. Muller. 2000. Unfolding pathways of individual bacteriorhodopsins. *Science* 288:143-146.
17. Kessler, M. and H. E. Gaub. 2006. Unfolding barriers in bacteriorhodopsin probed from the cytoplasmic and the extracellular side by AFM. *Structure* 14:521-527.

## References

---

18. Bell, G. I. 1978. Models for the specific adhesion of cells to cells. *Science* 200:618-627.
19. Ashkin, A. 1997. Optical trapping and manipulation of neutral particles using lasers. *Proc. Natl. Acad. Sci. USA* 94:4853-4860.
20. Dumont, S., W. Cheng, V. Serebrov, I. Tinoco, A. M. Pyle, and C. Bustamante. 2005. Direct single molecule observation of HCV's RNA helicase at work. *Biophys. J.* 88:350A-351A.
21. Maier, B., D. Bensimon, and V. Croquette. 2000. Replication by a single DNA polymerase of a stretched single-stranded DNA. *Proc Natl Acad Sci U S A* 97:12002-12007.
22. Smith, D. E., S. J. Tans, S. B. Smith, S. Grimes, D. L. Anderson, and C. Bustamante. 2001. The bacteriophage straight phi29 portal motor can package DNA against a large internal force. *Nature* 413:748-752.
23. Rock, R. S., M. Rief, A. D. Mehta, and J. A. Spudich. 2000. In vitro assays of processive myosin motors. *Methods* 22:373-381.
24. Bockelmann, U., P. Thomen, B. Essevaz-Roulet, V. Viasnoff, and F. Heslot. 2002. Unzipping DNA with optical tweezers: high sequence sensitivity and force flips. *Biophys J* 82:1537-1553.
25. Smith, S. B., L. Finzi, and C. Bustamante. 1992. Direct mechanical measurements of the elasticity of single DNA molecules by using magnetic beads. *Science* 258:1122-1126.
26. Strick, T. R., V. Croquette, and D. Bensimon. 2000. Single-molecule analysis of DNA uncoiling by a type II topoisomerase. *Nature* 404:901-904.

27. Binnig, G., C. F. Quate, and C. Gerber. 1986. Atomic Force Microscope. *Phys. Rev. Lett.* 56:930-933.
28. Florin, E. L., V. T. Moy, and H. E. Gaub. 1994. Adhesion forces between individual ligand-receptor pairs. *Science* 264:415-417.
29. Rief, M., F. Oesterhelt, B. Heymann, and H. E. Gaub. 1997. Single Molecule Force Spectroscopy on Polysaccharides by Atomic Force Microscopy. *Science* 275:1295-1297.
30. Grandbois, M., M. Beyer, M. Rief, H. Clausen-Schaumann, and H. E. Gaub. 1999. How strong is a covalent bond? *Science* 283:1727-1730.
31. Neuert, G., C. Albrecht, E. Pamir, and H. E. Gaub. 2006. Dynamic force spectroscopy of the digoxigenin-antibody complex. *FEBS Lett* 580:505-509.
32. Jeon, S. I., J. H. Lee, J. D. Andrade, and P. G. Degennes. 1991. Protein Surface Interactions In The Presence Of Polyethylene Oxide.1. Simplified Theory. *Journal Of Colloid And Interface Science* 142:149-158.
33. Sofia, S. J. and E. W. Merrill. 1997. Protein Adsorption on Poly(ethylene oxide)-Grafted Silicon Surfaces. In *Poly(ethylene glycol) Chemistry and Biological Applications*. J. M. Harris and S. Zalipsky, editors. ACS Symposium Series. Washington, DC. 342-360.
34. Alcantar, N. A., E. S. Aydil, and J. N. Israelachvili. 2000. Polyethylene glycol-coated biocompatible surfaces. *J Biomed Mater Res* 51:343-351.
35. Blank, K., J. Morfill, and H. E. Gaub. 2006. Site-specific immobilization of genetically engineered variants of *Candida antarctica* lipase B. *Chembiochem* 7:1349-1351.

36. Kühner, F., J. Morfill, R. A. Neher, K. Blank, and H. E. Gaub. 2007. Force-induced DNA slippage. *Biophys J* 92:2491-2497.
37. Morfill, J., F. Kühner, K. Blank, R. A. Lugmaier, J. Sedlmair, and H. E. Gaub. 2007. B-S transition in short oligonucleotides. *Biophys J* 93:2400-2409.
38. Morfill, J., K. Blank, C. Zahnd, B. Luginbuhl, F. Kühner, K. E. Gottschalk, A. Plückthun, and H. E. Gaub. 2007. Affinity-matured recombinant antibody fragments analyzed by single-molecule force spectroscopy. *Biophys J* 93:3583-3590.
39. Kufer, S. K., E. M. Puchner, H. Gump, T. Liedl, and H. E. Gaub. 2008. Single-Molecule, Cut-and-Paste Surface Assembly. *Science* 318:594-596.
40. Smith, S. B., Y. J. Cui, and C. Bustamante. 1996. Overstretching B-DNA: The elastic response of individual double-stranded and single-stranded DNA molecules. *Science* 271:795-799.
41. Wang, M. D., H. Yin, R. Landick, J. Gelles, and S. M. Block. 1996. Stretching DNA with optical tweezers. *Biophys. J.* 70:SUP63-SUP63.
42. Rief, M., H. Clausen-Schaumann, and H. E. Gaub. 1999. Sequence-dependent mechanics of single DNA molecules. *Nature Struct. Biol.* 6:346-349.
43. Lebrun, A. and R. Lavery. 1996. Modelling extreme stretching of DNA. *Nucleic Acids Res.* 24:2260-2267.
44. Lebrun, A. and R. Lavery. 1998. Modeling the mechanics of a DNA oligomer. *J Biomol Struct Dyn* 16:593-604.

45. Lavery, R. and A. Lebrun. 1999. Modelling DNA stretching for physics and biology. *Genetica* 106:75-84.
46. Konrad, M. W. and J. I. Bolonick. 1996. Molecular dynamics simulation of DNA stretching is consistent with the tension observed for extension and strand separation and predicts a novel ladder structure. *J. Am. Chem. Soc.* 118:10989-10994.
47. Ahsan, A., J. Rudnick, and R. Bruinsma. 1998. Elasticity theory of the B-DNA to S-DNA transition. *Biophys. J.* 74:132-137.
48. MacKerell, A. D. and G. U. Lee. 1999. Structure, force, and energy of a double-stranded DNA oligonucleotide under tensile loads. *Eur. Biophys. J.* 28:415-426.
49. Marko, J. F. 1997. Stretching must twist DNA. *Europhys. Lett.* 38:183-188.
50. Kosikov, K. M., A. A. Gorin, V. B. Zhurkin, and W. K. Olson. 1999. DNA stretching and compression: Large-scale simulations of double helical structures. *J. Mol. Biol.* 289:1301-1326.
51. Strunz, T., K. Oroszlan, R. Schäfer, and H. J. Güntherodt. 1999. Dynamic force spectroscopy of single DNA molecules. *Proc. Natl. Acad. Sci. USA* 96:11277-11282.
52. Pope, L. H., M. C. Davies, C. A. Laughton, C. J. Roberts, S. J. Tendler, and P. M. Williams. 2001. Force-induced melting of a short DNA double helix. *Eur. Biophys. J.* 30:53-62.
53. Krautbauer, R., M. Rief, and H. E. Gaub. 2003. Unzipping DNA oligomers. *Nano Lett.* 3:493-496.

54. Neher, R. A. and U. Gerland. 2004. Dynamics of force-induced DNA slippage. *Phys. Rev. Lett.* 93:198102.
55. Neher, R. A. and U. Gerland. 2005. DNA as a programmable viscoelastic nanolement. *Biophys. J.* 89:3846-3855.
56. Winter, G., A. D. Griffiths, R. E. Hawkins, and H. R. Hoogenboom. 1994. Making antibodies by phage display technology. *Annu Rev Immunol* 12:433-455.
57. Plückthun, A., C. Schaffitzel, J. Hanes, and L. Jermutus. 2000. In vitro selection and evolution of proteins. *Adv Protein Chem* 55:367-403.
58. Ge, L., A. Knappik, P. Pack, C. Freund, and A. Plückthun. 1995. Expressing Antibodies in *Escherichia coli*. In *Antibody Engineering*. C. A. K. Borrebaeck, editor. 2nd ed ed. Oxford University Press. New York. 229-266.
59. Hanes, J., L. Jermutus, S. Weber-Bornhauser, H. R. Bosshard, and A. Plückthun. 1998. Ribosome display efficiently selects and evolves high-affinity antibodies in vitro from immune libraries. *Proc Natl Acad Sci U S A* 95:14130-14135.
60. Zahnd, C., S. Spinelli, B. Luginbühl, P. Amstutz, C. Cambillau, and A. Plückthun. 2004. Directed in vitro evolution and crystallographic analysis of a peptide-binding single chain antibody fragment (scFv) with low picomolar affinity. *J Biol Chem* 279:18870-18877.
61. Berger, C., S. Weber-Bornhauser, J. Eggenberger, J. Hanes, A. Plückthun, and H. R. Bosshard. 1999. Antigen recognition by conformational selection. *FEBS Lett* 450:149-153.

62. Albrecht, C., K. Blank, M. Lalic-Multhaler, S. Hirler, T. Mai, I. Gilbert, S. Schiffmann, T. Bayer, H. Clausen-Schaumann, and H. E. Gaub. 2003. DNA: a programmable force sensor. *Science* 301:367-370.
63. Grzybowski, B. A., H. A. Stone, and G. M. Whitesides. 2000. Dynamic self-assembly of magnetized, millimetre-sized objects rotating at a liquid-air interface. *Nature* 405:1033-1036.
64. Pellegrino, T., S. Kudera, T. Liedl, A. Munoz Javier, L. Manna, and W. J. Parak. 2005. On the development of colloidal nanoparticles towards multifunctional structures and their possible use for biological applications. *Small* 1:48-63.

## 8 Publications

P1

---

Force-Based Analysis of Multidimensional Energy Landscapes: Application of Dynamic Force Spectroscopy and Steered Molecular Dynamics Simulations to an Antibody-Peptide Complex

J. Morfill, J. Neumann, K. Blank, U. Steinbach, E. M. Puchner, K-E. Gottschalk and H. E. Gaub

*Submitted to Journal of Molecular Biology*

P2

---

Site-specific and covalent immobilization of biomolecules for single molecule experiments

J. Morfill, T. Nicolaus, G. Neuert, H. E. Gaub and K. Blank

*Submitted to Nature Methods*

P3

---

Affinity-Matured Recombinant Antibody Fragments Analyzed by Single Molecule Force Spectroscopy

J. Morfill, K. Blank, C. Zahnd, B. Luginbühl, F. Kühner, K-E. Gottschalk, A. Plückthun and H. E. Gaub

*Biophysical Journal (2007) 93: 3583-3590*

P4

---

B-S Transition in Short Oligonucleotides

J. Morfill, F. Kühner, K. Blank, R. Lügmaier, J. Sedlmair and H. E. Gaub

*Biophysical Journal (2007) 93: 2400-2409*

P5

---

Force induced DNA slippage

F. Kühner, J. Morfill, R. A. Neher, K. Blank and H. E. Gaub

*Biophysical Journal (2007) 92: 2491-2497*

---

P6

---

Site-Specific Immobilization of Genetically Engineered Variants of *Candida Antarctica* Lipase B

K. Blank, J. Morfill and H. E. Gaub

*ChemBioChem* (2006) 7: 1349-1351

P7

---

Functional expression of *Candida antarctica* lipase B in *Escherichia coli*

K. Blank, J. Morfill, H. Gump and H. E. Gaub

*Journal of Biotechnology* (2006) 125: 474-483

Further publications, which are not part of this thesis:

Friction of Single Polymers at Surfaces

F. Kühner, M. Erdmann, L. Sonnenberg, A. Serr, J. Morfill and H. E. Gaub

*Langmuir* (2006) 22: 11180-11186

## **P1**

### **8.1 Force-Based Analysis of Multidimensional Energy Landscapes: Application of Dynamic Force Spectroscopy and Steered Molecular Dynamics Simulations to an Antibody-Peptide Complex**

J. Morfill, J. Neumann, K. Blank, U. Steinbach, E. M. Puchner,  
K-E. Gottschalk and H. E. Gaub

*Submitted to Journal of Molecular Biology*

running title: Unbinding Pathways of an Antibody-Peptide Complex

# **Force-Based Analysis of Multidimensional Energy Landscapes: Application of Dynamic Force Spectroscopy and Steered Molecular Dynamics Simulations to an Antibody-Peptide Complex**

Julia Morfill\*, Jan Neumann\*, Kerstin Blank\*<sup>†</sup>, Uta Steinbach\*, Elias M. Puchner\*, Kay-E. Gottschalk\*, Hermann E. Gaub\*

\* Lehrstuhl für Angewandte Physik & Center for Nanoscience, LMU München, Amalienstrasse 54, D-80799 München, Germany

<sup>†</sup> present address:

Department of Chemistry, Katholieke Universiteit Leuven

Celestijnenlaan 200 F, B-3001 Heverlee, Belgium

Corresponding author: Dr. Kerstin Blank  
Kerstin.Blank@chem.kuleuven.be  
Tel.: +32 16 32 74 47  
Fax: +32 16 32 79 90

## Summary

Multidimensional energy landscapes are an intrinsic property of proteins and define their dynamic behavior as well as their response to external stimuli. In order to explore the energy landscape and its implications on the dynamic function of proteins dynamic force spectroscopy and Steered Molecular Dynamics (SMD) simulations have proven to be important tools. In this study, these techniques have been employed to analyze the influence of the direction of the probing forces on the complex of an antibody fragment with its peptide antigen. Using an atomic force microscope (AFM), experiments were performed where the attachment points of the 12 amino acid long peptide antigen were varied. These measurements yielded clearly distinguishable basal dissociation rates and potential widths proving that the direction of the applied force determines the unbinding pathway. Complementary atomistic SMD simulations were performed, which also show that the unbinding pathways of the system are dependent on the pulling direction. However, the main barrier to be crossed was independent of the pulling direction and is represented by a backbone hydrogen bond between GLY<sup>H</sup>-H40 of the antibody fragment and GLU<sup>O $\epsilon$</sup> -6<sub>peptide</sub> of the peptide. For each pulling direction the observed barriers can be correlated with the rupture of specific interactions, which stabilize the bound complex. Furthermore, although the SMD simulations were performed at loading rates exceeding the experimental ones by orders of magnitude due to computational limitations, a detailed comparison of the barriers, which were overcome in the SMD simulations with the data obtained from the AFM unbinding experiments show excellent agreement.

**Key words:** single molecule force spectroscopy, atomic force microscope, molecular dynamics simulations, energy landscape, antibody-antigen interaction

## Introduction

The knowledge of protein structures revolutionized the understanding of protein function on the atomic level. However, crystal structures provide static pictures and do not account for the fact that proteins are soft materials, which, due to thermal fluctuations sample a large ensemble of slightly different conformations around their average structure. Multidimensional energy landscapes, that define the relative probabilities of the conformational states and the energy barriers between them, are capable to describe the dynamical equilibrium of protein conformations.<sup>1; 2; 3</sup> As a result, the complexation of two proteins forming a protein-protein complex also occurs on these multi-dimensional energy landscapes (figure 1a). The corresponding complexation rates of a protein-protein interaction are determined by the barriers in the underlying energy landscape, that can be influenced by a variety of internal and external factors such as phosphorylation, mutations, or even the action of external forces. All these factors can alter the relative energy barrier height between different substates or even generate new local substates.

Since force is an ideal control parameter to explore multidimensional energy landscapes of proteins (figure 1b), single molecule force spectroscopy experiments have become an important tool for studying the dynamic function of individual proteins and protein-protein complexes.<sup>4; 5; 6; 7; 8; 9; 10</sup> Technically, the application of forces on the single molecule level can be realized using different experimental techniques as well as molecular dynamics simulations. The atomic force microscope (AFM) and laser tweezers have evolved into the most prominent experimental tools for the analysis of the mechanical and dissociation properties of proteins and protein-protein interactions.<sup>11; 12; 13; 14</sup>

In this report, the energy landscape of an antibody-peptide complex was explored using single molecule force spectroscopy and molecular dynamics simulations. We chose this system because the crystal structure of the complex is known<sup>15</sup> and therefore provides the

possibility of explaining the response of this complex to the externally applied force with structural data. The peptide antigen was derived from the leucine zipper domain of the yeast transcription factor GCN4. For the generation of antibodies two proline mutations have been introduced in this 33 amino acid long peptide to prevent coiled coil formation. Using this peptide, mice have been immunized and the mouse antibody genes have been cloned into a ribosome display system to select and improve peptide binders.<sup>15; 16</sup> The used antibody single-chain Fv fragment (scFv; clone H6) was obtained from this affinity maturation process and has been further modified by site-directed mutagenesis. In order to crystallize the complex of scFv fragment and peptide a truncated 12 amino acid long peptide was used, which is recognized by the antibody. The peptide binds to the scFv fragment in an  $\alpha$ -helical conformation facing the scFv fragment with the same side which binds the complementary peptide in the leucine zipper. This region of the peptide corresponds to the so-called trigger sequence, which has been found by Kammerer et al.<sup>17</sup> The trigger region has been shown to be essential for folding and coiled coil formation of the leucine zipper and contains a high  $\alpha$ -helical content.<sup>18</sup> It is considered that the interaction of the two peptides upon coiled coil formation involves assembly of these  $\alpha$ -helical stretches by conformational selection. The identity of interactions in the coiled-coil peptide and interactions between a single peptide and the antibody implies that the binding to the antibody follows a similar mechanism.

For our studies, the peptide antigen opens up the possibility to vary the attachment points of the peptide, since the amino acid for coupling can be easily introduced at different positions. This gives us the possibility to investigate whether the unbinding pathway of the regarded antibody-peptide complex is changed by the direction of the applied force, which would point to the existence of a multidimensional energy landscape. High-resolution atomic force microscope-based single molecule force spectroscopy measurements were performed to determine the basal dissociation rate  $k_{\text{off}}$ , which correlates with the height of the energy barrier, which has to be overcome for unbinding, and the potential width  $\Delta x$ , which is a rough

measure of the width of the binding potential. The obtained results for  $k_{\text{off}}$  were then compared with the  $k_{\text{off}}$  values determined under equilibrium conditions with surface plasmon resonance (SPR).

Complementary, Steered Molecular Dynamics (SMD) simulations were performed to provide additional information about the energy landscape of the respective antibody-peptide system. Furthermore, SMD simulations allow the analysis of the chosen unbinding pathway with atomic resolution.<sup>19; 20; 21; 22</sup> SMD simulations enable the identification of the rupture events and the corresponding molecular interactions correlated with these ruptures. This structural information was related to the results obtained from the AFM measurements.

## Results and Discussion

### Single Molecule Force Spectroscopy

The antibody fragment H6 used in our studies binds the truncated 12 amino acid long peptide antigen corresponding to amino acids 17 to 28 of the wildtype leucine zipper GCN4-p1.<sup>15; 23</sup> However, in this paper the numbering of the structure file (PDB code 1P4B) will be used, which counts the amino acids of the peptide from 1 to 12. To explore the energy landscape of the antibody-peptide complex in detail, force spectroscopy measurements were performed using an atomic force microscope (AFM). For this purpose, the antibody fragment H6 was covalently coupled to a surface containing covalently attached polyethylene glycol (PEG) and the peptide was immobilized onto the cantilever tip in the same way (figure 2). The usage of the elastic spacer PEG minimizes nonspecific interactions and maximizes the probability of detecting specific and single rupture events. Three setups representing different attachment points were analyzed in detail: For setup N a cysteine followed by three glycines was attached to the N-terminus (TYR-1<sub>peptide</sub>; corresponding to amino acid 17 of the full length leucine zipper) in order to couple the peptide to the cantilever of the AFM. For setup M the coupling to the cantilever was achieved via a cysteine, which replaced ALA-8<sub>peptide</sub> (corresponding to amino acid 24 of the full length leucine zipper) in the “middle” of the peptide. It is obvious from the structure of the peptide that ALA-8<sub>peptide</sub> is not involved in interactions with the antibody. And for setup C a spacer of three glycines followed by a cysteine was attached to the C-terminus of the truncated peptide (LYS-12<sub>peptide</sub>; corresponding to amino acid 28 of the full length leucine zipper). In the following, the three different attachment possibilities of the peptide will be abbreviated with N, M and C. In all experiments, the surface was approached with the tip of the cantilever, allowing the antibody-peptide complex to bind. Subsequently, the cantilever was retracted and the antibody-peptide complex was loaded with an increasing force until the complex ruptured and the cantilever

relaxed back into its equilibrium position. The force applied to this complex was recorded as a function of the distance between the cantilever tip and the surface. Figure 3a shows three different force-extension curves, which correspond to the rupture event of the antibody-peptide complex, where the peptide was attached either as shown in N (red), M (green) or C (blue) in figure 2. The force-extension curves measured for the three different setups N, M and C exhibit similar rupture forces. To obtain good statistics, several hundreds of force-extension curves at different retract velocities were recorded using only one cantilever for every setup respectively. The usage of one cantilever per setup is crucial in these experiments to minimize errors originating from the cantilever calibration. From the obtained force-extension curves, the rupture force and the rupture length were determined. Force-time curves revealed the corresponding loading rate. Figures 3b and c show the rupture force and loading rate distributions for setup N, measured at a retract velocity of 800 nm/s. The rupture force histogram was fitted with a Gaussian distribution (black curve) and has a most probable force of 47.3 pN. The Gaussian distribution of the loading rates (plotted logarithmically) (figure 3c) shows a maximum at a loading rate of 1307.8 pN s<sup>-1</sup>. The maxima of the force and the loading rate distributions were determined for a large range of loading rates (from 40 pN s<sup>-1</sup> to 31000 pN s<sup>-1</sup>) for all three setups. In the following step these values were plotted in a force versus loading rate (plotted logarithmically) diagram (figure 4). Following the approach of Evans and coworkers<sup>4</sup>, the basal dissociation rate  $k_{\text{off}}$  and the potential width  $\Delta x$  were determined from a linear fit to the data points in the force versus loading rate diagram (eq. 1). The measurements of setup N resulted in a  $k_{\text{off}}$  of  $(16.9 \pm 1.0) \cdot 10^{-3} \text{ s}^{-1}$  and a  $\Delta x$  of  $(0.82 \pm 0.01) \text{ nm}$ . The denoted errors refer to the constant estimated error of  $\pm 0.2 \text{ pN}$ , which includes the injected noise and oscillations as described in Material and Methods. The values for  $k_{\text{off}}$  and  $\Delta x$  for the maximum and minimum linear fit, which were determined by taking into account the spring constant calibration error, equal:  $(14.5 \pm 1.0) \cdot 10^{-3} \text{ s}^{-1}$  for  $k_{\text{off,max}}$  and  $(0.79 \pm 0.01) \text{ nm}$  for  $\Delta x_{\text{max}}$  and  $(14.8 \pm 1.0) \cdot 10^{-3} \text{ s}^{-1}$  for  $k_{\text{off, min}}$  and  $(0.87 \pm 0.01) \text{ nm}$  for  $\Delta x_{\text{min}}$ . The

obtained values for  $k_{\text{off}}$  and  $\Delta x$ , including their calculated errors, for the setups N, M and C are listed in table 1. The detailed error analysis, as described in Material and Methods, demonstrates that the basal dissociation rates and the potential widths of the three different setups N, M and C can be clearly separated. A comparison of the three different setups shows that setup N possesses the smallest potential width and the fastest basal dissociation rate, which corresponds to the smallest energy barrier in the respective multidimensional energy landscape. In contrast, setup C revealed the largest potential width ( $\Delta x = (1.10 \pm 0.01)$  nm) and the slowest basal dissociation rate ( $k_{\text{off}} = (1.3 \pm 1.0) \cdot 10^{-3} \text{ s}^{-1}$ ), which therefore corresponds to the highest energy barrier of the three measured setups. The values for the basal dissociation rate ( $k_{\text{off}} = (7.6 \pm 1.0) \cdot 10^{-3} \text{ s}^{-1}$ ) and the potential width ( $\Delta x = (0.95 \pm 0.01)$  nm) for setup M are in between the values obtained for setup N and C. Interestingly, the setup with the fastest basal dissociation rate has the smallest potential width (setup N) and the setup with the slowest basal dissociation rate has the largest potential width (setup C). Hence, in our system the distance how far the complex can be stretched before it finally ruptures correlates with the basal dissociation rate. This correlation has been observed before for the interaction of different anti-fluorescein scFv fragments with their antigen fluorescein.<sup>24</sup> For the experiments performed here, this correlation can originate from a different starting conformation of the bound complexes. In this case, the number and strength of the stabilizing interactions would determine the basal dissociation rate and the potential width. Alternatively, the direction of the applied force can result in different unbinding pathways on the multidimensional energy landscape.

## Comparison of the basal dissociation rates (AFM) with SPR data

In order to rule out the existence of different starting conformations, surface plasmon resonance (SPR) measurements were performed to investigate if the attached cysteines (at the N-, C-terminus and the ALA8CYS<sub>peptide</sub> mutation) lead to different conformations of the complex and as a result to differences in the dissociation rates and potential widths. These measurements revealed a dissociation rate of  $(1.5 \pm 0.6) \cdot 10^{-3} \text{ s}^{-1}$  for the peptide with the cysteine at its N-terminus and  $(0.9 \pm 0.2) \cdot 10^{-3} \text{ s}^{-1}$  for the peptide with the cysteine at its C-terminus. SPR measurements using the peptide with the ALA8CYS<sub>peptide</sub> mutation failed due to an insufficient signal. This might be the result of a conformational change in the peptide originating from the mutation. However, the values for the peptides with the cysteine attached at the N- or C-terminus agree within the experimental error. Concluding from these data, the differences in the basal dissociation rates and potential widths, observed with the AFM, do not result from conformational changes in the peptide resulting from the cysteines attached either at the N- or C-terminus.

However, from these experiments it cannot be excluded that the different attachment points lead to a disturbance of the system when performing the AFM measurements. The structure together with the SMD simulations (see below) show that one of the main interactions between the peptide and the scFv fragment is very close to the N-terminal attachment point. Hence, the faster dissociation rate observed for the AFM in comparison to the SPR results might be caused by a partial unfolding of the peptide close to the attachment point, so that the interaction is partially weakened due to the linker used in the AFM measurements.

Although it cannot be ruled out that the immobilization to the AFM cantilever leads to slightly different conformations of the peptide the data suggests that the different basal dissociation rates and potential widths are a consequence of the direction of the applied force. Assuming that indeed the direction of the applied force results in different unbinding

pathways, the obtained values for the basal dissociation rates and potential widths can be explained as follows: Within the experimental error the basal dissociation rate for the peptide with the C-terminal cysteine determined with SPR agrees with the  $k_{\text{off}}$  value obtained for setup C with the AFM. This leads to the conclusion, that the same barrier in the energy landscape is probed. In contrast, setup N revealed a 13-fold higher basal dissociation rate, compared with the SPR value for the peptide with the N-terminal cysteine. This difference can be explained by considering a 2D energy landscape with two energy barriers in the direction of the applied force (figure 5). If no external force is applied, as is the case in SPR measurements, the second higher energy barrier is rate limiting for the unbinding of the antibody-peptide complex. For setup N, the externally applied force tilts the energy landscape (red curve in figure 5) such that the first originally lower energy barrier becomes prominent and is rate limiting. This potentially explains the observed higher dissociation rate with the AFM for setup N compared with the equilibrium measurement.

## Steered Molecular Dynamics Simulations

In order to explore the energy landscape in the high velocity regime and to obtain more structure based information about the energy barriers Steered Molecular Dynamics (SMD) simulations were performed.<sup>8; 19; 20; 21; 22; 25</sup> For all simulations the structure pdb code 1P4B<sup>15</sup> of the truncated 12 amino acid long peptide bound to the antibody domains was used. Corresponding to the AFM experiments, three different attachment points on the peptide were defined (see figure 6). A pulling potential was attached to the peptides N-terminus (setup N; ALA-1<sub>peptide</sub>), its C-terminus (setup C; LYS-12<sub>peptide</sub>) and ALA-8<sub>peptide</sub> (setup M). In contrast to the AFM measurements no additional amino acids were attached to the N- or C-terminus of the peptide and the alanine at position 8 was not replaced with cysteine, which had been necessary for the AFM-based analysis. The pulling potential steered the attached amino acid directly away from the antibody at a speed of  $v_{\text{pull}} = 2$  nm/ns. The all-atom trajectories and the pulling forces for every time step were recorded for every simulation.

For every setup a respective average force-time curve out of 20 trajectories was generated. A characteristic force-time curve with minimal root mean square deviation from the average force-time curve is shown in figures 7, 8 and 9 respectively. At least 65% of all 20 trajectories show the respective main pathway of the average force-time curve and were used for further analysis. For each setup, the average times  $t_i^j$  and average forces  $F_i^j$  ( $i = 1, 2$ , corresponding to the number of the force peak;  $j = N, M, C$ ) were determined by analyzing the force peaks, which indicate the positions of the major rupture events in the unbinding pathways. The given errors were calculated as Gaussian errors.

In setup N, the peptide is zipped off the antibody starting from its N-terminal end. Here, two main barriers have been identified (figure 7, table 2). The first barrier is crossed after  $t_1^N = (440 \pm 25)$  ps with a mean force of  $F_1^N = (567 \pm 25)$  pN and corresponds to the rupture of a hydrophobic contact between the amino acids TYR-L40 and LEU-3<sub>peptide</sub>. For the first rupture event a rupture length of  $\Delta r_1^N = (0.88 \pm 0.05)$  nm was detected. The pathway, which involves

this interaction, is taken in 75% of all trajectories. The second rupture event occurs after  $t_2^N = (860 \pm 28)$  ps with a mean force of  $F_2^N = (716 \pm 23)$  pN. For this second rupture event, the rupture length equaled  $\Delta r_2^N = (1.72 \pm 0.06)$  nm. The force peak, which corresponds to the second main barrier crossing and appears in 65% of all trajectories, results from the rupture of the H-bond between  $\text{GLU}^{\text{O}\epsilon}\text{-6}_{\text{peptide}}$  and the backbone hydrogen  $\text{GLY}^{\text{H}}\text{-H40}$ . The last contact for the unbinding process is formed by  $\text{ASN-L69}$ ,  $\text{ARG-L70}$ ,  $\text{ARG-9}_{\text{peptide}}$  and  $\text{LEU-10}_{\text{peptide}}$ .

In setup M, the peptide is separated from the antibody in a double zipper mode, which leads to breakage of two stabilizing interactions next to the steered amino acid (figure 8). Nevertheless, only one major force peak can be identified after an average pulling time of  $t_1^M = (319 \pm 9)$  ps (corresponding to a rupture length of  $\Delta r_1^M = (0.64 \pm 0.02)$  nm) at an average force of  $F_1^M = (1161 \pm 28)$  pN (table 2). The main barrier can be clearly identified as the rupture of the H-bond between  $\text{GLY}^{\text{H}}\text{-H40}$  and  $\text{GLU}^{\text{O}\epsilon}\text{-6}_{\text{peptide}}$  (in 95% of all trajectories). This interaction also causes the second rupture event in the majority of trajectories in setup N (figure 7, table 2). Subsequent to this H-bond rupture, after a mean time of additional  $\Delta t^M = (40 \pm 8)$  ps (corresponding to  $\Delta r^M = (0.08 \pm 0.02)$  nm), the double H-bond between  $\text{ASP}^{\text{O}\delta\text{i}}\text{-H137}$  and  $\text{ARG}^{\text{H}\zeta\text{i}}\text{-9}_{\text{peptide}}$  ( $i = 1, 2$ ) ruptures (figure 8) without a resolvable additional force peak. The last contact for the unbinding process in setup M is formed via  $\text{ASN-L68}$ ,  $\text{ASN-L69}$  and  $\text{LYS-11}_{\text{peptide}}$  on the C-terminal side. The last contact on the N-terminal side of the peptide ruptures shortly before the C-terminal last contact between  $\text{LEU-3}_{\text{peptide}}$  and  $\text{HIS-2}_{\text{peptide}}$  of the peptide and  $\text{ASN-L68}$ ,  $\text{ASP-H33}$  and  $\text{LEU-H110}$  of the scFv fragment.

In setup C, the peptide is zipped off starting from its C-terminal end. Again, two main force peaks can be identified. The first force peak was detected after  $t_1^C = (514 \pm 20)$  ps (corresponding to a rupture length of  $r_1^C = (1.03 \pm 0.04)$  nm) at a mean force of  $F_1^C = (775 \pm 28)$  pN. This force peak coincides with the opening of the stabilizing backbone H-bond of the first peptide helix loop between  $\text{VAL-7}_{\text{peptide}}$  and  $\text{LEU-10}_{\text{peptide}}$ . Hence, the first major rupture event refers to the opening of the secondary structure of the peptide and not to the breakage of

a peptide-antibody bond. The main unbinding pathway is probed in 85% of all trajectories. The second barrier crossing occurred after an average time of  $t_2^C = (750 \pm 45)$  ps with an average rupture length of  $r_2^C = (1.50 \pm 0.09)$  nm and an average force of  $F_2^C = (720 \pm 21)$  pN. This force peak is again determined by the rupture of the H-bond between GLY<sup>H</sup>-H40 and GLU<sup>O $\epsilon$</sup> -6<sub>peptide</sub> (figure 9, table 2). 65% of all trajectories crossed this second barrier via the main unbinding pathway. The last contact for the unbinding process of setup C is formed via HIS-2<sub>peptide</sub>, LEU-3<sub>peptide</sub>, THR-L32, THR-L67, ASN-L68 and ASN-L69.

The three setups underline the importance of the H-bond between the backbone of GLY<sup>H</sup>-H40 and GLU<sup>O $\epsilon$</sup> -6<sub>peptide</sub>: The breakage of this bond is a dominant rupture event in the majority of all trajectories independent of the pulling vector. The setups N and C, where the peptide unbinds in a single zipper mode, show two main rupture events. In setup N, the first force peaks occurs earlier ( $t_1^N < t_1^C$ ) and at lower forces ( $F_1^N < F_1^C$ ) with respect to setup C. In setup C the second force peak occurs earlier ( $t_2^N > t_2^C$ ) but at higher forces ( $F_2^N < F_2^C$ ) than in setup N. The first force peak results from different molecular interactions in setup N and C, whereas the second force peak corresponds to the same molecular interaction of GLY<sup>H</sup>-H40 and GLU<sup>O $\epsilon$</sup> -6<sub>peptide</sub> in both setups. Furthermore, this interaction is also responsible for the force peak in setup M.

## Comparison of SMD and AFM results

Both, simulation and experiment, probe the respective antibody-peptide complex at the same positions on the peptide thereby exerting forces into the same directions. Yet, SMD simulations, due to computational limitations, probe the system at much higher loading rates.<sup>22; 26</sup> Hence, thermal relaxation occurs only partially. The system lacks the time to relax orthogonally to the pulling direction and resulting from this, lacks the time to explore the energy landscape locally to find the optimal pathway to cross the barrier.<sup>26</sup> This might lead to a steeper pathway on the energy landscape potentially crossing higher barriers and finally resulting in higher rupture forces. Whereas higher rupture forces have been observed for all setups, this effect is most dominant for setup M, which unbinds in a double zipper mode (nearly simultaneous rupture of two bonds). In the simulations, as soon as the first important interaction breaks (H-bond GLY<sup>H</sup>-H40, which binds GLU<sup>O $\epsilon$</sup> -6<sub>peptide</sub>), the more stable double H-bond of the interaction between ASP<sup>O $\delta$ i</sup>-H137 and ARG<sup>H $\zeta$ i</sup>-9<sub>peptide</sub> ( $i = 1, 2$ ) experiences the full load and ruptures within 40 ps (figure 8). In contrast, in the AFM experiments, the system can relax orthogonally to the applied force and can re-arrange after the first breakage. As a result, after the first breakage the complex might become so unstable that dissociation occurs on a timescale faster as can be observed with the AFM.

Furthermore, the ALA8CYS mutation in the peptide used in the AFM experiments may lead to additional disturbances of the peptide structure, which may result in a lower stability of the complex. The mutation lies in that region of the peptide with the highest probability for  $\alpha$ -helix formation and mutations at this position have been shown to have an influence on the leucine zipper stability.<sup>27; 28</sup> This contribution of the mutation is very likely, as the peptide containing the mutation, also shows a very weak interaction in the SPR measurements, which is indicative for a destabilized peptide.

A more detailed comparison of the values, obtained from the AFM experiments and the SMD simulations allows the explanation of the energy barriers on the unbinding pathways for

the respective setups. The comparison of the potential widths, obtained with the AFM and the rupture lengths obtained from the SMD simulations shows that the rupture lengths for setup N and C for the first barrier crossing of the main unbinding pathway ( $r_1^N$ ,  $r_1^C$ ) are in good agreement with the potential widths obtained with the AFM ( $\Delta x^N$ ,  $\Delta x^C$ ) (table 1, 2). Hence, the AFM experiments probe the first barrier observed in the SMD simulations (figure 10). Again, for setup M the observed differences might result from the different relaxation due to different time regimes and additionally from the potentially destabilizing mutation, as discussed above.

Furthermore, the SMD simulations provide further evidence for the existence of a second energy barrier, which could not be shown unambiguously from the AFM and SPR data. The forces needed to overcome the second barrier of the main unfolding pathway are of the same order of magnitude as for the first barrier crossing. Yet, the second rupture event for setup N and C occurs at nearly twice the distance of the first rupture event (table 2). Hence, the second energy barrier of the main unfolding pathway in the energy landscape has a large potential width. Outer barriers are much more influenced by externally applied forces than inner barriers due to the tilted energy landscape. Because of this large potential width of the second barrier observed in the SMD simulations, it is plausible that this barrier is not probed in the AFM, even at the lowest applied loading rates. Therefore, the existence of two energy barriers is not in conflict with the observation that the AFM data could be fitted with a straight line in the force versus loading rate plot in figure 4.

The SMD data do not only explain the observed potential widths in the different experimental setups, they also provide more information about the basal dissociation rates of the first barrier crossing which have been obtained from the AFM measurements. As stated earlier, the results from the SMD simulations show, that the first barrier crossing in setup C occurs at a longer rupture length ( $r_1^C > r_1^N$ ) and at a higher force ( $F_1^C > F_1^N$ ) than in setup N. Since the forces measured with the SMD simulations correspond to the slope of the energy

barrier in the energy landscape, the higher forces observed in setup C result from a steeper energy barrier. This steeper energy barrier together with the longer rupture length indicates that the first energy barrier of the main unbinding pathway is higher in setup C than in setup N. A higher energy barrier corresponds to a lower dissociation rate. Hence, if - as already concluded from the comparison of AFM and SPR - the inner energy barrier is rate determining for the AFM experiments (figure 5), both experiment and simulation agree on a lower dissociation rate for setup C compared with the dissociation rate for setup N ( $k_{\text{off}, 1}(\text{C}) < k_{\text{off}, 1}(\text{N})$ ).

## Conclusions

A well-characterized antibody antigen interaction has been chosen to explore the underlying energy landscape with a combination of different techniques. The main focus was to investigate if different pulling directions lead to different unbinding pathways and therefore provide a more detailed insight into the unbinding process of the analyzed interaction. For every pulling direction two rupture events were detected with the SMD simulations. One rupture event in each setup is determined by the same molecular bond, whereas the other rupture event originates from the breakage of different bonds. These findings clearly show that the underlying energy landscape is multidimensional. This information could not be obtained from the AFM measurements only, which show a linear dependence of the rupture forces on the logarithm of the loading rate – a feature, which is characteristic for a two-state system with only one barrier. However the comparison of AFM and SPR point to the existence of at least one more barrier. SPR always probes the lowest energy barrier in the energy landscape. When performing AFM measurements, the complex might be forced to follow a steeper unbinding pathway, which would result in a lower dissociation rate (corresponding to a higher barrier). But, as stated earlier, the basal dissociation rate for setup N obtained with the AFM is higher than the  $k_{\text{off}}$  value obtained with SPR. This leads to the conclusion, that the energy barrier probed with the AFM is lower than the energy barrier, which has to be overcome under equilibrium conditions. Therefore, an additional energy barrier has to exist along the pulling direction of setup N (figure 5), which is not detectable with the AFM. The results from the SMD simulations further support this conclusion since the outer (second) barrier has a very large potential width so that the inner (first) barrier is most likely rate determining even at smallest loading rates. For setup C, the SMD simulations also show a second barrier, which is considered to be lower than the first barrier. Therefore this second barrier is not probed experimentally.

In conclusion, the experimental setup chosen for the AFM measurements, which allows the site-specific immobilization of the binding partners, clearly shows that the direction of the applied force defines the unbinding pathway on a multidimensional energy landscape. This finding clearly points out that non(site)-specific coupling procedures provide a simplified picture about the molecular interactions as the contributions of different unbinding pathways are averaged out.

## Materials and Methods

### Preparation of the peptides and the scFv fragment

Peptides representing a truncated version of the GCN4-p1 leucine zipper Y<sub>1</sub>HLENEVA<sub>8</sub>RLKK<sub>12</sub> were obtained from Jerini Peptide Technologies GmbH, Berlin, Germany. Cysteines have been introduced at different positions during solid phase synthesis to provide site-specific attachment points for the immobilization to the cantilever (figure 2): NH<sub>2</sub>-CGGGYHLENEVARLKK-amide (setup N), NH<sub>2</sub>-YHLENEVCRLK-amide (setup M), NH<sub>2</sub>-YHLENEVARLKKGGGC-amide (setup C).

The expression and purification of the scFv fragment H6 was carried out as described earlier.<sup>29</sup> Briefly, the scFv fragment H6 was expressed with a C-terminal His tag followed by a cysteine to allow a site-specific immobilization. The plasmid for the periplasmic expression in *E. coli* is based on the pAK series.<sup>30</sup> The gene for coexpression of the periplasmic chaperone Skp was introduced.<sup>31</sup> The original His tag was replaced by a tag of six histidines followed by two glycines and a cysteine. For the expression and purification of H6, the protocol of Hanes et al.<sup>16</sup> was slightly modified. In short, the bacteria with the transformed plasmid were grown at 25 °C in SB medium (20 g l<sup>-1</sup> tryptone, 10 g l<sup>-1</sup> yeast extract, 5 g l<sup>-1</sup> NaCl, 50 mM K<sub>2</sub>HPO<sub>4</sub>) containing 30 µg ml<sup>-1</sup> chloramphenicol. Expression was induced with 1 mM isopropyl-β-D-thiogalactopyranoside (IPTG) at an OD<sub>600</sub> between 1.0 and 1.5. The cells were harvested 3 h after induction by centrifugation. Cell disruption was achieved by French Press lysis. The scFv fragment H6 was purified using two chromatography steps. After chromatography on a Ni<sup>2+</sup>-NTA column (Qiagen, Hilden, Germany) using standard protocols the eluted fraction was directly loaded onto an affinity column with immobilized antigen. The fractions from the affinity column were dialyzed against coupling buffer (50 mM sodium phosphate pH 7.2, 50 mM NaCl, 10 mM EDTA) and concentrated using Centricon YM-10 (Millipore, Eschborn, Germany). The actual concentration of the purified scFv fragment H6

was determined by measuring the absorbance at 280 nm. The extinction coefficient was calculated using the program Vector NTI (Invitrogen, Karlsruhe, Germany). The preparation of the purified protein was adjusted to a concentration of  $0.8 \text{ mg ml}^{-1}$  and stored in aliquots at  $-80 \text{ }^{\circ}\text{C}$ .

### **Preparation of slides and cantilevers for the AFM measurements**

Poly(ethylene) glycol (PEG) was used as a spacer between the biomolecules and the surfaces. PEG is an ideal spacer for force spectroscopy measurements<sup>24; 32; 33; 34; 35; 36; 37</sup>, as it provides protein resistant surfaces<sup>38</sup>, thereby reducing the number of non-specific binding events. In addition, PEG shows a characteristic force-extension curve allowing the discrimination between specific and non-specific interactions during data analysis. The scFv fragment H6 possessing a C-terminal cysteine was immobilized on an amino-functionalized slide using a hetero-bifunctional NHS-PEG-maleimide (MW = 5000 g/mol; Nektar, Huntsville, Alabama). The three peptides were separately immobilized via their introduced cysteine to an amino-functionalized cantilever, again using the NHS-PEG-maleimide spacer (figure 2).

In detail, the cantilevers (Bio-lever, Olympus, Tokyo, Japan) were activated with a ten-minute UV-Ozone cleaning treatment and amino modified with 3-aminopropyl-dimethylethoxysilane (ABCR GmbH, Karlsruhe, Germany) as described previously.<sup>29; 35; 36</sup> For the immobilization of the scFv fragment H6 commercially available amino-functionalized slides (Slide A, Nexterion, Mainz, Germany) were used. For the next steps, both surfaces (slide and cantilever) were treated in parallel as described in.<sup>39</sup> Briefly, they were incubated in borate buffer, pH 8.5, in order to increase the fraction of unprotonated amino groups for coupling to the NHS groups of the PEG. NHS-PEG-maleimide was dissolved at a concentration of 50 mM in borate buffer at pH 8.5 and incubated on the surfaces for one hour. In parallel, one of the peptides and the scFv fragment H6 were reduced using TCEP beads

(Perbio Science, Bonn, Germany) in order to generate free thiols. After washing both surfaces with ultrapure water, a solution of the peptide (200  $\mu$ M) was incubated on the cantilever and a solution of the scFv fragment H6 (0.13 mg/ml) was incubated on the slide for one hour. Finally, both surfaces were rinsed with PBS (10 mM Na phosphate, pH 7.4, 137 mM NaCl, 2.7 mM KCl) to remove non-covalently bound material and stored in PBS until use.

### **Force spectroscopy**

All force measurements were performed with a MFP-1D atomic force microscope (AFM) (Asylum Research, Santa Barbara, USA) at room temperature in PBS. Cantilever spring constants equaled 8.7 pN/nm for the measurement of setup N (see figure 2), 3.4 pN/nm for the measurement of setup M and 4.2 pN/nm for the measurement of setup C (B-Bio-Lever) and were obtained as described previously.<sup>40; 41</sup> During the experiments the approach and retract velocity were held constant, whereas the applied force was adjusted by changing the distance between the cantilever tip and the surface to obtain single binding events. To achieve good statistics, several hundred approach-retract cycles were carried out. To obtain measurements over a broad range of different loading rates, every experiment was carried out for different retract velocities ranging from 50 nm/s to 10  $\mu$ m/s.

### **Data extraction**

The obtained data was converted into force-extension curves. From these force-extension curves, the rupture force (the force at which the antibody-antigen complex ruptures) and the rupture length were determined using the program Igor Pro 5.0 (Wavemetrics, Lake Oswego, Oregon, USA) and a custom-written set of procedures. The corresponding loading rate was determined from the force-time curves. The rupture force was determined as described previously.<sup>4; 42</sup> The loading rate was determined using the two-state freely jointed chain fit to the force-extension curve, according to previous studies.<sup>43</sup>

## Data analysis

To analyze the data set obtained from one experiment, which was recorded at a constant retract velocity, the rupture forces, the rupture lengths and the loading rates were plotted in three histograms. These histograms were analyzed with a method based on the so-called Bell-Evans-model.<sup>4; 44</sup> The rupture force and loading rate (plotted logarithmically) histograms for each data set, i.e. for each retract velocity, were fitted with a Gaussian distribution to determine the maxima. Finally, these obtained maxima of the Gaussian distributions were plotted in a force versus loading rate diagram. The maximum force (from the Gaussian distribution of the rupture force histogram) represents the most probable force  $F^*$ :

$$(1) \quad F^* = \frac{k_B \cdot T}{\Delta x} \ln \frac{\dot{F} \cdot \Delta x}{k_B \cdot T \cdot k_{\text{off}}}$$

with  $k_B$  = the Boltzmann constant,  $T$  = the temperature,  $\Delta x$  = the potential width,  $k_{\text{off}}$  = the basal dissociation rate at zero force and  $\dot{F} = \frac{dF}{dt}$  = the loading rate. From a linear fit of the force versus loading rate (pictured logarithmically) plot and eq. 1,  $\Delta x$  and  $k_{\text{off}}$  of the antibody-antigen complex can be determined from the slope and the intercept of the linear fit with the abscissa.

## Error estimation

To calculate the performed error of the dissociation rate  $k_{\text{off}}$  and the potential width  $\Delta x$ , the following assumptions were made:

- i.) The error in the calibration of the spring constant constitutes 10 %.

ii.) Injected noise and oscillations lead to an error of  $\pm 0.2$  pN in the measured rupture force. This value was estimated from the integration of the frequency spectrum of the cantilever in PBS to a frequency of 10 Hz.

As described above,  $k_{\text{off}}$  and  $\Delta x$  can be calculated from the linear fit to the data points in the force vs. loading rate diagram. Due to the usage of only one cantilever for all data points, the error, originating from the calibration of the spring constant, leads to systematic higher or lower rupture forces and loading rates and therefore to higher or lower most probable rupture forces and loading rates. We therefore determined the maximum and minimum linear fit. From these two fits, the maximum and minimum  $k_{\text{off}}$  and  $\Delta x$  can be calculated. In addition, the estimated value of  $\pm 0.2$  pN, was taken into account. This error is not systematic and therefore can be added or subtracted from the most probable rupture force. By using a random generator, a mean linear fit was calculated. From this we gained a mean value for  $k_{\text{off}}$  and  $\Delta x$  with the corresponding standard deviation. This procedure was applied to the original, the maximum and the minimum linear fit in the force versus loading rate plot to receive the maximum and minimum  $k_{\text{off}}$  and  $\Delta x$  with their corresponding standard deviations.

### **Proof of specificity**

To prove the specificity of the force spectroscopy measurements, experiments were performed, either without the antibody fragment or without the peptide. By measuring the antibody fragment H6, attached to the surface, against a cantilever tip passivated with PEG, more than 1000 force-extension curves were recorded. Thereby, less than 1% non-specific interactions were detected. The measurements without the peptide led to similar results.

### **SPR measurements**

The measurements of  $k_{\text{off}}$  (25°C) of the scFv fragment H6 and the peptide either with a cysteine at its N- or C-terminus were performed with a Biacore X instrument (BIAcore,

Freiburg, Germany). For this purpose a CM5 sensor chip (BIAcore) was modified via amine coupling according to the manufacturer's protocol. Clone H6 was diluted in immobilization buffer (10 mM Na-Acetat, pH 5.0) to a final concentration of 11.4 ng/ $\mu$ l and injected on the chip. The final signal intensity on the surface equaled  $\sim$ 200 RU. A series of the respective peptide solutions in PBS buffer in the range of 1.64 - 400 nM was injected on the chip. After binding, dissociation was followed at a flow rate of 50  $\mu$ l/min. The dissociation phase was fitted globally, using the single exponential fit function of the program BIAEvaluation 3.2.

### **Molecular dynamics simulations**

All molecular dynamics (MD) simulations were based on the 2.35 Å resolution X-ray structure 1P4B<sup>15</sup> of the antibody scFv fragment bound to the peptide AH<sub>1</sub>LENEVA<sub>8</sub>RLKK<sub>12</sub>. During this paper the amino acids of the antibody will be labelled <three-letter-code of the amino acid><location in the V<sub>H</sub> or V<sub>L</sub> domain><position in the 1P4B PDB structure>. The amino acids of the peptide will be labelled as a combination of the three-letter-code and the number of the amino acid in the full-length wildtype GCN4 peptide. To distinguish between antibody and peptide amino acids, the residues of the peptide will be added an additional “peptide” in a low placed position.

The first amino acid of the 1P4B pdb structure differs from the experimentally used amino acid. We chose not to mutate the sequence to match the experimental one, because this would have reduced the resolution of the structure. The influence of this sequential difference will not be significant since it is located at the non-interacting end of the peptide.

All MD simulations were performed using the software GROMACS.<sup>45; 46; 47</sup> We used periodic boundary conditions, the OPLS-AA force field<sup>48</sup> and SPC/E water<sup>49</sup> for all MD simulations. For all simulations first one energy-minimized, equilibrated and pre-oriented state of the proteins solved in water was generated. This initial structure was then assigned to new

Boltzmann distributed velocities and again shortly equilibrated before the SMD simulations were performed.

### **System preparation**

The antibody-peptide structure 1P4B was preoriented with the helical peptide axis parallel to the z-axis of the system. Then the molecules were solvated in a 6.8x6x11.6 nm<sup>3</sup> waterbox (16034 H<sub>2</sub>O) ionized with 45 Na<sup>+</sup> and 43 Cl<sup>-</sup> atoms. The overall charge of the system is neutral.

Steepest descent energy minimization was performed with a maximum step size of 0.01 nm up to a precision of 2000 kJ/(mol·nm). No pressure or temperature coupling was used. The cut-off radius for Coulomb and van-der-Waals interactions was set to 1nm.

Afterwards, a water relaxation simulation of 200 ps was performed. On all protein atoms a positional restraint was placed using a harmonic potential with a force constant of 2000 kJ/(mol·nm<sup>2</sup>) = 3.32 nN/nm on the protein atoms. The LINCS algorithm<sup>50</sup> was used on all bond constraints. Protein and non-protein atoms were separately coupled to a heat bath of 300 K using a time constant of 0.1 ps.

All further simulations were performed using Fast Particle-Mesh Ewald electrostatics (PME) with an order of four and a van-der-Waals cut-off of 1.0 nm. A 1 ns equilibration of the whole system followed. A leapfrog algorithm with a time step of 2 fs was used. All C<sub>α</sub> atoms were restrained with a harmonic potential of 1000 kJ/(mol·nm) = 1.8 nN/nm to avoid an unwanted rotation of the system. The restraint potential was weak enough to allow small conformational changes of the backbone due to the equilibration. The side chains were not restricted and therefore freely equilibrating. The RMSD (nm) fit of the C<sub>α</sub>-position reached a stable plateau within this equilibration (data not shown). The temperature was restricted to 300 K analogues

to the last step. The resulting structure was used as the initial structure for all setups to allow a better comparison of the results. Before the actual SMD simulations were performed, for each simulation new random Boltzmann distributed velocities were assigned and an additional 200 ps pre-equilibration was performed.

## Simulations

In every SMD simulation the antibody was fixed in space via a COM movement removal of the chain  $V_H$  of the antibody. In each setup a different  $C_\alpha$  atom was steered away from the antibody (into x-direction) with a harmonic potential using a spring constant of  $k = 1600 \text{ kJ}/(\text{mol}\cdot\text{nm}^2) = 2.66 \text{ nN}/\text{nm}$ . This steering was executed for 3 ns at a speed of  $v_{\text{pull}} = 2 \text{ nm}/\text{ns}$  resulting in a final separation of 6 nm. The strong steering potential forces the attached atom to follow it closely. No other atom of the peptide is restricted in any way, leaving it to respond freely on the forced movement of the attached atom.

Three different setups were tested in correspondence to the AFM experiments. In setup N, the  $C_\alpha$  atom of the N-terminal alanine ALA-1<sub>peptide</sub> of the antigen peptide was attached to the steering potential. In setup C the  $C_\alpha$  atom of the C-terminal amino acid LYS-12<sub>peptide</sub> was attached and in the setup M the  $C_\alpha$  atom of the 8<sup>th</sup> amino acid ALA-8<sub>peptide</sub> was attached. In contrast to the AFM experiments no mutations in setup M were performed, because no cysteine for external linkage was needed in the SMD simulations.

## **Acknowledgements**

The authors thank Dr. Torsten Pirch and Prof. Dr. Kirsten Jung for the SPR data and Prof. Dr. Andreas Plückthun for the gift of the expression vector of the antibody fragment. This work was supported by the Center for Integrative Protein Science Munich, the European Union, the Deutsche Forschungsgemeinschaft and the Fonds der Chemischen Industrie.

## References

1. Henzler-Wildman, K. & Kern, D. (2007). Dynamic personalities of proteins. *Nature* **450**, 964-72.
2. Tsai, C. J., Ma, B., Sham, Y. Y., Kumar, S. & Nussinov, R. (2001). Structured disorder and conformational selection. *Proteins* **44**, 418-27.
3. Kumar, S., Ma, B., Tsai, C. J., Sinha, N. & Nussinov, R. (2000). Folding and binding cascades: dynamic landscapes and population shifts. *Protein Sci* **9**, 10-9.
4. Evans, E. & Ritchie, K. (1999). Strength of a weak bond connecting flexible polymer chains. *Biophys. J.* **76**, 2439-47.
5. Merkel, R., Nassoy, P., Leung, A., Ritchie, K. & Evans, E. (1999). Energy landscapes of receptor-ligand bonds explored with dynamic force spectroscopy. *Nature* **397**, 50-3.
6. Bustamante, C., Bryant, Z. & Smith, S. B. (2003). Ten years of tension: single-molecule DNA mechanics. *Nature* **421**, 423-7.
7. Nevo, R., Brumfeld, V., Kapon, R., Hinterdorfer, P. & Reich, Z. (2005). Direct measurement of protein energy landscape roughness. *EMBO Rep* **6**, 482-6.
8. Barsegov, V. & Thirumalai, D. (2005). Probing protein-protein interactions by dynamic force correlation spectroscopy. *Phys Rev Lett* **95**, 168302.
9. Kessler, M., Gottschalk, K. E., Janovjak, H., Muller, D. J. & Gaub, H. E. (2006). Bacteriorhodopsin folds into the membrane against an external force. *J Mol Biol* **357**, 644-54.
10. Bornschlöggl, T. & Rief, M. (2006). Single molecule unzipping of coiled coils: sequence resolved stability profiles. *Phys Rev Lett* **96**, 118102.

11. Evans, E., Ritchie, K. & Merkel, R. (1995). Sensitive force technique to probe molecular adhesion and structural linkages at biological interfaces. *Biophys J* **68**, 2580-7.
12. Rief, M., Gautel, M., Oesterhelt, F., Fernandez, J. M. & Gaub, H. E. (1997). Reversible unfolding of individual titin immunoglobulin domains by AFM. *Science* **276**, 1109-12.
13. Oesterhelt, F., Oesterhelt, D., Pfeiffer, M., Engel, A., Gaub, H. E. & Muller, D. J. (2000). Unfolding pathways of individual bacteriorhodopsins. *Science* **288**, 143-6.
14. Kessler, M. & Gaub, H. E. (2006). Unfolding barriers in bacteriorhodopsin probed from the cytoplasmic and the extracellular side by AFM. *Structure* **14**, 521-7.
15. Zahnd, C., Spinelli, S., Luginbühl, B., Amstutz, P., Cambillau, C. & Plückthun, A. (2004). Directed in vitro evolution and crystallographic analysis of a peptide-binding single chain antibody fragment (scFv) with low picomolar affinity. *J. Biol. Chem.* **279**, 18870-7.
16. Hanes, J., Jermutus, L., Weber-Bornhauser, S., Bosshard, H. R. & Plückthun, A. (1998). Ribosome display efficiently selects and evolves high-affinity antibodies in vitro from immune libraries. *Proc. Natl. Acad. Sci. USA* **95**, 14130-5.
17. Kammerer, R. A., Schulthess, T., Landwehr, R., Lustig, A., Engel, J., Aebi, U. & Steinmetz, M. O. (1998). An autonomous folding unit mediates the assembly of two-stranded coiled coils. *Proc Natl Acad Sci U S A* **95**, 13419-24.
18. Myers, J. K. & Oas, T. G. (1999). Reinterpretation of GCN4-p1 folding kinetics: partial helix formation precedes dimerization in coiled coil folding. *J Mol Biol* **289**, 205-9.
19. Grubmüller, H. (1995). Predicting slow structural transitions in macromolecular systems: Conformational flooding. *Phys Rev E Stat Phys Plasmas Fluids Relat Interdiscip Topics* **52**, 2893-2906.

20. Sotomayor, M. & Schulten, K. (2007). Single-molecule experiments in vitro and in silico. *Science* **316**, 1144-8.
21. Grubmüller, H. (2005). Force probe molecular dynamics simulations. *Methods Mol Biol* **305**, 493-515.
22. Rief, M. & Grubmüller, H. (2002). Force spectroscopy of single biomolecules. *Chemphyschem* **3**, 255-61.
23. O'Shea, E. K., Klemm, J. D., Kim, P. S. & Alber, T. (1991). X-ray structure of the GCN4 leucine zipper, a two-stranded, parallel coiled coil. *Science* **254**, 539-44.
24. Schwesinger, F., Ros, R., Strunz, T., Anselmetti, D., Güntherodt, H. J., Honegger, A., Jermutus, L., Tiefenauer, L. & Plückthun, A. (2000). Unbinding forces of single antibody-antigen complexes correlate with their thermal dissociation rates. *Proc. Natl. Acad. Sci. USA* **97**, 9972-7.
25. Gao, M., Wilmanns, M. & Schulten, K. (2002). Steered molecular dynamics studies of titin I1 domain unfolding. *Biophys J* **83**, 3435-45.
26. Evans, E. & Ritchie, K. (1997). Dynamic strength of molecular adhesion bonds. *Biophys J* **72**, 1541-55.
27. Holtzer, M. E., Lovett, E. G., d'Avignon, D. A. & Holtzer, A. (1997). Thermal unfolding in a GCN4-like leucine zipper: <sup>13</sup>C alpha NMR chemical shifts and local unfolding curves. *Biophys J* **73**, 1031-41.
28. Zitzewitz, J. A., Ibarra-Molero, B., Fishel, D. R., Terry, K. L. & Matthews, C. R. (2000). Preformed secondary structure drives the association reaction of GCN4-p1, a model coiled-coil system. *J Mol Biol* **296**, 1105-16.
29. Morfill, J., Blank, K., Zahnd, C., Luginbuhl, B., Kühner, F., Gottschalk, K. E., Plückthun, A. & Gaub, H. E. (2007). Affinity-Matured Recombinant Antibody Fragments Analyzed by Single Molecule Force Spectroscopy. *Biophys J* **93**, 3583-90.

30. Krebber, A., Bornhauser, S., Burmester, J., Honegger, A., Willuda, J., Bosshard, H. R. & Plückthun, A. (1997). Reliable cloning of functional antibody variable domains from hybridomas and spleen cell repertoires employing a reengineered phage display system. *J. Immunol. Methods* **201**, 35-55.
31. Bothmann, H. & Plückthun, A. (1998). Selection for a periplasmic factor improving phage display and functional periplasmic expression. *Nat. Biotechnol.* **16**, 376-80.
32. Hinterdorfer, P., Baumgartner, W., Gruber, H. J., Schilcher, K. & Schindler, H. (1996). Detection and localization of individual antibody-antigen recognition events by atomic force microscopy. *Proc Natl Acad Sci U S A* **93**, 3477-81.
33. Ros, R., Schwesinger, F., Anselmetti, D., Kubon, M., Schafer, R., Plückthun, A. & Tiefenauer, L. (1998). Antigen binding forces of individually addressed single-chain Fv antibody molecules. *Proc Natl Acad Sci U S A* **95**, 7402-5.
34. Kienberger, F., Pastushenko, V. P., Kada, G., Gruber, H. J., Riener, C. K., Schindler, H. & Hinterdorfer, P. (2000). Static and dynamic properties of single poly(ethylene glycol) molecules investigated by force spectroscopy. *Single Mol.* **1**, 123-128.
35. Neuert, G., Albrecht, C., Pamir, E. & Gaub, H. E. (2006). Dynamic force spectroscopy of the digoxigenin-antibody complex. *FEBS Lett.* **580**, 505-9.
36. Morfill, J., Kühner, F., Blank, K., Lugmaier, R. A., Sedlmair, J. & Gaub, H. E. (2007). B-S transition in short oligonucleotides. *Biophys J* **93**, 2400-9.
37. Kühner, F., Morfill, J., Neher, R. A., Blank, K. & Gaub, H. E. (2007). Force-induced DNA slippage. *Biophys J* **92**, 2491-7.
38. Alcantar, N. A., Aydil, E. S. & Israelachvili, J. N. (2000). Polyethylene glycol-coated biocompatible surfaces. *J. Biomed. Mater. Res.* **51**, 343-51.
39. Blank, K., Morfill, J. & Gaub, H. E. (2006). Site-Specific Immobilization of Genetically Engineered Variants of *Candida antarctica* Lipase B. *ChemBioChem* **7**, 1349-1351.

40. Butt, H. J. & Jaschke, M. (1995). Calculation Of Thermal Noise In Atomic-Force Microscopy. *Nanotechnology* **6**, 1-7.
41. Hugel, T. & Seitz, M. (2001). The study of molecular interactions by AFM force spectroscopy. *Macromol. Rapid Commun.* **22**, 989-1016.
42. Friedsam, C., Wehle, A. K., Kühner, F. & Gaub, H. E. (2003). Dynamic single-molecule force spectroscopy: bond rupture analysis with variable spacer length. *J. Phys. Condens. Matter* **15**, S1709-S1723.
43. Oesterhelt, F., Rief, M. & Gaub, H. E. (1999). Single molecule force spectroscopy by AFM indicates helical structure of poly(ethylene-glycol) in water. *New J. Phys.* **1**, 6.1-6.11.
44. Bell, G. I. (1978). Models for the specific adhesion of cells to cells. *Science* **200**, 618-27.
45. van der Spoel, D., van Drunen, R. & Berendsen, H. J. C. (1995). Gromacs: A message-passing parallel molecular dynamics implementation. *Com Phys Comm* **91**, 4356.
46. Hess, B., van der Spoel, D. & Lindahl, E. (2001). A package for molecular simulation and trajectory analysis. *J Mol Mod* **7**, 306-317.
47. van der Spoel, D., Lindahl, E., Hess, B., Groenhof, G., Mark, A. E. & Berendsen, H. J. C. (2005). Gromacs: fast, flexible and free. *J Comp Chem* **26**, 1701-1718.
48. Jorgensen, W. L., Maxwell, D. S. & TiradoRives, J. (1996). Development and testing of the Opls all-atom force field on conformational energetics and properties of organic liquids. *J Am Chem Soc* **118**, 11225-11236.
49. Berendsen, H. J. C., Grigera, J. R. & Straatsma, T. P. (1987). The Missing Term in Effective Pair Potentials. *J Phys Chem* **91**, 6269-6271.
50. Hess, B., Bekker, H., Berendsen, H. J. C. & Fraaije, J. G. E. M. (1997). LINCS: A linear constraint solver for molecular simulations. *J Comp Chem.* **18**, 1463-1472.

**Table 1**

Summary of the obtained values for  $k_{\text{off}}$  and  $\Delta x$  for the three different setups N, M and C (AFM measurements)

setup	Original linear fit		Maximum linear fit		Minimum linear fit	
	$k_{\text{off}}$ in $\text{s}^{-1}$	$\Delta x$ in nm	$k_{\text{off}}$ in $\text{s}^{-1}$	$\Delta x$ in nm	$k_{\text{off}}$ in $\text{s}^{-1}$	$\Delta x$ in nm
N	$(16.9 \pm 1.3) \cdot 10^{-3}$	$(0.82 \pm 0.01)$	$(14.5 \pm 1.0) \cdot 10^{-3}$	$(0.79 \pm 0.01)$	$(14.8 \pm 1.0) \cdot 10^{-3}$	$(0.87 \pm 0.01)$
M	$(7.6 \pm 1.00) \cdot 10^{-3}$	$(0.95 \pm 0.01)$	$(9.2 \pm 1.00) \cdot 10^{-3}$	$(0.89 \pm 0.01)$	$(10.2 \pm 1.2) \cdot 10^{-3}$	$(0.97 \pm 0.01)$
C	$(1.3 \pm 0.2) \cdot 10^{-3}$	$(1.10 \pm 0.01)$	$(1.5 \pm 0.2) \cdot 10^{-3}$	$(1.04 \pm 0.01)$	$(2.0 \pm 0.2) \cdot 10^{-3}$	$(1.11 \pm 0.01)$

**Table 2**

Summary of the obtained information from the force curves from the three different setups N, M and C (SMD simulations)

setup	force peak 1				force peak 2			
	$t_1$ in ps	$F_1$ in pN	$\Delta x_1$ in nm	interaction	$t_2$ in ps	$F_2$ in pN	$\Delta x_2$ in nm	interaction
N	$440 \pm 25$	$567 \pm 25$	$0.88 \pm 0.05$	TYR-L40 and LEU-3 <sub>peptide</sub>	$860 \pm 28$	$716 \pm 23$	$1.72 \pm 0.06$	GLY <sup>H</sup> -H40 and GLU <sup>O<math>\epsilon</math></sup> -6 <sub>peptide</sub>
M	$319 \pm 9$	$1161 \pm 28$	$0.64 \pm 0.02$	GLY <sup>H</sup> -H40 and GLU <sup>O<math>\epsilon</math></sup> -6 <sub>peptide</sub>	$359 \pm 8$	n. d.	$0.72 \pm 0.02$	ASP <sup>O<math>\delta</math>i</sup> -H137 and ARG <sup>H<math>\zeta</math>i</sup> -9 <sub>peptide</sub> (i = 1, 2)
C	$514 \pm 20$	$775 \pm 28$	$1.03 \pm 0.04$	loop opening	$750 \pm 45$	$720 \pm 21$	$1.50 \pm 0.09$	GLY <sup>H</sup> -H40 and GLU <sup>O<math>\epsilon</math></sup> -6 <sub>peptide</sub>

## Figure legends

**Figure 1. Influence of an externally applied force on the energy landscape of a protein or a protein-protein complex.** **a. Two-dimensional cross-section through the energy landscape without an externally applied force (black).** In this picture the protein or the protein-protein complex (blue) is situated in one of the closely related substates at minimal energy. The free energy difference  $\Delta G$  between the folded protein or the bound protein-protein complex (blue) and the unbound or unfolded state is determined by the difference between the energy barrier  $\Delta G_{\text{off}}$  and the activation energy  $\Delta G_{\text{on}}$ . Therefore, the barrier between these two states ( $\Delta G_{\text{off}}$ ), which can be overcome due to thermal fluctuations, determines the rate of interconversion ( $k_{\text{off}}$ ).  $k_{\text{off}}$  represents the basal dissociation rate.  $\Delta x$  reflects the potential width. **b. Two-dimensional cross-section through the energy landscape with an externally applied force (red).** If an external force  $F$  is applied, the energy landscape is tilted (red), thereby reducing the energy barrier by  $-F \cdot x$  (dashed red). This reduction leads to an increase of the dissociation rate.

**Figure 2. Experimental setup.** The antibody fragment H6 possessing a C-terminal cysteine was covalently immobilized onto an amino-functionalized glass slide using a hetero-bifunctional poly(ethylene glycol) spacer. The same coupling chemistry was used for the immobilization of the peptide to the cantilever. N, M and C show different measurement setups. In setup N a cysteine and three glycines were attached to the N-terminus of the peptide. In setup M alanine on position 8 of the peptide sequence was changed to a cysteine and finally in setup C three glycines followed by a cysteine were attached to the C-terminus of the peptide.

**Figure 3. Results from the AFM measurements. a. Example of three typical force-extension curves measured for setup N, M and C.** The force-extension curves show the rupture event of the scFv-peptide complex, experimentally recorded at a retract velocity of 800 nm/s. The red force-extension curve corresponds to a rupture event measured for setup N. The green and blue force-extension curves were gained for setup M and C. All force-extension curves are virtually indistinguishable and possess very similar rupture forces. The elastic behavior of the spacer PEG can be described with the two-state FJC-fit (black curve).

**b. Example of a rupture force distribution, obtained for setup N.** The rupture force histogram contains ~300 rupture events and was fitted with a Gaussian curve (black).

**c. Example of a loading rate distribution, obtained for setup N.** The histogram of the loading rates was plotted logarithmically and fitted with a Gaussian curve (black).

**Figure 4. Diagram showing the most probable rupture force plotted against the corresponding loading rate (pictured logarithmically) for all three setups N, M and C.** The data points were gained from the Gaussian fits of the rupture force histogram and the histogram of loading rates. The red data points (setup N) were fitted to a straight line. From this linear fit  $\Delta x = (0.82 \pm 0.01)$  nm and  $k_{\text{off}} = (16.9 \pm 1.3) \cdot 10^{-3} \text{ s}^{-1}$  were obtained. The green data set was measured for setup M. From the linear fit  $\Delta x = (0.95 \pm 0.01)$  nm and  $k_{\text{off}} = (7.6 \pm 1.0) \cdot 10^{-3} \text{ s}^{-1}$  were obtained. Finally, the measurement of setup C yielded the blue data set. Here, the linear fit lead to  $\Delta x = (1.10 \pm 0.01)$  nm and  $k_{\text{off}} = (1.3 \pm 0.2) \cdot 10^{-3} \text{ s}^{-1}$ .

**Figure 5. Scheme of a possible energy landscape with two barriers for setup N.** For the SPR measurements (setup N and C), the second higher energy barrier is rate limiting since this barrier has to be overcome to generate free scFv fragment and peptide. If an external force is applied for example with an AFM, the energy landscape is tilted (red curve). Now the first originally lower barrier becomes prominent and rate limiting for the unbinding process.

This model of an energy landscape is able to explain the low dissociation rate for setup N obtained with SPR, compared with the higher dissociation rate obtained with the AFM.

**Figure 6. Steered Molecular Dynamics Simulations setup.** All molecular dynamics simulations were started using the same initial structure. The Center Of Mass (COM) of the heavy chain  $V_H$  was fixed in space during the whole simulation time, whereas the light chain  $V_L$  was not constricted. **a.** For the simulation of the unbinding forces the pulling potential was attached to different  $C_\alpha$ -atoms of the peptide to yield the setups N, M and C. **6b-6d. Last contacts between the scFv fragment and the peptide revealed by the SMD simulations.** The last contacts between the peptide and the antibody are shown for the respective setups. The amino acids are identified in the main text.

**Figure 7. Unbinding process of setup N. a. Force-time curves.** The mean average force-time curve (black) and a representative force-time graph (red) were plotted. The unbinding process shows two important events, which correspond to the highlighted force peaks. The colors of the highlighted force peaks were chosen according to the colors in the molecular structures (cyan for the first rupture event and purple for the second rupture event). **b. Structural origin of the first unbinding event.** The first unbinding event (cyan) corresponds to the rupture of the hydrophobic contact between TYR-L40 and LEU-3<sub>peptide</sub>. The picture shows the molecular structure shortly before the event is observed. **c. Structural origin of the second unbinding event.** The second unbinding event (purple) corresponds to the rupture of the important H-bond between GLY<sup>H</sup>-H40 and GLU<sup>O $\epsilon$</sup> -6<sub>peptide</sub>. The picture shows the molecular structure shortly before the event is observed. This second rupture event has also been found in the two other setups M and C.

**Figure 8. Unbinding process of setup M. a. Force-time curves.** The mean average force curve (black) and a representative force-time graph (green) were plotted. The force-time curve shows one major peak highlighted in purple. **b. Structural origin of the observed unbinding event.** The unbinding event (purple) corresponds to the rupture of the important H-bond between GLY<sup>H</sup>-H40 and GLU<sup>O $\epsilon$</sup> -6<sub>peptide</sub>. The picture shows the molecular structure shortly before the event is observed. This rupture event has also been found in the two other setups N and C.

**Figure 9. Unbinding process of setup C a. Force-time curves.** The mean average force-time curve (black) and a representative force-time graph (blue) were plotted. The two important rupture events represented by the force peaks of the mean curve were highlighted according to the colors in the molecular structures. **b. Structural origin of the first unbinding event.** The first rupture event (orange) corresponds to the breakage of a backbone hydrogen bond stabilizing the  $\alpha$ -helical structure of the peptide resulting in the opening of a peptide loop. The picture shows the molecular structure shortly before this event is observed. **c. Structural origin of the second unbinding event.** The second unbinding event (purple) corresponds to the rupture of the important H-bond between GLY<sup>H</sup>-H40 and GLU<sup>O $\epsilon$</sup> -6<sub>peptide</sub>. The picture shows the molecular structure shortly before the event is observed. This rupture event has also been found in the two other setups N and M.

**Figure 10. Energy barriers obtained from the AFM experiments and rupture lengths obtained from the SMD Simulations.** The potential widths and basal dissociation rates have been taken from the AFM measurements and plotted into a diagram (setup N – red, setup M – green and setup C – blue) to provide an overview of the barriers that need to be crossed. As the further unbinding pathways on the respective energy landscapes are not known, these were not included in the diagram. The arrows above the energy landscapes indicate the

positions of the respective rupture lengths for the first and second barrier crossing of the main unbinding pathway, obtained from the SMD simulations.

Figure 1

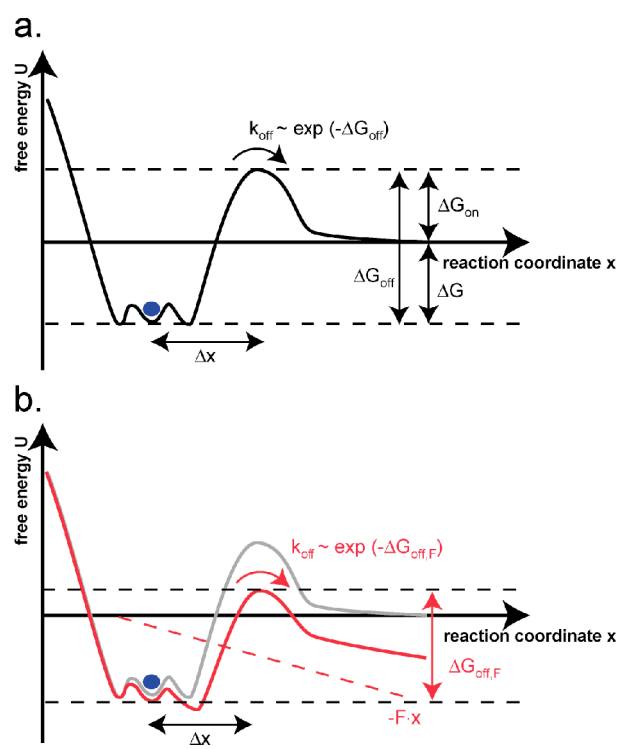


# Figure 2

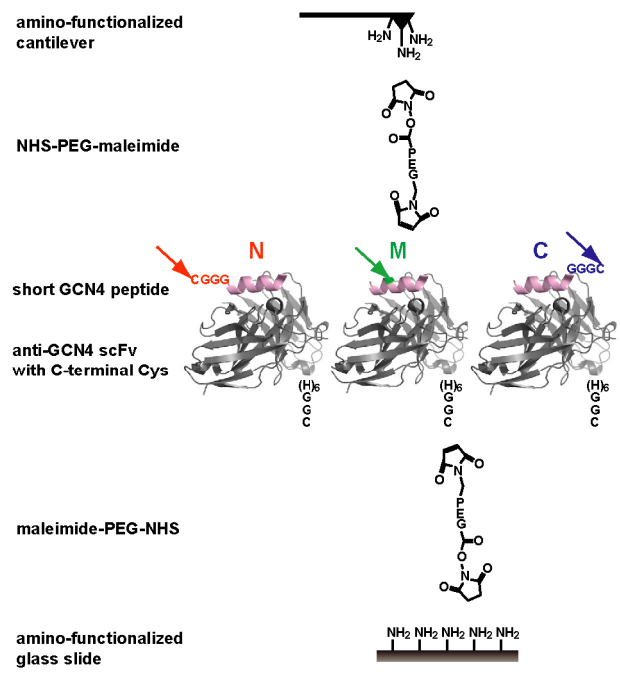
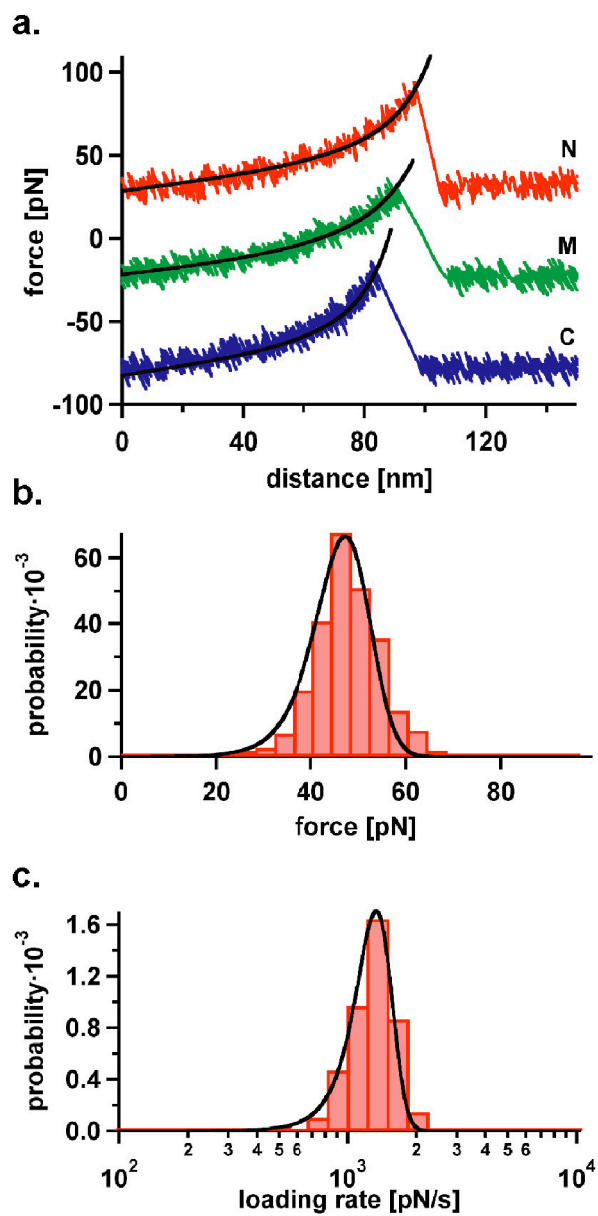


Figure 3



**Figure 4**

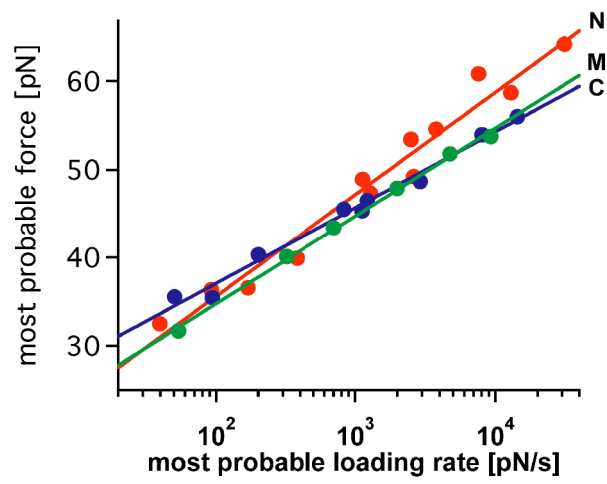
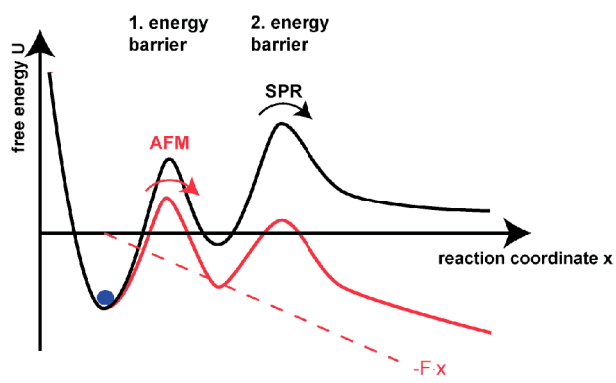


Figure 5



**Figure 6**

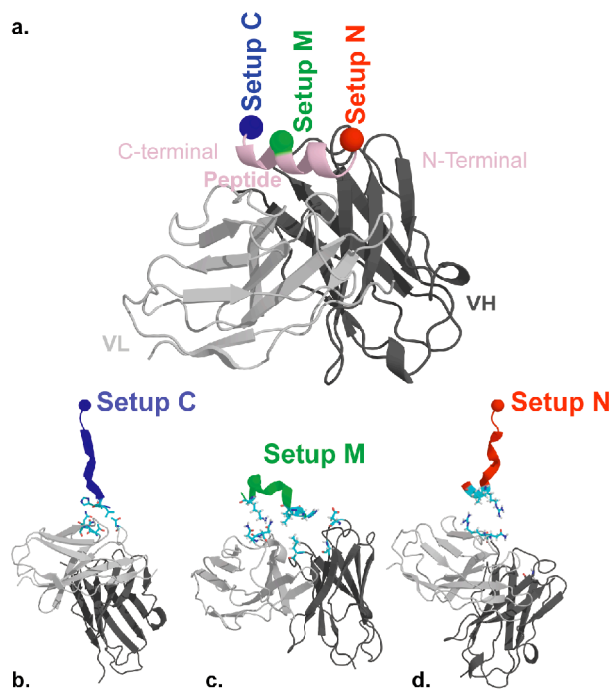
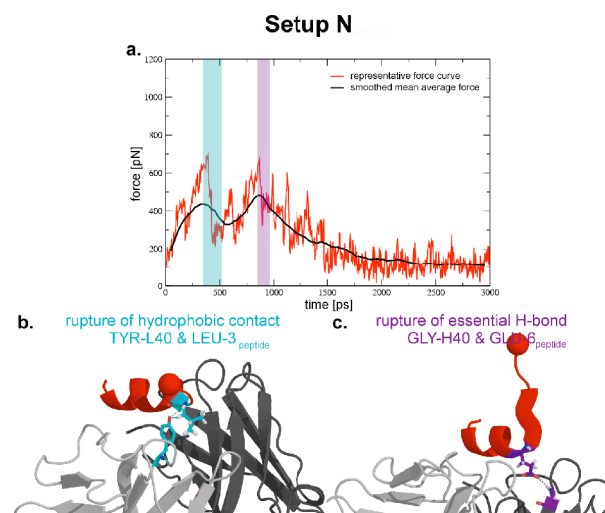


Figure 7



**Figure 8**

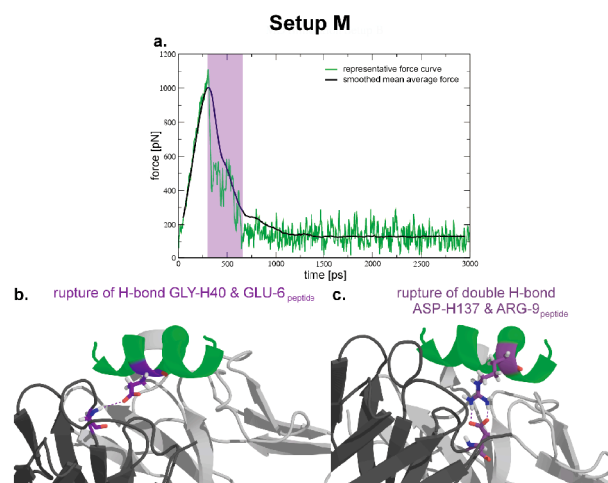


Figure 9

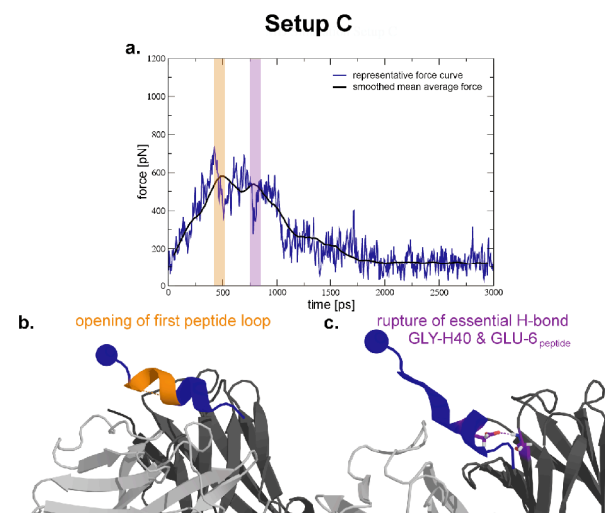
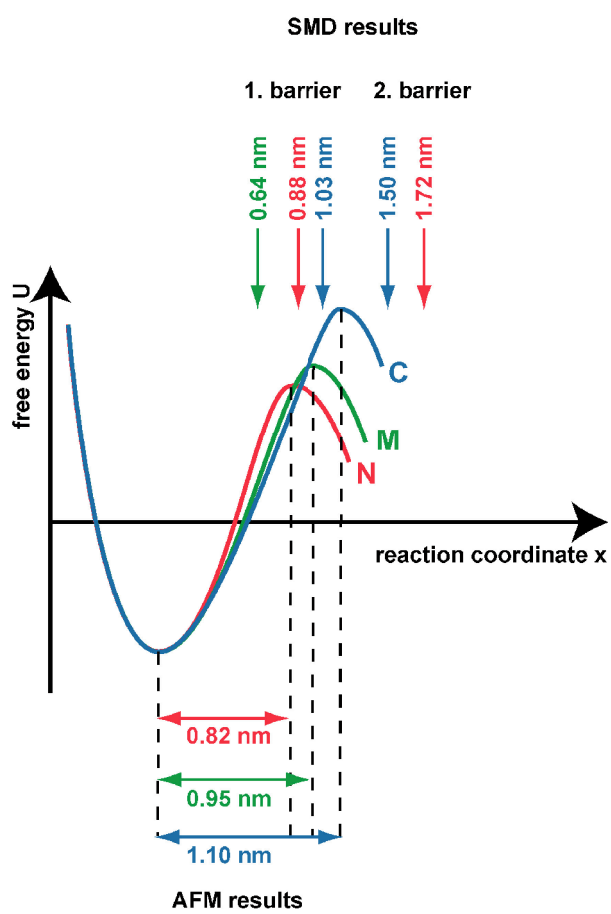


Figure 10



## **P2**

### **8.2 Site-specific and covalent immobilization of biomolecules for single molecule experiments**

J. Morfill, T. Nicolaus, G. Neuert, H. E. Gaub and K. Blank

Submitted to Nature Methods

# **Site-specific and covalent immobilization of biomolecules for single molecule experiments**

Julia Morfill<sup>1</sup>, Thomas Nicolaus<sup>1</sup>, Gregor Neuert<sup>1,2</sup>, Hermann E. Gaub<sup>1</sup> & Kerstin Blank<sup>1,3</sup>

<sup>1</sup> Lehrstuhl für Angewandte Physik & Center for Nanoscience, LMU München,  
Amalienstrasse 54, D-80799 München, Germany

<sup>2</sup> Department of Physics, Massachusetts Institute of Technology,  
77 Massachusetts Avenue, Cambridge, MA 02139, USA

<sup>3</sup> Department of Chemistry, Katholieke Universiteit Leuven  
Celestijnenlaan 200 F, B-3001 Heverlee, Belgium

Corresponding author: Dr. Kerstin Blank  
kerstin.blank@chem.kuleuven.be  
Tel.: +32 (0) 16 32 74 47  
Fax: + 32 (0) 16 32 79 90

## Summary

Site-specific and covalent coupling is desired for almost every application relying on immobilized biomolecules. Microarrays, surface plasmon resonance applications, single molecule fluorescence or force spectroscopy measurements are just a few examples. For all these experiments surfaces with low non-specific binding but a high number of reactive sites are of advantage to allow a high dynamic range to adjust the density of the biomolecules on the surface for each specific application. As a result, such a surface provides good signal to noise ratios and a high probability to find a single molecule on the surface. The usage of hetero-bifunctional poly(ethylene glycol) (PEG) spacers combines many advantages: PEG is biocompatible and surfaces with a sufficiently high density of PEG become “resistant” to the adsorption of biomolecules<sup>1-3</sup>. PEG is a polymer with a relatively defined length and it can be activated to provide reactive groups for coupling<sup>4</sup>. Here we describe a protocol, which uses PEG carrying a N-hydroxy succinimide (NHS) group on one end and a maleimide group on the other end (Fig. 1). After coupling the PEG via its NHS group to an amino-functionalized surface (Box 1), the relatively stable but highly reactive maleimide group allows the coupling of biomolecules, which carry a free thiol group. Thiol groups can be incorporated into oligonucleotides and peptides during solid phase synthesis. For proteins the usage of thiols relies on the presence of a free cysteine on the molecule, which can either be present naturally or can be introduced by site-directed mutagenesis at a desired position (Box 2). We have been able to show that this protocol can be applied for a broad range of amino-functionalized surfaces (glass<sup>5-9</sup>, Si<sub>3</sub>N<sub>4</sub> cantilevers<sup>6-9</sup> and even PDMS) and many different types of biomolecules (oligonucleotides<sup>6,7,9</sup>, peptides<sup>8</sup>, recombinant antibody fragments<sup>8</sup> and enzymes<sup>5</sup>). The only adjustment required when changing the biological system is the concentration of the used biomolecules.

## Materials

### *Reagents*

Cantilevers (Bio-lever, Olympus; Park-lever, Veeco Microscopes)

Cover slips (Menzel Gläser)

Amino-functionalized slides type A and A+ (Schott Nexterion)

3-Aminopropyl dimethyl ethoxysilane (ABCR GmbH)

NHS-PEG-maleimide (MW according to the desired application; Rapp Polymere)

Tris(2-carboxyethyl) phosphine (TCEP; Perbio Science)

TCEP-Beads (Perbio Science)

Ethanol abs (Roth)

Isopropanol (Roth)

Toluol (Roth)

DNA- or RNA-oligonucleotides with thiol group (IBA)

Peptide with cysteine at the desired position (Jerini Peptide Technologies GmbH)

Recombinant protein with a single cysteine

Bovine serum albumin fraction V, protease free (BSA; Roth)

Borate buffer, BB (50 mM sodium borate pH 8.5)

Coupling buffer, CB (50 mM sodium phosphate pH 7.2 @ 4 °C, 50 mM NaCl, 10 mM EDTA)

Sodium acetate solution, NaAc (3M, pH 6.0)

10x Phosphate buffered saline PBS (Roche)

Ethanol, 85 %

## *Equipment*

UV-ozone cleaner (FHR)

Refrigerated centrifuge for Eppendorf tubes (Heraeus)

Thermomixer (Eppendorf)

Microarray scanner (Tecan)

Orbitrary shaker (IKA)

Ultrasonic bath (Sonorex)

Vortex (Scientific Industries)

Cold room

Filter paper (Macherey-Nagel)

Teflon holder for cover slips

Several glass Petri dishes (Roth)

Disposable plastic Petri dishes (Roth)

Quadriperm petridishes for slides (VWR)

## Initial Remarks

The described procedure uses commercially available glass slides (for the preparation of amino-functionalized surfaces see Box 1) and has mainly been used in force spectroscopy measurements. Therefore, the preparation of slides and cantilevers is carried out in parallel. However, the same protocol has been used for single molecule fluorescence measurements. In this case, one only needs to follow the procedure for slides or cover slips.

Silanes and poly(ethylene glycols) are moisture and/or oxidation sensitive. It is recommended to aliquot them upon arrival and to store them under argon at the temperature stated by the manufacturer. Storage under argon is also required for the amino-functionalized glass slides.

It is recommended to use gloves in all steps and to use exclusively tweezers to touch cantilevers and glass surfaces. The tweezers should be cleaned with ethanol and water before using them. In several steps of the protocol glass Petri dishes, slides and cover slips are used. These are cleaned with ethanol and then ultra pure water for 10 minutes each in an ultrasonic bath. Finally they are dried in a clean oven at 80°C.

## Procedure

Cleaning & activating the cantilevers

1| Deposit the cantilevers with the tips facing up on a cleaned glass slide in a UV-Ozone cleaner for 10 minutes.

### CRITICAL STEP

amino functionalization of cantilevers

2| For silanization, keep the cantilevers in concentrated 3-Aminopropyl dimethyl ethoxysilane in a small cleaned glass Petri dish for 60 seconds at room temperature.

3| Wash the cantilevers in 100 ml toluol for 1-2 minutes. The toluol, which remains on the cantilevers, is removed, by drying the cantilever on a filter paper. Now, wash the cantilevers in 100 ml ultra pure water for 1-2 minutes. Again, the remaining liquid film on the cantilever surface has to be removed with a filter paper. Deposit the cantilevers with the tips facing up in a cleaned small glass Petri dish.

4| Put the glass Petri dish, containing the cantilevers, in a oven heated to 80°C for 30 minutes. After this silanization procedure, the cantilevers have to cool down to room temperature for 1-2 minutes.

### CRITICAL STEP

Cantilevers – deprotonation of amino groups

5| For each cantilever pipet one droplet of 50 µl BB into a clean container, e.g. a disposable plastic Petris dish. Put the cantilevers in the droplets of BB and place the container, containing the cantilevers in a box with a water-saturated atmosphere to prevent evaporation. Incubate for 1 hour at room temperature.

### CRITICAL STEP

Glass surface – deprotonation of amino groups

6| Pipet 5 ml BB each into the required number of wells in a Quadriperm petridish (one slide fits in there exactly). Put one amino functionalized slide in each well and shake for 1 hour.

**CRITICAL STEP**

Reduction of disulfides

Alternative a – DNA or RNA with thiol modification – starting the reaction

7a| Dilute the TCEP stock solution (500 mM) to a concentration of 10 mM in ultra pure water. For one slide or two cantilevers, 18  $\mu$ l of the respective DNA (100 $\mu$ M) or RNA is necessary to perform force spectroscopy measurements. Mix 18  $\mu$ l of the respective DNA or RNA with 18  $\mu$ l of 10 mM TCEP in an Eppendorf tube and store at 4°C for 30 minutes.

**CRITICAL STEP**

Alternative b – proteins or peptides with a free cysteine – starting the reaction

7b| For the generation of proteins with a free cysteine see Box 2. The starting concentration of the protein should be between 0.2 mg/ml and 1.0 mg/ml. For peptides a concentration of 2 mM is recommended. Always keep the molecules on ice. Mix TCEP beads well. Take 10  $\mu$ l of beads (corresponds to 20  $\mu$ l suspension as supplied by the manufacturer) and add them to 1 ml of cooled CB in an Eppendorf tube. Vortex and centrifuge for 2 min at 5000 rpm and 4 °C. Remove the supernatant and wash the beads for 2 more times with 1 ml of CB. After the final washing step remove the supernatant carefully. Add 10  $\mu$ l protein or peptide solution and shake the mixture in a Thermomixer (set to 4°C) at maximum speed for at least 1 hour.

**CRITICAL STEP**

Cantilevers - coupling of the PEG spacer

8| Make sure that the powder of the NHS-PEG-maleimide is warmed up to room temperature before weighing the required amount (see step 9). Dissolve the NHS-PEG-maleimide in a

concentration of 50 mM in BB. Centrifuge 1 min at maximum speed. Use the solution immediately.

#### **CRITICAL STEP**

9| For each cantilever pipet droplets of at least 25  $\mu\text{l}$  of the PEG solution in a clean container, e.g. a disposable plastic Petri dish. Remove the cantilevers from the BB droplets (see step 5) and put them directly into the PEG solution droplets. Place the container, containing the cantilevers, in a box with a water-saturated atmosphere to prevent evaporation. Incubate for 1 hour at room temperature.

10| Remove the cantilevers from the PEG solution droplets and wash them in 100 ml ultra pure water. Store the cantilevers in a clean container, containing ultra pure water.

Glass surface - coupling of the PEG spacer

11| Take the slide out of the BB and dry it under a stream of nitrogen. Put it into an appropriate container, e.g. a disposable plastic Petri dish.

12| Make sure that the powder of the NHS-PEG-maleimide is warmed up to room temperature before weighing the required amount (see step 13). Dissolve the NHS-PEG-maleimide in a concentration of 50 mM in BB. Centrifuge 1 min at maximum speed. Use the solution immediately.

#### **CRITICAL STEP**

13| Pipet the PEG solution on the amino functionalized glass slide and cover it with a cleaned cover slip. One can either incubate PEG on the whole slide or just choose a small area depending on the size of the cover slip. For one  $\text{cm}^2$  approximately 15  $\mu\text{l}$  of the PEG solution is required. Place the container with the slide in a box with a water-saturated atmosphere to prevent evaporation. Incubate for 1 hour at room temperature.

14| Take out the slide and wash it carefully under flowing ultra pure water. The cover slip will be removed by the flowing water. Dry the slide under a stream of nitrogen and put it in a clean container.

#### Reduction of disulfides

Alternative a – DNA or RNA with thiol modification – removal of reducing agent

15a| (continued from step 7a) To remove the TCEP from the solution add 4  $\mu$ l NaAc and vortex for 60 seconds. Then add 160  $\mu$ l ethanol abs, mix carefully using a pipette and store the solution at -20°C for 30 minutes. Take the sample(s) out of the freezer and centrifuge for 10 minutes at 13000 rpm at 4°C. Remove the supernatant. Be careful not to disturb the pellet. Wash the pellet with 800  $\mu$ l 85 % ethanol. Centrifuge the solution for 10 minutes at 13000 rpm at 4°C. Remove the supernatant carefully. Air-dry the pellet at room temperature until the ethanol has evaporated. Dissolve the pellet in the desired amount of CB and use as quickly as possible.

#### **CRITICAL STEP**

**PAUSE POINT** The ethanol precipitation can be done at any time and the air-dried pellets can be stored at -20°C until use.

Alternative b – proteins or peptides with cysteine – removal of reducing agent

15b| (continued from step 7b) Take the sample(s) out of the thermomixer and centrifuge at maximum speed for 2 min at 4 °C. Remove the supernatant containing the reduced proteins or peptides without sucking any beads into the pipette. Dilute the reduced proteins and peptides to the desired concentration by using CB. Use as quickly as possible. In the meantime keep the samples on ice.

*The procedure for proteins and peptides is slightly different. In the case of DNA or RNA the removal of the reducing agent can be achieved by precipitating the oligonucleotides.*

*However, this is not possible for proteins and peptides. When using an immobilized reducing agent it can be easily removed by centrifugation (see step 15b).*

Cantilevers – coupling of reduced biomolecules

16| For each cantilever, pipet droplets of at least 25  $\mu$ l of the desired protein, peptide or oligonucleotide solution in a clean container. Remove the cantilevers from the ultra pure water (see step 10) and put them directly into the prepared protein, peptide or DNA solution droplets.

17| Incubate for at least 1 hour at 4 °C in a water-saturated atmosphere.

**PAUSE POINT** This reaction can also be performed over night.

Glass surface – coupling of reduced biomolecules

18| Pipet the desired amount of reduced sample on the slide at the desired position(s). Spots with a volume starting from 1  $\mu$ l can be prepared this way depending on the application. For AFM or single molecule fluorescence measurements use at least 20  $\mu$ l per spot. For initial tests to check the performance of the protocol 1  $\mu$ l to 2  $\mu$ l of every sample is sufficient.

*In the case of sensitive proteins it is recommended to perform this step in a cold room. This also prevents the evaporation of the spotted sample(s) while preparing other surfaces in parallel.*

19| Incubate for at least 1 hour at 4 °C in a water-saturated atmosphere.

**PAUSE POINT** This reaction can also be performed over night.

Cantilevers – removal of non-coupled biomolecules

20| Wash the cantilevers in 100 ml PBS (or any other buffer used for the final experiment) for 1-2 minutes and repeat this procedure one more time with fresh PBS. Store the cantilevers in PBS in a clean container at room temperature until use.

## CRITICAL STEP

Glass surface – removal of non-coupled biomolecules

21| Pipet 5 ml of PBS (or any other buffer used for the final experiment) into the required amount of wells of a Quadriperm Petri dish. Remove the liquid from the surface by suction e.g. with a pipette or with a pipette tip attached to a pump. Be careful to remove the solution as completely as possible without touching the surface. Place the slide in the buffer immediately. Put on a shaker at 25 rpm for 5 min. Depending on the experiment, either store the slide in fresh buffer until use or dry the slide under a stream of nitrogen.

## CRITICAL STEP

single molecule experiment

22| Proceed with the planned experiments.

*In principle it should be possible to store cantilevers and surfaces either dry, under argon or in an appropriate buffer. However, this has never been checked in detail since storage might not only lead to inactivation or degradation of the biomolecules but also to the accumulation of dirt from the environment on the surfaces.*

## TROUBLE SHOOTING

OPTIONAL: Fluorescence detection

23| Prepare a PBS solution containing 0.4 % BSA. Dilute the fluorescently labeled detection molecule(s) (Box 3) to the appropriate concentration in 5 ml of the prepared buffer. For labeled oligonucleotides a concentration of 0.1  $\mu\text{M}$  is recommended. For proteins (e.g. antibodies) the final concentration can vary between 0.1  $\mu\text{g/ml}$  and 10  $\mu\text{g/ml}$  depending on the affinity of the respective interaction. Pipet the mixture into a Quadriperm Petri dish and shake the slide or cover slip for 1 hour at 25 rpm in dark surroundings to prevent bleaching of the fluorescent dye.

24| Wash the slide or cover slip at least 2 x in 5 ml PBS + BSA in the Quadriperm Petri dish in dark surroundings. Take the slide out and dry it under a stream of nitrogen.

*The dried buffer on the surface does not interfere with the fluorescence measurements. Never wash the slide or cover slip with water since this might disrupt the biological interaction.*

25| Scan the fluorescence on the surface by using a microarray scanner or a confocal microscope.

## **TROUBLE SHOOTING**

## Troubleshooting table

<b>Problem</b>	<b>Solution</b>
<b>Step 22</b> no interaction detectable with the AFM	Check the functionality of all different components with appropriate positive and negative controls (e.g. molecules with and without the reactive groups) as described in step 23 and Box 3.
<b>Step 22</b> no specific fluorescence signal when performing single molecule fluorescence measurements	<p>Check the functionality of all the different components with appropriate positive and negative controls (e.g. molecules with and without the reactive groups) as described in step 23 and Box 3.</p> <p>If the background fluorescence is too high check the different reagents step by step with the measurement set-up in order to identify the origin of the fluorescent impurity.</p>
<b>Step 23</b> high background fluorescence	<p>The most likely reasons are:</p> <ol style="list-style-type: none"><li>1. One of the used reagents contains fluorescent impurities. This can be analyzed by scanning the surface after every step.</li><li>2. The coupling of the PEG did not work and the fluorescently labeled detection molecule adsorbs non-specifically to the surface. This is very likely if no specific spots appear on the expected positions. Check the reactivity of the PEG with other methods.</li><li>3. The coupling of the biomolecules did not work. We</li></ol>

---

have observed that the detection molecules adsorb non-specifically if no specific interaction can take place. Check the reactivity of the biomolecule with other methods. If the biomolecule is relatively old or has not been stored properly and the reaction has worked before consider replacing it.

4. The concentration of the fluorescently labeled detection molecule is too high. Perform a dilution series to find out the optimal concentration.

5. No specific interaction with the labeled detection molecule. Check the interaction between the molecules with other methods. If the detection molecule is relatively old or has not been stored properly and the reaction has worked before consider replacing it.

6. The number or time of the washing steps before scanning the surface was not sufficient. Extend the washing procedure.

7. Depending on the detection molecule used, it might become necessary to block the remaining maleimide groups on the surface (e.g. with cysteine).

**In order to find out where the problem is exactly it is very helpful to include negative and positive controls in the experiment (see box 3).**

---

**Step 23** little or no fluorescent signal at the positions where the

The most likely reasons are:

1. The coupling of the PEG did not work. This is very

---

---

biomolecules have been  
immobilized

likely if the fluorescent background is very high in addition. Check the reactivity of the PEG with other methods.

2. The coupling of the biomolecules did not work. Check the reactivity of the biomolecule with other methods. If the biomolecule is relatively old or has not been stored properly and the reaction has worked before consider replacing it.

3. The concentration of the immobilized biomolecule was too low. The concentrations of the biomolecules described in the text are those that worked best in our experiments. Do a dilution series of the biomolecule and spot these different dilutions on the surface.

4. The concentration of the fluorescently labeled detection molecule is too low. Perform a dilution series to find out the optimal concentration.

5. No specific interaction with the labeled detection molecule. Check the interaction between the biomolecules with other methods. If the detection molecule is relatively old or has not been stored properly and the reaction has worked before consider replacing it.

**In order to find out where the problem is exactly it is very helpful to include negative and positive controls in the experiment (see box 3).**

---

## Critical steps

**Step 1** The generated ozone does not only oxidize all organic dirt on the surface, which might interfere with the coupling reaction, it also oxidizes the surface of the cantilevers to provide a higher density of Si-OH groups for coupling.

**Step 4** Without baking the cantilevers, the silane layer is not stable in aqueous solutions. This step is essential for the formation of the covalent bond between the surface and the silane.

**Steps 5 and 6** The reaction between the amino groups on the surface and the NHS groups of the PEG requires deprotonated amino groups. The slightly alkaline pH of the borate buffer ensures that most amino groups are deprotonated. In principle any other buffer with a similar pH can be used as well. However, buffers containing free amino groups (such as Tris) have to be avoided since they will block the reaction of the PEG with the surface.

**Step 7** Thiols can oxidize easily and form disulfides. But only thiols in their reduced state are able to react with maleimide groups. This step ensures that the thiol groups are in their reduced state.

**Step 7 and 15** The composition of the buffer CB is critical for the performance of the protocol. The pH value ensures that the reaction of maleimides is specific for thiol groups. For higher pH values the probability increases that the reaction of maleimides also occurs with amino groups, which are present on the surface of proteins. Furthermore, the EDTA in the buffer slows down the rate of reoxidation of the generated free thiols.

**Step 8 and 12** The reactive groups on the PEG (especially the NHS ester) are sensitive to hydrolysis. If the vial containing the PEG is not warmed up to room temperature before

opening humidity from the air condenses on the PEG leading to hydrolysis of the reactive groups. For this reason it is also important to store the PEG under argon.

Once dissolved in an aqueous solution, the reaction of the NHS ester with amino groups competes with the autohydrolysis. Both, the desired reaction and the autohydrolysis proceed faster for higher pH values. Therefore the used pH is a compromise to balance stability and reactivity. Nevertheless, one has to make sure that the PEG solution is brought onto the surface and the cantilevers as quickly as possible.

**Step 15a** It is essential to remove the reducing agent from the sample since it interferes with the coupling reaction between the thiol groups and the maleimide groups.

**Step 20 and 21** This washing step is crucial for the following experiments. If non-coupled biomolecules remain on the surface they might interfere with the experiment thereby reducing the amount of available binding sites.

## Comments

The described method has been used for single molecule force and fluorescence measurements. The single molecule force measurements have been performed to analyze the interactions between DNA oligonucleotides<sup>6,7,9</sup> as well as the interaction between a peptide and different recombinant antibody fragments<sup>8</sup>. All experiments showed very low non-specific binding and very high interaction frequencies (up to 50%). As a result very good statistics have been obtained allowing the discrimination of only small differences in the binding strength of different interactions<sup>8</sup>. For one example the whole range of loading rates, which is accessible with the atomic force microscope, could be measured on one day with one cantilever only<sup>7</sup>. Furthermore, these high interaction frequencies allowed the use of the atomic force microscope to repeatedly pick up fluorescently labeled DNA oligonucleotides specifically at one position and to deposit them at an other position on the surface. In this way 2D structures with nanometer resolution could be assembled<sup>9</sup>.

These high interaction frequencies and the low non-specific binding are the result of a dense layer of PEG which is achieved by using high concentrations of silane and PEG in the first steps. The adjustment of the density of the biomolecules for the respective experiment is done in the last step when coupling the biomolecules. Therefore, another key advantage of this method is its general applicability for many different biomolecules. Only one protocol is required and only little optimization needs to be done when changing the biological system.

Many other methods are available to reduce the disulfides of the biomolecules. However, for many of them the removal of the reducing agent is more complicated especially in the case of proteins where no ethanol precipitation can be performed. The use of TCEP beads simplifies this procedure immensely. In addition, the use of TCEP beads has the additional advantage that only the surface of the protein is accessible for the reducing agent. In none of our examples we had problems with the reduction of internal disulfide bonds. It should be noted that the usage of beads did not work as well for oligonucleotides and depends on the method used by the manufacturer to introduce the thiol group into the oligonucleotide.

Parts of this protocol have also been used to immobilize enzymes on glass surfaces<sup>5</sup> or to couple antibody fragments and peptides to thiol reactive beads. The method may find further use in other applications such as protein and DNA microarrays as well as surface plasmon resonance techniques.

## References

1. Jeon, S.I., Lee, J.H., Andrade, J.D. & Degennes, P.G. Protein Surface Interactions in the Presence of Polyethylene Oxide. 1. Simplified Theory. *J. Colloid Interface Sci.* **142**, 149-158 (1991).
2. Sofia, S.J. & Merrill, E.W. Protein Adsorption on Poly(ethylene oxide)-Grafted Silicon Surfaces. In *Poly(ethylene glycol) Chemistry and Biological Applications*. (Harris, J.M. & Zalipsky, S., ed) 342-360 (ACS Symposium Series, Washington, DC, 1997).
3. Alcantar, N.A., Aydil, E.S. & Israelachvili, J.N. Polyethylene glycol-coated biocompatible surfaces. *J. Biomed. Mater. Res.* **51**, 343-351 (2000).
4. Veronese, F.M. Peptide and protein PEGylation: a review of problems and solutions. *Biomaterials* **22**, 405-417 (2001).
5. Blank, K., Morfill, J. & Gaub, H.E. Site-specific immobilization of genetically engineered variants of *Candida antarctica* lipase B. *ChemBiochem* **7**, 1349-1351 (2006).
6. Kühner, F., Morfill, J., Neher, R.A., Blank, K. & Gaub, H.E. Force-induced DNA slippage. *Biophys. J.* **92**, 2491-2497 (2007).
7. Morfill, J. et al. B-S transition in short oligonucleotides. *Biophys. J.* **93**, 2400-2409 (2007).
8. Morfill, J. et al. Affinity-matured recombinant antibody fragments analyzed by single-molecule force spectroscopy. *Biophys. J.* **93**, 3583-3590 (2007).
9. Kufer, S.K., Puchner, E., Gump, H., Liedl, T. & Gaub, H.E. Single-Molecule Cut-and-Paste Surface Assembly. *Science in press*.
10. Velonia, K., Rowan, A.E. & Nolte, R.J.M. Lipase polystyrene giant amphiphiles. *J. Am. Chem. Soc.* **124**, 4224-4225 (2002).

## **Box 1 – Preparation of amino functionalized glass surfaces**

Whereas for many applications it is possible to use commercially available amino-functionalized surfaces some applications require the use of cover slips or similar.

In this case, it is necessary to silanize the required glass surface using a similar protocol as for the cantilevers:

**Step 1** Place the cover slips in an appropriate Teflon holder. Put the holder with the cover slips in a beaker containing 50 % isopropanol. Sonicate for 10 min.

**Step 2** Wash the cover slips with ultra pure water and dry them under a stream of nitrogen.

**Step 3** Deposit the cover slips in a UV-Ozone cleaner for 10 minutes.

**Step 4** Silanize the cover slips with pure 3-Aminopropyl dimethyl ethoxysilane for 30 min. Depending on the amount of cover slips to be silanized one has to find a solution to use as little volume as possible because the silane is relatively expensive. Always use Teflon or glass for silanization reactions.

**Step 5** Put the cover slips in isopropanol immediately and wash them carefully with isopropanol. Wash with ultra pure water and dry under a stream of nitrogen.

**Step 6** Incubate the cover slips at 80 °C for 1 hour.

**Step 7** Proceed with the protocol for amino-functionalized slides (step 6).

## **Box 2 – Preparation of proteins containing cysteines for coupling**

Coupling proteins via thiol groups is superior compared to the commonly used coupling procedures based on the amino groups of lysines. First, the thiol group itself is more reactive than the amino group. Second, maleimide groups for thiol coupling are more stable than NHS groups. This combination results in a higher coupling efficiency. And last but not least, cysteines are less frequent than lysines. Therefore, only a few cysteines are present on the surface of a protein. In fact, many proteins do not contain any exposed cysteine residues at all. In order to choose the best strategy one should check for the amount and the positions of the cysteines on the protein. In general it can be assumed that buried disulfide bonds are not accessible for the reducing agent if the protein is folded correctly. (In some very unlucky cases the protein might have multiple cysteines on the surface. In addition some enzymes need a free cysteine in their active site. In this case one has to evaluate on a case-by-case basis if the strategy can still be used for the desired application.)

**Reducing surface exposed disulfide bonds (potentially site-specific).** The protein of interest might have accessible disulfide bonds on the surface. These disulfide bonds can be reduced<sup>10</sup> with the protocol described in steps 7b and 15b. If there is only one disulfide bond the position of coupling is relatively well defined. However, one should keep in mind that this method generates two reactive thiols for coupling. They are located at the same site of the protein but depending on the desired application it might make a difference if one or the other is coupled. In addition, since the reduced thiols are in close proximity there is a high chance of reoxidation before coupling to the surface can take place.

**Mutating surface exposed cysteines forming a disulfide bond (site-specific).** If the protein of interest has one or more accessible disulfide bonds on the surface it might be a better strategy to mutate one cysteine of the disulfide bond to alanine<sup>5</sup>. With this strategy the disulfide bond cannot form anymore and the remaining cysteine can be used for coupling.

**Attaching a free cysteine at the C-terminus at the genetic level (site-specific).** Most likely the best and most general strategy is to attach an additional cysteine at the C-terminus

of the protein<sup>5,8</sup>. This strategy is even more attractive since a tag for purification (e.g. His tag) can be added to the protein together with the cysteine. In our experience proteins with a cysteine after the His tag yielded the highest efficiency for coupling due to the good accessibility of the cysteine.

**Converting amino groups into thiol groups (NOT site-specific).** If none of the above strategies can be applied but one still wants to use the thiol-maleimide reaction it is possible to convert amino groups on the surface of the protein into thiols. There are several reagents, which introduce protected thiol groups into a protein (e.g. N-Succinimidyl-S-acetylthioacetate; SATA). The protecting group is removed directly before coupling the protein to the surface. With this strategy, however, no site-specific coupling can be achieved and depending on the degree of modification of the protein with SATA even multi point attachment might occur.

### **Box 3 – Was the immobilization successful?**

It is generally recommended to check the immobilization procedure at least once using a fluorescently labeled binding partner for the immobilized molecule (see steps 23 to 25). Since the chemistry used for the cantilevers and the glass slides is identical, the immobilization of the molecule, which should be coupled to the cantilever, can also be checked on a glass slide before. When doing this, a negative control using exactly the same molecule without a thiol group should always be included. One should consider that buying or preparing a fluorescently labeled detection molecule might be cheaper than performing many unsuccessful single molecule experiments.

#### **Suggested negative controls:**

***DNA or RNA oligonucleotide:*** exactly the same sequence without the thiol modification

***Protein:*** use the same protein without the mutation or without the attached C-terminal cysteine (see Box 2)

***Peptide:*** exactly the same sequence without the cysteine (in the case of peptides, the usage of the same sequence is highly recommended since other peptides can have different charge or hydrophobicity resulting in another tendency to bind non-specifically)

#### **Suggested detection molecules:**

***DNA oligonucleotide:*** A complementary oligonucleotide with a fluorescent label is the ideal reagent to detect the immobilized molecule. Many different labels are commonly available to suit the specific needs for the detection. However we recommend the usage of Cyanin 3.

***RNA oligonucleotide:*** Depending on the secondary structure of the RNA it might not be possible to use a complementary RNA or DNA oligonucleotide. Maybe it is known that the RNA binds another ligand specifically. Then it makes sense to label this ligand with a

fluorophor. If there are no other possibilities the RNA oligonucleotide might be fluorescently labeled itself.

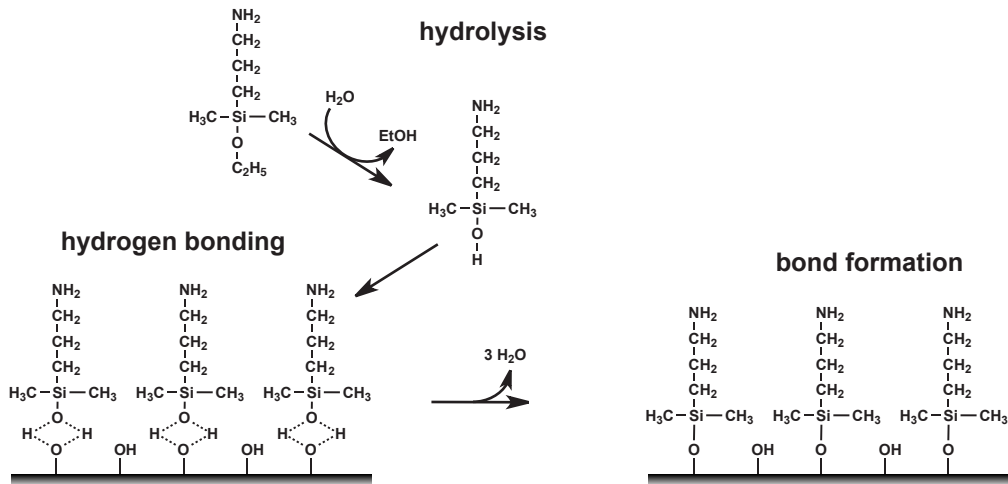
**Protein:** If a recombinant protein was prepared as described in Box 2 it might be easiest to use a fluorescently labeled antibody against the His tag (for example Penta-His from Qiagen). Alternatively, every potential ligand (antibody, antigen, covalent inhibitor, etc.) can be fluorescently labeled and used for this purpose.

**Peptide:** Again, the detection might be performed using a specific binding partner carrying a fluorescent label. If this cannot be achieved easily, there might be the option to include the amino acid sequence of one of the “standard fusion tags” (His tag, FLAG tag, Strep tag, HA tag, etc.) into the peptide sequence at either terminus. For these tags fluorescently labeled detection molecules are commercially available.

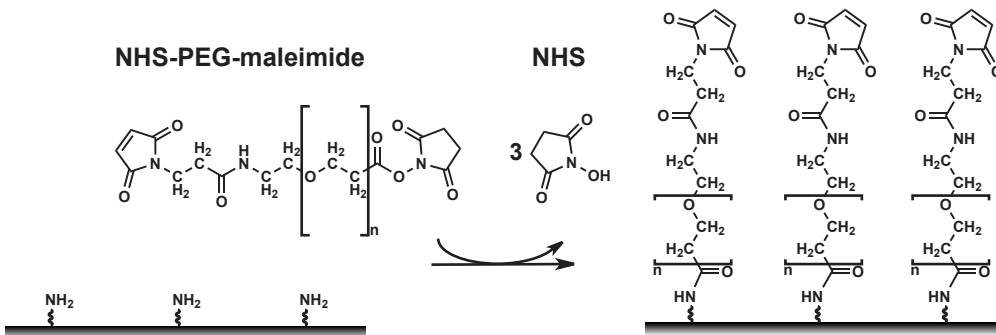
## Figure 1

**Overview of the immobilization procedure.** The protocol can be used for every kind of surface, which can react with silanes, and consists of 3 steps: a Cleaned surfaces are incubated in a solution of pure monoalkoxy amino silane to prevent the formation of crosslinks between silane molecules which might lead to the formation of multilayers. After placing the silane on the surface the silane is not covalently bound yet. In order to obtain covalent bonds the surface needs to be baked to remove the layer of water, which stabilizes the interaction of the silane with the surface via hydrogen bonds. b After having obtained amino functionalized surfaces the hetero bifunctional NHS-PEG-maleimide spacer is coupled to the surface yielding a covalent amide bond between the PEG and the silane. c Finally, the reduced biomolecules are coupled to the PEG surface displaying thiol reactive maleimide groups. The surface density of the biomolecules is adjusted in this last step and needs to be optimized for the desired application.

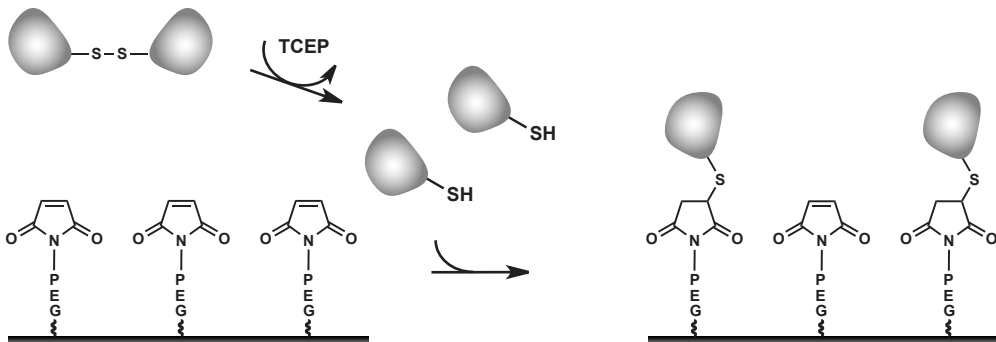
## A generation of amino functionalized surfaces



## B coupling of the hetero bifunctional PEG crosslinker



## C coupling of the biomolecule via its thiol group



## **P3**

### **8.3 Affinity-Matured Recombinant Antibody Fragments Analyzed by Single Molecule Force Spectroscopy**

J. Morfill, K. Blank, C. Zahnd, B. Luginbühl, F. Kühner, K-E. Gottschalk, A.  
Plückthun and H. E. Gaub

*Biophysical Journal* (2007) 93:3583-3590

## Affinity-Matured Recombinant Antibody Fragments Analyzed by Single-Molecule Force Spectroscopy

Julia Morfill,\* Kerstin Blank,\* Christian Zahnd,<sup>†</sup> Beatrice Luginbühl,<sup>†</sup> Ferdinand Kühner,\* Kay-E. Gottschalk,\* Andreas Plückthun,<sup>†</sup> and Hermann E. Gaub\*

\*Lehrstuhl für Angewandte Physik and Center for Nanoscience, Ludwig-Maximilians-Universität München, Munich, Germany; and <sup>†</sup>Biochemisches Institut, Universität Zürich, Zürich, Switzerland

**ABSTRACT** For many applications, antibodies need to be engineered toward maximum affinity. Strategies are in demand to especially optimize this process toward slower dissociation rates, which correlate with the (un)binding forces. Using single-molecule force spectroscopy, we have characterized three variants of a recombinant antibody single-chain Fv fragment. These variants were taken from different steps of an affinity maturation process. Therefore, they are closely related and differ from each other by a few mutations only. The dissociation rates determined with the atomic force microscope differ by one order of magnitude and agree well with the values obtained from surface plasmon resonance measurements. However, the effective potential width of the binding complexes, which was derived from the dynamic force spectroscopy measurements, was found to be the same for the different mutants. The large potential width of 0.9 nm indicates that both the binding pocket and the peptide deform significantly during the unbinding process.

### INTRODUCTION

In recent years, recombinant antibodies have become increasingly important as therapeutic agents (1–4), for proteomics applications, and for diagnostic assays (5). In addition, they might prove useful as building blocks for the self-assembly of nanostructures. Antibodies with high affinities are needed in most of the cases, and the application sets the requirements.

Several different approaches have been developed for the *in vitro* affinity maturation of recombinant antibody fragments such as single-chain Fv (scFv) or Fab fragments (1–4, 6–11). If a number of clones have been selected, they need to be characterized according to their affinity improvement. Often, the determination of the equilibrium dissociation constant  $K_D$  yields sufficient information, and a ranking of mutants is possible. However, in some cases it is necessary to measure the kinetic rate constants of both the binding and unbinding processes as a way to describe both equilibrium and kinetic behavior in an application. This characterization is of particular importance if the affinity improvement needs to be correlated with the structure of the mutants and the position and type of the acquired mutation(s), e.g., during an affinity maturation process and its structural interpretation.

Several different methods exist for the determination of the equilibrium dissociation constant. It can be measured, e.g., with ELISA (enzyme-linked immunosorbent assay)

(12), surface plasmon resonance (SPR) (13), fluorescence titration (14), and fluorescence-activated cell sorting (9). The quantitative measurement of the kinetic constants can be more difficult. Usually, SPR is used for this purpose. To obtain exact values, one has to take care of possible rebinding effects on the surface during the dissociation phase, which can slow down the apparent dissociation rate,  $k_{off}$ , artificially. In addition, in the case of slow dissociation rates ( $k_{off} < 10^{-5} \text{ s}^{-1}$ ), an accurate determination of  $k_{off}$  is difficult due to the small amount of analyte dissociating. The signal change can then approach the rate of drift of the SPR instrument (15).

Single-molecule force spectroscopy is an alternative method to obtain information about the unbinding process of receptor-ligand interactions. This measurement method has been used for a broad range of different biological systems, including antibody-antigen interactions (14,16–21). Force spectroscopy makes use of the fact that  $k_{off}$  is increased if an external force is applied. Measuring the rupture forces of a receptor-ligand interaction for different loading rates (dynamic force spectroscopy) allows extrapolation to the dissociation rate at zero force, which represents the natural  $k_{off}$ . Furthermore, force spectroscopy yields additional information about the width of the potential  $\Delta x$  (see below). This information might be useful for interpreting the influence of different mutations on unbinding kinetics. Mutations could lead to changes in the geometry of the binding site or to other conformational rearrangements of the molecule, resulting in an altered unbinding pathway that can be detected as a change in the width of the potential.

In this report we have analyzed three different variants of an scFv fragment with force spectroscopy using an atomic force microscope (AFM). These variants represent a series of clones obtained from different steps of an affinity maturation process by using ribosome display (11,22). All three variants

Submitted May 10, 2007, and accepted for publication July 11, 2007.

Address reprint requests to Julia Morfill, Lehrstuhl für Angewandte Physik and Center for Nanoscience, LMU München, Amalienstrasse 54, D-80799, Munich, Germany. Tel.: 49-89-2180-2306; Fax: 49-89-2180-2050; E-mail: julia@morfill.de.

Kerstin Blank's present address is Institut de Science et d'Ingénierie Supramoléculaires (ISIS-ULP), Laboratoire de Biologie Chimique, 8, allée Gaspard Monge, BP 70028, F-67083 Strasbourg cedex, France.

Editor: Jane Clarke.

© 2007 by the Biophysical Society  
0006-3495/07/11/3583/08 \$2.00

doi: 10.1529/biophysj.107.112532

bind the same peptide antigen, which is a random coil in solution. The crystal structure of a closely related variant complexed with the antigen has been determined (11). As the peptide forms an  $\alpha$ -helical structure in complex with the antibody fragment, the peptide is considered to undergo a conformational change upon binding and unbinding, giving rise to more complex unbinding pathways compared to the unbinding of small and compact ligands. The study described here focuses on two aspects. First, we address some methodological aspects of the AFM measurements, mainly dealing with data evaluation. The obtained data were used to compare two different methods for analyzing AFM measurements. Both methods are based on the well-established Bell-Evans model (23–25) and allow determination of the  $k_{\text{off}}$  and  $\Delta x$  values. In addition, the  $k_{\text{off}}$  values obtained from force spectroscopy measurements were compared with the  $k_{\text{off}}$  values determined by SPR. Second, as the variants only differ in a few amino acids it is possible to examine the influence of these mutations, acquired during the affinity maturation process, on  $k_{\text{off}}$  and  $\Delta x$ .

## MATERIALS AND METHODS

### Cloning, expression, and purification of the antibody fragments

The three scFv variants (C11, C11L34, and 52SR4) were expressed with a C-terminal His tag followed by a cysteine to allow site-specific immobilization of the scFv fragments. The plasmids for periplasmic expression were based on the pAK series (26). The gene for coexpression of the periplasmic chaperone Skp was introduced (27). The original His tag was replaced by a tag of six histidines followed by two glycines and a cysteine. For the expression and purification of the scFv variants, the protocol of Hanes et al. (22) was slightly modified. Briefly, the *Escherichia coli* strain SB536 was transformed with the plasmids. Cells were grown at 25°C in SB medium (20 g L<sup>-1</sup> tryptone, 10 g L<sup>-1</sup> yeast extract, 5 g L<sup>-1</sup> NaCl, 50 mM K<sub>2</sub>HPO<sub>4</sub>) containing 30  $\mu\text{g ml}^{-1}$  chloramphenicol. Expression was induced with 1 mM isopropyl- $\beta$ -D-thiogalactopyranoside at an OD<sub>600</sub> between 1.0 and 1.5. The cells were harvested by centrifugation 3 h after induction. Cell disruption was achieved by French Press lysis. The scFv fragments were purified using two chromatography steps. After chromatography on a Ni<sup>2+</sup>-NTA column (Qiagen, Hilden, Germany) using standard protocols, the eluted fraction was directly loaded onto an affinity column with immobilized antigen. The fractions from the affinity column were dialyzed against coupling buffer (50 mM sodium phosphate, pH 7.2, 50 mM NaCl, 10 mM EDTA) and concentrated using Centricon YM-10 (Millipore, Eschborn, Germany). The actual concentration of the purified scFv fragments was determined by measuring the absorbance at 280 nm. The extinction coefficients of the different variants were calculated using the program Vector NTI (Invitrogen, Karlsruhe, Germany). The preparations of the purified proteins were adjusted to a concentration of 0.8 mg ml<sup>-1</sup> and stored in aliquots at -80°C.

### Preparation of slides and cantilevers for the AFM measurements

Poly(ethylene) glycol (PEG) was used as a spacer between the biomolecules and the surfaces. Due to its properties, PEG is an ideal spacer for force spectroscopy measurements (14,16,19,21,28–30). It provides protein-resistant surfaces (31), thereby reducing the number of nonspecific binding events.

In addition, PEG shows a characteristic force-extension curve, allowing discrimination between specific and nonspecific interactions during data analysis. The scFv fragments possessing a C-terminal Cys were immobilized on an amino-functionalized slide using a heterobifunctional NHS-PEG-maleimide (molecular mass 5000 g/mol; Nektar, Huntsville, AL). The peptide GCN4(7P14P) (RMKQLEPKVEELLPKNYHLENEVARLKKLVGER), which has been used for the generation and affinity-maturation of antibodies, was used for the force spectroscopy measurements (11,22,32). A cysteine residue followed by three glycines was attached to the N-terminus during peptide synthesis (Jerini Peptide Technologies, Berlin, Germany). The Cys was used to couple the peptide to an amino-functionalized cantilever, again using the NHS-PEG-maleimide spacer (Fig. 1).

The cantilevers (Bio-lever, Olympus, Tokyo, Japan) were cleaned and functionalized as described (21). However, instead of epoxy-functionalized cantilevers, amino-modified surfaces were prepared using 3-aminopropyl-dimethylethoxysilane (ABCR, Karlsruhe, Germany). Commercially available amino-functionalized slides (Slide A, Nexterion, Mainz, Germany) were

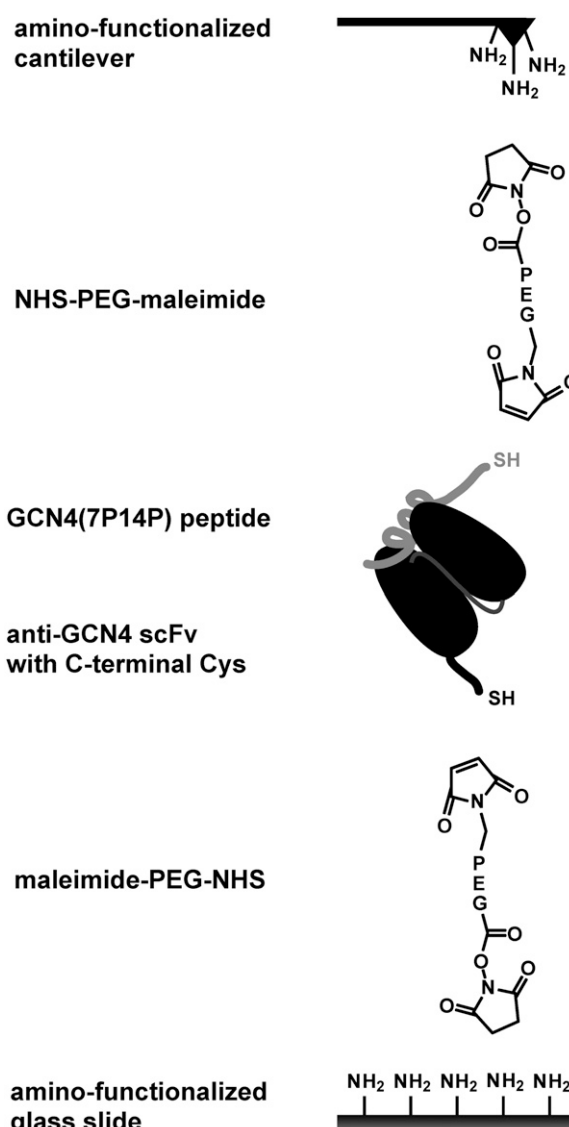


FIGURE 1 Experimental setup. The antibody fragments having a C-terminal cysteine were covalently immobilized onto amino-functionalized glass slides using a heterobifunctional PEG spacer. The same coupling chemistry was used for immobilizing the peptide on the cantilever.

used. For the next steps, both surfaces (slide and cantilever) were treated in parallel as described (33). Briefly, they were incubated in borate buffer, pH 8.5, to increase the fraction of unprotonated amino groups for coupling to the NHS groups of the PEG. NHS-PEG-maleimide was dissolved at a concentration of 50 mM in borate buffer at pH 8.5 and incubated on the surfaces for 1 h. In parallel, the peptide and one of the scFv fragments were reduced using TCEP beads (Perbio Science, Bonn, Germany) to generate free thiols. After washing both surfaces with ultrapure water, a solution of the peptide (200  $\mu$ M) was incubated on the cantilever and a solution of the scFv fragment (0.13 mg/ml) was incubated on the slide for 1 h. Finally, both surfaces were rinsed with phosphate-buffered saline (PBS) (10 mM Na phosphate, pH 7.4, 137 mM NaCl, 2.7 mM KCl) to remove noncovalently bound material and stored in PBS until use.

## Force spectroscopy

All force measurements were performed with a MFP-1D AFM (Asylum Research, Santa Barbara, CA) at room temperature in PBS. Cantilever spring constants ranged from 6 to 8 pN/nm (B-Bio-Lever) and were measured as described previously (34,35). During one experiment, the approach and retract velocity were held constant, whereas the applied force was adjusted by changing the distance between the cantilever tip and the surface to obtain single binding events. To achieve good statistics, several hundreds of approach-retract cycles were carried out. To obtain measurements over a broad range of different loading rates, several experiments were performed, each at a different retract velocity ranging from 50 nm/s to 10  $\mu$ m/s.

## Data extraction

The obtained data was converted into force-extension curves. From these force-extension curves, the rupture force (the force at which the antibody-antigen complex ruptures), the rupture length, and the corresponding loading rate were determined using the program Igor Pro 5.0 (Wavemetrics, Lake Oswego, OR) and a custom-written set of procedures. The rupture force was determined as described previously (24,25). The loading rate was determined using the two-state freely jointed chain fit to the force-extension curve, according to previous studies (36).

## Data analysis

To analyze the data set obtained from one experiment, which was recorded at a constant retract velocity, the rupture forces, rupture lengths, and loading rates were plotted in three histograms. The loading rates were plotted logarithmically. The histograms were analyzed with two methods based on the Bell-Evans model (23–25). The first method refers to the basis of dynamic force spectroscopy and has been applied broadly in the past to analyze force spectroscopy data. The histograms of the force and the loading rate (plotted logarithmically) for each data set, i.e., for each retract velocity, were fitted with a Gaussian distribution to determine the maxima. Finally, these obtained maxima of the Gaussian distributions were plotted in a force versus loading rate diagram. The maximum force (from the Gaussian distribution of the force histogram) represents the most probable force  $F^*$ :

$$F^* = \frac{k_B \times T}{\Delta x} \ln \frac{\dot{F} \times \Delta x}{k_B \times T \times k_{\text{off}}}, \quad (1)$$

where  $k_B$  is the Boltzmann constant,  $T$  the temperature,  $\Delta x$  the potential width,  $k_{\text{off}}$  the natural dissociation rate at zero force, and  $\dot{F}$ , equal to  $dF/dt$ , is the loading rate. From a linear fit of the force versus loading rate (pictured logarithmically) plot and Eq. 1,  $k_{\text{off}}$  and  $\Delta x$  of the antibody-antigen complex can be determined.

Whereas the first analysis method requires measurements at different retract velocities, the values for  $k_{\text{off}}$  and  $\Delta x$  can be obtained from one data set measured at one retract velocity when using the second analysis method. The second method was introduced by Friedsam et al. (25) and takes into account

a distribution of spacer lengths of the used PEG. The bond rupture probability density function  $p(F)$  was calculated according to Eq. 2 for every spacer length in the measured rupture-length histogram:

$$p(F) = k_{\text{off}} \times \exp\left(\frac{F \times \Delta x}{k_B \times T}\right) \frac{1}{\dot{F}} \times \exp\left(-k_{\text{off}} \int_0^F dF' \exp\left(\frac{F' \times \Delta x}{k_B \times T}\right) \frac{1}{\dot{F}}\right). \quad (2)$$

These  $p(F)$  functions were weighted according to their occurrence in the rupture-length histogram and finally added up. This results in a semihypothetical rupture-force histogram based on the two input parameters  $k_{\text{off}}$  and  $\Delta x$ , which were varied to find the best fit to the measured rupture-force histogram. Additionally, to account for the detection noise, the probability density function,  $p(F)$ , was convolved with a Gaussian distribution. The standard deviation of the Gaussian distribution equals the typical noise value of the cantilever, which was used in the experiment (37).

The main difference between these two analysis methods is that the first method only uses the maxima of the force and loading-rate distributions for the fit procedure. As a consequence, the spacer length of the PEG spacer is averaged, which therefore results in an averaged loading rate. In contrast, the second method takes into account a certain spacer-length distribution. In addition, with the second method, the force histogram is fitted directly with the probability density function and therefore considers the shape of the histogram. To analyze the experimentally obtained data using the second method, it is extremely important to eliminate nonspecific interactions during data analysis, as they can shift or broaden the force histogram. This would lead to incorrect fit values for  $k_{\text{off}}$  and  $\Delta x$ .

## Proof of specificity

To prove the specificity of the force spectroscopy measurements, experiments were performed either without the antibody fragment or without the peptide. By measuring the antibody fragment, attached to the surface, against a cantilever tip passivated with PEG, >1000 force-extension curves were recorded. Thereby, <1% nonspecific interactions were detected. The measurements without the peptide led to similar results.

## SPR measurements

For the measurement of  $k_{\text{off}}$  (25°C) of the scFv fragments with a Biacore 3000 instrument (Biacore, Freiburg, Germany), two different assay formats were used: 1), an antigen-immobilized assay for clone C11; and 2), an antibody-immobilized assay for the clones C11L34 and 52SR4. For both formats, a CM5 sensor chip (Biacore) was modified via amine coupling according to the manufacturer's protocol. For assay format 1, biotinylated peptide GCN4(7P14P) (22) was bound to the amine-coupled neutravidin (Perbio Science, Lausanne, Switzerland) surface to a final signal intensity of 20 RU. Clone C11 was diluted in HBST buffer (20 mM Hepes, pH 7.2, 150 mM NaCl, 0.005% Tween 20) to final concentrations of 20–100 nM and injected on the chip. For format 2, either clone C11L34 or clone 52SR4 was amine-coupled to the surface to a final signal intensity of 100–300 RU. A series of GCN4(7P14P) peptide solutions in HBST buffer in the range 50–0.023 nM, using threefold dilutions, was injected on the chip. After binding, dissociation was followed at a flow rate of 100  $\mu$ l/min and 50  $\mu$ l/min for assay formats 1 and 2, respectively. The dissociation phase was fitted globally, using the single-exponential fit function of the program SigmaPlot or Clamp, alternatively.

## RESULTS

The antibody fragments used in our study are closely related and have been described previously (11,22). They all bind

the same peptide antigen, which has been derived from the transcription factor GCN4. For a better understanding, we briefly summarize the positions (Table 1) and the influence of the mutations. The antibody fragments differ in a few amino acids only. Starting from clone C11, clone C11L34 has one mutation. Compared to clone C11L34, clone 52SR4 has four additional mutations. The mutated amino acids do not interact directly with the antigen, although three of them are located in the complementarity determining regions (CDRs). Mutation L42 (N→S; AHo numbering scheme (38)), which has already been introduced into clone C11L34, may reduce the flexibility of CDR L1 and may allow a more favorable domain orientation. Mutation L107 (A→V) of clone 52SR4 lies in close proximity to mutation L42 and therefore might contribute to this effect. Therefore, these two mutations are thought to influence the loop position and/or geometry and the relative domain orientation and thereby optimize the binding geometry. Most likely, mutation L135 (N→D in clone 52SR4) has a different effect. The exchange of asparagine to aspartic acid introduces a negative charge. This charged residue might be able to establish an electrostatic interaction with the peptide, as the peptide has a positive charge at the corresponding position (K15 in the original peptide). From the structure, it appears that the mutations L13 (T→S in clone 52SR4) and H30 (S→L in clone 52SR4) only have a small contribution to the affinity.

To analyze the interaction of the variants with their peptide antigen, force spectroscopy measurements were performed using an atomic force microscope (AFM). To be able to compare the two different analysis methods for the AFM data (see Materials and Methods) and the data from the surface plasmon resonance (SPR) measurements, it was essential to minimize nonspecific interactions and to ensure that only specific and single antibody-peptide interactions were analyzed. As an effective approach to discriminate nonspecific interactions, we chose to attach both the antibody fragment and the peptide via PEG, which is known to provide protein-resistant surfaces. The antibody fragment was coupled to a surface containing covalently attached PEG and the peptide was immobilized onto the cantilever tip in the same way (Fig. 1). An additional advantage of this approach is that PEG acts as an elastic spacer with a known length. When the

PEG spacers are stretched, the elastic properties of this molecule lead to a characteristic extension curve, which can be fitted with the two-state freely jointed chain (FJC) fit with the values from the literature (36). Specific interactions were thus selected by considering only those extension curves that show the appropriate length and the characteristic shape of the PEG spacers.

In all experiments, the surface was approached with the tip of the cantilever, allowing the antibody-peptide complex to bind. Subsequently, the cantilever was retracted and the antibody-peptide complex was loaded with an increasing force until the complex finally ruptured and the cantilever relaxed back into its equilibrium position. The force applied to this complex was recorded as a function of the distance between the cantilever tip and the surface. Fig. 2 shows a series of typical force-extension curves representing the interaction between clone C11 and the peptide. To obtain good statistics, several hundred force-extension curves were recorded for all three variants. From these curves, the rupture force, rupture length, and corresponding loading rate were determined. Fig. 3 *a* shows the rupture-force, Fig. 3 *b* the rupture-length, and Fig. 3 *c* the loading-rate distributions for the interaction of clone C11 with the peptide, measured at a retract velocity of 1000 nm/s. The rupture-force histogram in Fig. 3 *a* was fitted with a Gaussian distribution (*dotted curve*) and exhibits a most probable force of 55.6 pN. The Gaussian distribution of the histogram of the loading rates (plotted logarithmically) (Fig. 3 *c*) shows a maximum at 2697 pN s<sup>-1</sup>. The maxima of the force and the loading-rate distributions were determined for a large range of loading rates, and in the following step were plotted in a force versus loading rate (pictured logarithmically) diagram (first analysis method). The determination of  $k_{\text{off}}$  and  $\Delta x$  from a linear fit to these data points using Eq. 1 is described in Materials and Methods. The measurements of clone C11 resulted in a  $k_{\text{off}}$  of  $(3.9 \pm 5.7) \times 10^{-3} \text{ s}^{-1}$  and a  $\Delta x$  of  $(0.88 \pm 0.12) \text{ nm}$ . For a complete analysis of the experimental results, all data sets for the three variants were examined by the first analysis method, using Eq. 1 (Fig. 4). The obtained values for  $k_{\text{off}}$  and  $\Delta x$  for all three variants are listed in Table 1.

Additionally, the measured rupture-force distributions for all three variants were analyzed using the second analysis

**TABLE 1** Summary of the results obtained for the three different clones

Clone	Mutations	AFM analysis method 1		AFM analysis method 2*		SPR
		$k_{\text{off}} (\text{s}^{-1})$	$\Delta x (\text{nm})$	$k_{\text{off}} (\text{s}^{-1})$	$\Delta x (\text{nm})$	$k_{\text{off}} (\text{s}^{-1})$
C11	None	$(3.9 \pm 5.7) \times 10^{-3}$	$0.88 \pm 0.12$	$(1.0 \pm 0.3) \times 10^{-3}$	$0.90 \pm 0.02$	$2.9 \times 10^{-3}$
C11L34	L42 (N→S)	$(4.9 \pm 7.2) \times 10^{-4}$	$0.90 \pm 0.10$	$(2.0 \pm 1.0) \times 10^{-4}$	$1.00 \pm 0.10$	$3.0 \times 10^{-4}$
52SR4	L13 (T→S)	$(8.2 \pm 7.9) \times 10^{-4}$	$0.92 \pm 0.07$	$(5.0 \pm 2.0) \times 10^{-4}$	$0.86 \pm 0.04$	$1.6 \times 10^{-4}$
	L42 (N→S)					
	L107 (A→V)					
	L135 (N→D)					
	H30 (S→L)					

\* $k_{\text{off}}$  and  $\Delta x$  for the analysis method 2 have been determined for  $dF/dt$  between 80 and 90 pN s<sup>-1</sup>.

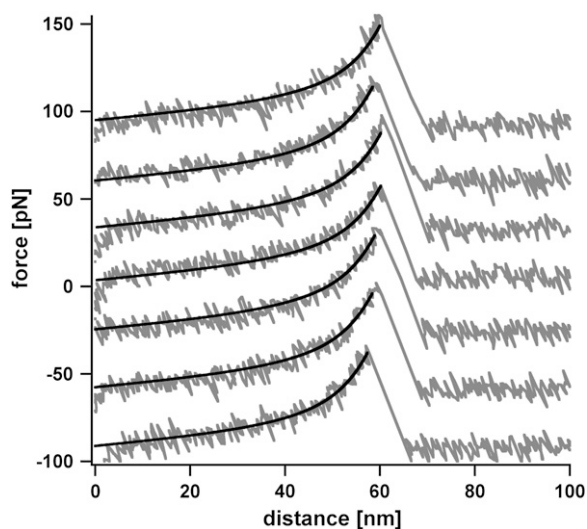


FIGURE 2 Example of seven typical force-extension curves. The force-extension curves show the rupture event of the scFv C11 peptide complex, experimentally recorded at a retract velocity of 1000 nm/s. The elastic behavior of the spacer PEG can be described using the two-state FJC fit (solid curve) with the values from the literature (36). The values for the rupture force, rupture length, and corresponding loading rate were obtained from these force-extension curves.

method based on the probability density function  $p(F)$  (Eq. 2). The respective fit for the presented data set of clone C11 is shown in Fig. 3 (solid curve). For this clone, the second analysis method resulted in a  $\Delta x$  of  $(0.9 \pm 0.03)$  nm and a  $k_{\text{off}}$  of  $(2.0 \pm 3.0) \times 10^{-3} \text{ s}^{-1}$ . To be able to compare the obtained values for  $k_{\text{off}}$  and  $\Delta x$  for all the variants, we performed an analysis for similar loading rates in the lower range ( $dF/dt$  between 80 and 90  $\text{pN s}^{-1}$ ). The values for all three variants are also listed in Table 1. A comparison of the three different variants shows that the  $\Delta x$  and  $k_{\text{off}}$  values, determined using the first and second analysis methods, are identical within the analysis error (first analysis method). The values for  $k_{\text{off}}$  obtained from the SPR measurements are also summarized in Table 1. Within experimental error, both methods (AFM and SPR) exhibit consistent values for  $k_{\text{off}}$  for all three variants.

A statistical analysis of the results obtained from the first analysis method using the AFM was performed using Student's  $t$ -tests. The potential widths  $\Delta x$  of the three variants have been determined from the corresponding slopes of the linear fits (see Materials and Methods), which are identical with a probability of 96%. Thus, none of the mutations changes the potential width,  $\Delta x$ , significantly. In contrast, the dissociation rates,  $k_{\text{off}}$ , were determined from the interpolation to zero force. Since the slopes are identical, the significance in the difference in  $k_{\text{off}}$  can be obtained from the intersections of the linear fits with the ordinate.

These intersections for clones C11 and C11L34 are different with a probability of 66%. This rather low value results from the lack of data points at very low loading rates

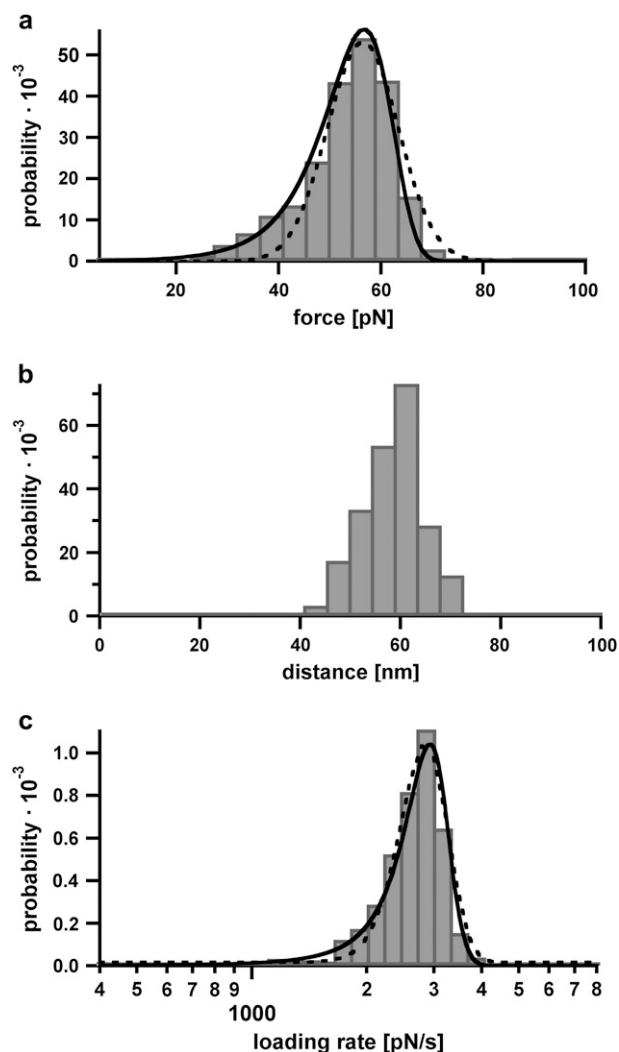


FIGURE 3 Example of the obtained rupture-force, rupture-length, and loading-rate distributions. (a) Rupture-force histogram of the scFv C11 peptide complex. The rupture-force histogram contains 859 rupture events and was fitted with a Gaussian curve (dotted curve). Additionally, the obtained rupture-force distribution was compared with the calculated probability density function  $p(F)$  (solid curve) with  $\Delta x = (0.9 \pm 0.03)$  nm and  $k_{\text{off}} = (2.0 \pm 3.0) \times 10^{-3} \text{ s}^{-1}$ , as described in Materials and Methods. Within the analysis error, the values for  $\Delta x$  and  $k_{\text{off}}$  are identical for both analysis methods (experimental data obtained from the first analysis method are shown in Fig. 4). (b) Rupture-length histogram of the scFv C11 peptide complex. (c) Histogram of the loading rates of the scFv C11 peptide complex, plotted logarithmically. This histogram was fitted with a Gaussian curve (dotted curve) and additionally compared with the calculated probability density function  $p(\ln \dot{F})$  (solid curve).

that are not accessible with the AFM. Since the AFM data from the first and second analysis methods are in full accordance with the SPR results, a comparison of the  $k_{\text{off}}$  values clearly reveals that clone C11L34 has a slower dissociation rate than clone C11 (5–8-fold). This is the consequence of one single-point mutation at the end of CDR L1 of the  $V_L$  domain. Clones C11L34 and 52SR4 differ in four amino acids. However, these mutations do not show any significant influence on  $k_{\text{off}}$ .

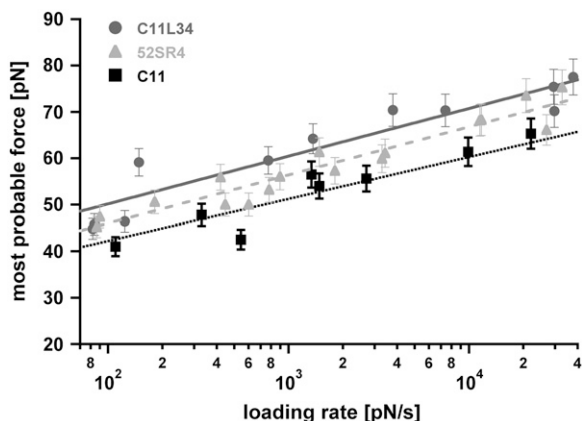


FIGURE 4 Diagram showing the most probable rupture force plotted against the corresponding loading rate (pictured logarithmically) for all three scFv-peptide complexes. The data points were gained from the Gaussian fits of the rupture-force histogram and the histogram of loading rates, plotted logarithmically. The black data points (■) correspond to the scFv C11 peptide complex. These data points were fitted to a straight line (*black dotted curve*). From this linear fit,  $\Delta x = (0.88 \pm 0.12)$  nm and  $k_{\text{off}} = (3.9 \pm 5.7) \times 10^{-3} \text{ s}^{-1}$  were obtained. The dark gray data set (●) was measured for the forced dissociation of the scFv C11L34 peptide complex. From the linear fit (*dark gray*),  $\Delta x = (0.90 \pm 0.10)$  nm and  $k_{\text{off}} = (4.9 \pm 7.2) \times 10^{-4} \text{ s}^{-1}$  were obtained. Finally, the scFv 52SR4 peptide complex, plotted with light gray data points (▲) and the linear fit (*light gray dashed curve*) gave  $\Delta x = (0.92 \pm 0.07)$  nm and  $k_{\text{off}} = (8.2 \pm 7.9) \times 10^{-4} \text{ s}^{-1}$ .

## DISCUSSION

Receptor-ligand interactions often display a marked deviation from the linear relation between the unbinding force and the logarithm of the force-loading rate, predicted by the Bell-Evans model. Biotin-Avidin (39) and digoxigenin-antibody interactions (21) are prominent examples, where two barriers in series are suggested due to the marked nonlinearity. Alternatively, other models based on the Kramers theory (40,41) are discussed. For the antibody-peptide system investigated here, we found that the simplest level of analysis, which is based on a mechanothermally activated transition in a two-level system, already provided a satisfactory description of the unbinding process: for each mutant, the plot in Fig. 4 revealed a linear relation, showing virtually indistinguishable slopes and a separation of the intersections at zero force.

However, this simple approach has two severe drawbacks: it requires the measurement of a series of data points for a wide spectrum of force-loading rates and it assumes a monodisperse spacer length. This has only a limited validity if polymeric spacers, such as PEG, are used (as in this study). We therefore also employed a second method, which analyzes the shape of the rupture-force histogram and requires only one loading rate. We found that this method provided more accurate results (see Table 1), as it considers the distribution of the spacer lengths (25). For all three variants used in this study, the  $k_{\text{off}}$  and  $\Delta x$  values agreed well for both analysis methods for slow loading rates. In general, the second analysis method may also be applied to faster loading rates (data

not shown). However, for faster loading rates, the experimental noise increases and, therefore, additional correction factors would have to be included for analysis of the data (37). In addition, one should keep in mind that the Bell-Evans model assumes a constant  $\Delta x$  over the entire range of loading rates, which is probably not the case for most receptor-ligand systems. Therefore, using the second analysis method for slow loading rates ensures that the potential width is not changed, as the system is still close to equilibrium.

Last but not least, this second method also reduces the experimental effort significantly, as the potential width and the dissociation rate are obtained from one experiment at one loading rate only, thereby making the method competitive with SPR measurements. This is particularly true in view of the rebinding problems that may hamper SPR analysis for very low  $k_{\text{off}}$  values. A decreasing  $k_{\text{off}}$  results in an increasing binding force, thus making this regime favorable for single-molecule force spectroscopy. The main advantage, however, lies in the accessibility of an otherwise not measurable parameter of receptor-ligand interactions: their potential width,  $\Delta x$ .

The most remarkable finding of our study is that the different variants have a more or less identical potential width, which is calculated from the indistinguishable slopes of the linear fits of the different clones. Although, in the Bell-Evans model, the potential width is only a rough measure of the steepness of the binding potential or, in other words, a measure of how far the binding complex can be stretched and deformed until it finally ruptures, this finding leads to the conclusion that neither the geometry of the binding site nor the unbinding pathways were significantly affected by the mutations introduced during the affinity-maturation process. Compared to the potential width of the well characterized antfluorescein scFv fragments (14,42,43), the value for  $\Delta x$  obtained for the system analyzed here is significantly higher. In addition, for the fluorescein system a correlation between  $\Delta x$  and  $k_{\text{off}}$  was observed, which is not the case for the variants investigated here. When comparing both systems, one has to keep in mind that there are three significant differences. First, in the fluorescein system the mutations are mainly located in the binding sites of the scFv fragments. Second, in the fluorescein system, affinity-matured scFv fragments were taken as a starting point and systematic mutations were made to reduce the number of contacts in the binding site. In the study presented here, a starting clone was improved sequentially by directed evolution. And finally, fluorescein is a very rigid antigen, which cannot adopt multiple conformations. In contrast, the peptide antigen of the system described here is a random coil in solution and has an  $\alpha$ -helical structure in complex with the antibody fragment.

Considering these aspects, the observed differences for  $\Delta x$  can be rationalized as follows: during the forced unbinding, one or both binding partners can be deformed in the direction of the applied force. If a certain point is reached, the deformation is so large that the complex dissociates. In the case of the antfluorescein scFvs, the number and quality of the

contacts in the binding site differs among the analyzed scFvs. As fluorescein is a rigid antigen, only the scFv fragment itself can respond to the applied force. Therefore, by stretching the scFv fragment with an externally applied force, it is deformed in the direction of the force. Finally, the contacts in the binding site cannot resist the force any longer, and the complex ruptures. Therefore, the correlation between  $\Delta x$  and  $k_{\text{off}}$  can be explained by the fact that a complex with a higher  $k_{\text{off}}$  is stabilized by a lower number of contacts and can withstand smaller deformations until the complex dissociates.

However, for the system investigated here, the antigen is extremely flexible. The helical peptide is most likely stretched along its axis, so that a deformation can be induced easily by applying force. In addition, a deformation of the scFv, as observed for the anti-fluorescein scFvs (42), might occur. That the values for  $\Delta x$  are identical leads to the conclusion that the unbinding process is the same for all variants: before the antibody-peptide complex finally dissociates, the peptide has to be stretched far enough to destabilize the complex. This point of destabilization is identical for the variants. As no additional contacts have been introduced in the binding site during the affinity-maturation process, a stabilization of the complex is only conceivable if the binding site is more rigid and possesses a higher resistance to the applied force. This can be realized with a lower  $k_{\text{off}}$  value. Indeed, the only relevant mutation that improves  $k_{\text{off}}$  among the mutants examined here is the mutation in clone C11L34, which is assumed to reduce the flexibility of CDR L1. This interpretation can also be supported by the fact that the flexibility of the binding pocket can be reduced during the affinity maturation process in vivo, as found in other antibody systems (44–46).

This latter finding is an interesting aspect of the affinity maturation process. However, more data from more, different variants would be needed to investigate whether evolution to higher affinity generally results in more rigid binding sites. Furthermore, it would be of great interest to investigate the forced unbinding process of the antibody-peptide system in much greater detail. As the structure of the complex is known, molecular dynamics simulations in combination with additional experiments can provide further insights (42,43,47). For example, it would be interesting to measure whether truncated or mutated peptides show an altered potential width. In addition, the system investigated here is an interesting model system to investigate whether the unbinding pathway is influenced by the direction of the applied force. This can be easily tested by changing the site of attachment of the peptide. A more detailed understanding of the response of biological systems to externally applied forces is of great importance. Even thermodynamically very stable complexes can rupture at low forces, and, conversely, complexes with identical dissociation rates can withstand a broad range of forces depending on the potential width. As more and more systems are discovered that respond to forces in their natural environment, a more detailed knowledge is required of the mechanisms governing how molecules sense and detect forces in biological systems.

The authors thank Julia Sedlmair and Holger Hesse for help in recording a large number of data points as well as Gregor Neuert, Hauke Clausen-Schaumann, Matthias Rief, Robert Lugmaier, Ludmila Mendelevitch, Elias Puchner, Thomas Nicolaus, and Gary Morfill for helpful discussions.

This work was supported by the European Union and the Deutsche Forschungsgemeinschaft.

## REFERENCES

1. Yang, W. P., K. Green, S. Pinz-Sweeney, A. T. Briones, D. R. Burton, and C. F. Barbas 3rd. 1995. CDR walking mutagenesis for the affinity maturation of a potent human anti-HIV-1 antibody into the picomolar range. *J. Mol. Biol.* 254:392–403.
2. Chen, Y., C. Wiesmann, G. Fuh, B. Li, H. W. Christinger, P. McKay, A. M. de Vos, and H. B. Lowman. 1999. Selection and analysis of an optimized anti-VEGF antibody: crystal structure of an affinity-matured Fab in complex with antigen. *J. Mol. Biol.* 293:865–881.
3. Maynard, J. A., C. B. Maassen, S. H. Leppla, K. Brasky, J. L. Patterson, B. L. Iverson, and G. Georgiou. 2002. Protection against anthrax toxin by recombinant antibody fragments correlates with antigen affinity. *Nat. Biotechnol.* 20:597–601.
4. Wu, H., D. S. Pfarr, Y. Tang, L. L. An, N. K. Patel, J. D. Watkins, W. D. Huse, P. A. Kiener, and J. F. Young. 2005. Ultra-potent antibodies against respiratory syncytial virus: effects of binding kinetics and binding valence on viral neutralization. *J. Mol. Biol.* 350:126–144.
5. Kusnezow, W., and J. D. Hoheisel. 2002. Antibody microarrays: promises and problems. *Biotechniques*. 33(Suppl.):14–23.
6. Schier, R., J. Bye, G. Apell, A. McCall, G. P. Adams, M. Malmqvist, L. M. Weiner, and J. D. Marks. 1996. Isolation of high-affinity monomeric human Anti-c-erbB-2 single chain Fv using affinity-driven selection. *J. Mol. Biol.* 255:28–43.
7. Chen, G., I. Dubrawsky, P. Mendez, G. Georgiou, and B. L. Iverson. 1999. In vitro scanning saturation mutagenesis of all the specificity determining residues in an antibody binding site. *Protein Eng.* 12:349–356.
8. Boder, E. T., K. S. Midelfort, and K. D. Wittrup. 2000. Directed evolution of antibody fragments with monovalent femtomolar antigen-binding affinity. *Proc. Natl. Acad. Sci. USA.* 97:10701–10705.
9. van den Beucken, T., H. Pieters, M. Steukers, M. van der Vaart, R. C. Ladner, H. R. Hoogenboom, and S. E. Hufton. 2003. Affinity maturation of Fab antibody fragments by fluorescent-activated cell sorting of yeast-displayed libraries. *FEBS Lett.* 546:288–294.
10. Graff, C. P., K. Chester, R. Begent, and K. D. Wittrup. 2004. Directed evolution of an anti-carcinoembryonic antigen scFv with a 4-day monovalent dissociation half-time at 37° C. *Protein Eng. Des. Sel.* 17:293–304.
11. Zahnd, C., S. Spinelli, B. Luginbühl, P. Amstutz, C. Cambillau, and A. Plückthun. 2004. Directed in vitro evolution and crystallographic analysis of a peptide-binding single chain antibody fragment (scFv) with low picomolar affinity. *J. Biol. Chem.* 279:18870–18877.
12. Friguet, B., A. F. Chaffotte, L. Djavadi-Ohanian, and M. E. Goldberg. 1985. Measurements of the true affinity constant in solution of antigen-antibody complexes by enzyme-linked immunosorbent assay. *J. Immunol. Methods.* 77:305–319.
13. Nieba, L., A. Krebber, and A. Plückthun. 1996. Competition BIAcore for measuring true affinities: large differences from values determined from binding kinetics. *Anal. Biochem.* 234:155–165.
14. Schwesinger, F., R. Ros, T. Strunz, D. Anselmetti, H. J. Güntherodt, A. Honegger, L. Jermutus, L. Tiefenauer, and A. Plückthun. 2000. Unbinding forces of single antibody-antigen complexes correlate with their thermal dissociation rates. *Proc. Natl. Acad. Sci. USA.* 97:9972–9977.
15. Schier, R., A. McCall, G. P. Adams, K. W. Marshall, H. Merritt, M. Yim, R. S. Crawford, L. M. Weiner, C. Marks, and J. D. Marks. 1996. Isolation of picomolar affinity anti-c-erbB-2 single-chain Fv by molecular evolution of the complementarity determining regions in the center of the antibody binding site. *J. Mol. Biol.* 263:551–567.

16. Hinterdorfer, P., W. Baumgartner, H. J. Gruber, K. Schilcher, and H. Schindler. 1996. Detection and localization of individual antibody-antigen recognition events by atomic force microscopy. *Proc. Natl. Acad. Sci. USA*. 93:3477–3481.
17. Dammer, U., M. Hegner, D. Anselmetti, P. Wagner, M. Dreier, W. Huber, and H. J. Güntherodt. 1996. Specific antigen/antibody interactions measured by force microscopy. *Biophys. J.* 70:2437–2441.
18. Allen, S., X. Chen, J. Davies, M. C. Davies, A. C. Dawkes, J. C. Edwards, C. J. Roberts, J. Sefton, S. J. B. Tendler, and P. M. Williams. 1997. Detection of antigen-antibody binding events with the atomic force microscope. *Biochemistry*. 36:7457–7463.
19. Ros, R., F. Schwesinger, D. Anselmetti, M. Kubon, R. Schafer, A. Plückthun, and L. Tiefenauer. 1998. Antigen binding forces of individually addressed single-chain Fv antibody molecules. *Proc. Natl. Acad. Sci. USA*. 95:7402–7405.
20. Moy, V. T., E. L. Florin, and H. E. Gaub. 1994. Intermolecular forces and energies between ligands and receptors. *Science*. 266:257–259.
21. Neuert, G., C. Albrecht, E. Pamir, and H. E. Gaub. 2006. Dynamic force spectroscopy of the digoxigenin-antibody complex. *FEBS Lett.* 580:505–509.
22. Hanes, J., L. Jeremut, S. Weber-Bornhauser, H. R. Bosshard, and A. Plückthun. 1998. Ribosome display efficiently selects and evolves high-affinity antibodies in vitro from immune libraries. *Proc. Natl. Acad. Sci. USA*. 95:14130–14135.
23. Bell, G. I. 1978. Models for the specific adhesion of cells to cells. *Science*. 200:618–627.
24. Evans, E., and K. Ritchie. 1999. Strength of a weak bond connecting flexible polymer chains. *Biophys. J.* 76:2439–2447.
25. Friedsam, C., A. K. Wehle, F. Kühner, and H. E. Gaub. 2003. Dynamic single-molecule force spectroscopy: bond rupture analysis with variable spacer length. *J. Phys. Condens. Matter*. 15:S1709–S1723.
26. Krebber, A., S. Bornhauser, J. Burmester, A. Honegger, J. Willuda, H. R. Bosshard, and A. Plückthun. 1997. Reliable cloning of functional antibody variable domains from hybridomas and spleen cell repertoires employing a reengineered phage display system. *J. Immunol. Methods*. 201:35–55.
27. Bothmann, H., and A. Plückthun. 1998. Selection for a periplasmic factor improving phage display and functional periplasmic expression. *Nat. Biotechnol.* 16:376–380.
28. Kienberger, F., V. P. Pastushenko, G. Kada, H. J. Gruber, C. K. Riener, H. Schindler, and P. Hinterdorfer. 2000. Static and dynamic properties of single poly(ethylene glycol) molecules investigated by force spectroscopy. *Single Mol.* 1:123–128.
29. Morfill, J., F. Kühner, K. Blank, R. Lugmaier, J. Sedlmair, and H. E. Gaub. 2007. B-S transition in short oligonucleotides. *Biophys. J.* 93:2400–2409.
30. Kühner, F., J. Morfill, R. A. Neher, K. Blank, and H. E. Gaub. 2007. Force-induced DNA slippage. *Biophys. J.* 92:2491–2497.
31. Alcantar, N. A., E. S. Aydil, and J. N. Israelachvili. 2000. Polyethylene glycol-coated biocompatible surfaces. *J. Biomed. Mater. Res.* 51:343–351.
32. Berger, C., S. Weber-Bornhauser, J. Eggenberger, J. Hanes, A. Plückthun, and H. R. Bosshard. 1999. Antigen recognition by conformational selection. *FEBS Lett.* 450:149–153.
33. Blank, K., J. Morfill, and H. E. Gaub. 2006. Site-specific immobilization of genetically engineered variants of *Candida antarctica* lipase B. *ChemBioChem*. 7:1349–1351.
34. Butt, H. J., and M. Jaschke. 1995. Calculation of thermal noise in atomic-force microscopy. *Nanotechnology*. 6:1–7.
35. Hugel, T., and M. Seitz. 2001. The study of molecular interactions by AFM force spectroscopy. *Macromol. Rapid Commun.* 22:989–1016.
36. Oesterhelt, F., M. Rief, and H. E. Gaub. 1999. Single molecule force spectroscopy by AFM indicates helical structure of poly(ethylene glycol) in water. *New J. Phys.* 1:6.1–6.11.
37. Kühner, F., and H. E. Gaub. 2006. Modelling cantilever-based force spectroscopy with polymers. *Polym.* 47:2555–2563.
38. Honegger, A., and A. Plückthun. 2001. Yet another numbering scheme for immunoglobulin variable domains: an automatic modeling and analysis tool. *J. Mol. Biol.* 309:657–670.
39. Merkel, R., P. Nassoy, A. Leung, K. Ritchie, and E. Evans. 1999. Energy landscapes of receptor-ligand bonds explored with dynamic force spectroscopy. *Nature*. 397:50–53.
40. Sheng, Y. J., S. Jiang, and H. K. Tsao. 2005. Forced Kramers escape in single-molecule pulling experiments. *J. Chem. Phys.* 123:91102–91102-4.
41. Schlierf, M., and M. Rief. 2006. Single-molecule unfolding force distributions reveal a funnel-shaped energy landscape. *Biophys. J.* 90:L33–L35.
42. Paci, E., A. Caffisch, A. Plückthun, and M. Karplus. 2001. Forces and energetics of hapten-antibody dissociation: a biased molecular dynamics simulation study. *J. Mol. Biol.* 314:589–605.
43. Curcio, R., A. Caffisch, and E. Paci. 2005. Change of the unbinding mechanism upon a mutation: a molecular dynamics study of an antibody-hapten complex. *Protein Sci.* 14:2499–2514.
44. Wedemayer, G. J., P. A. Patten, L. H. Wang, P. G. Schultz, and R. C. Stevens. 1997. Structural insights into the evolution of an antibody combining site. *Science*. 276:1665–1669.
45. Yin, J., E. C. Mundorff, P. L. Yang, K. U. Wendt, D. Hanway, R. C. Stevens, and P. G. Schultz. 2001. A comparative analysis of the immunological evolution of antibody 28B4. *Biochemistry*. 40:10764–10773.
46. Jimenez, R., G. Salazar, J. Yin, T. Joo, and F. E. Romesberg. 2004. Protein dynamics and the immunological evolution of molecular recognition. *Proc. Natl. Acad. Sci. USA*. 101:3803–3808.
47. Heymann, B., and H. Grubmüller. 2001. Molecular dynamics force probe simulations of antibody/antigen unbinding: entropic control and nonadditivity of unbinding forces. *Biophys. J.* 81:1295–1313.

## **P4**

### **8.4 B-S Transition in Short Oligonucleotides**

J. Morfill, F. Kühner, K. Blank, R. Lugmaier, J. Sedlmair and H. E. Gaub

*Biophysical Journal* (2007) 93:2400-2409

## B-S Transition in Short Oligonucleotides

Julia Morfill, Ferdinand Kühner, Kerstin Blank, Robert A. Lugmaier, Julia Sedlmair, and Hermann E. Gaub  
Lehrstuhl für Angewandte Physik & Center for Nanoscience, Ludwig-Maximilians-Universität München, Munich, Germany

**ABSTRACT** Stretching experiments with long double-stranded DNA molecules in physiological ambient revealed a force-induced transition at a force of 65 pN. During this transition between B-DNA and highly overstretched S-DNA the DNA lengthens by a factor of 1.7 of its B-form contour length. Here, we report the occurrence of this so-called B-S transition in short duplexes consisting of 30 basepairs. We employed atomic-force-microscope-based single molecule force spectroscopy to explore the unbinding mechanism of two short duplexes containing 30 or 20 basepairs by pulling at the opposite 5' termini. For a 30-basepair-long DNA duplex the B-S transition is expected to cause a length increase of 6.3 nm and should therefore be detectable. Indeed 30% of the measured force-extension curves exhibit a region of constant force (plateau) at 65 pN, which corresponds to the B-S transition. The observed plateaus show a length between 3 and 7 nm. This plateau length distribution indicates that the dissociation of a 30-basepair duplex mainly occurs during the B-S transition. In contrast, the measured force-extension curves for a 20-basepair DNA duplex exhibited rupture forces below 65 pN and did not show any evidence of a B-S transition.

### INTRODUCTION

The elastic and mechanical behavior of long double-stranded DNA has been investigated using a variety of techniques, which cover a broad range of forces from a few piconewton up to several hundred piconewtons. For example, magnetic beads (1), glass microneedles (2), optical traps (3,4), and the atomic force microscope (AFM) (5) have been used to investigate the response of long  $\lambda$ -DNA to externally applied forces. These stretching experiments of  $\lambda$ -DNA exhibit a highly cooperative transition at a force of 65–70 pN, which refers to the conversion of B-DNA into an overstretched conformation called S-DNA. Hereby the DNA molecule stretches up to a factor of 1.7 of its B-form contour length. Besides force spectroscopy experiments, molecular dynamic simulations, and various theoretical approaches give detailed insights into the processes of this so-called B-S transition (6–13).

A detailed analysis of the B-S transition was performed with single molecule force spectroscopy using the AFM. In 1999, Rief et al. (5) were the first to analyze long  $\lambda$ -DNA with the AFM.  $\lambda$ -DNA was adsorbed nonspecifically to a gold surface and picked up with a cantilever in the next step. Upon retraction, the double-stranded DNA molecule, attached via the 3' and 5' terminus of the same strand is stretched between the cantilever tip and the gold surface until the complementary strand melts off. Fig. 1 shows a typical example of the force-extension curves for  $\lambda$ -DNA, which exhibits an overstretching B-S transition at a force of 65 pN. During this

transition the force-extension curve shows a lengthening of the double-stranded  $\lambda$ -DNA by a factor of 1.7. At forces higher than 65 pN a second transition occurs, which is discussed in the literature to be a force-induced melting transition (5). During this transition the double-stranded DNA is split into two single strands. Upon further extension, the force increases drastically until the remaining single-stranded DNA finally ruptures. The B-S transition and the melting transition exhibit a significant thermodynamic difference: The B-S transition is represented by a force plateau in the force-extension curve and is independent of the pulling speed. Therefore, it can be considered as an equilibrium process within the timescale of the performed experiments. In contrast, the melting transition shows a very steep force increase and a pronounced speed dependence. Therefore this transition occurs in nonequilibrium (5). In contrast to this approach, theoretical analyses exist, which interpret the B-S transition as a force-induced melting transition (14,15). It was shown that this interpretation can quantitatively describe the thermodynamics of DNA overstressing (16).

In addition to  $\lambda$ -DNA, which contains a mixture of A-T and G-C basepairs, Rief et al. measured long double-stranded poly(dG-dC) and poly(dA-dT) sequences to obtain information about the sequence dependence of the B-S transition. The B-S transition for double-stranded poly(dG-dC) also occurred at a force of 65 pN whereas the force-extension curves for poly(dA-dT) sequences showed a force of 35 pN. Further investigations of the nature of the B-S transition were carried out by Clausen-Schaumann et al., Williams et al., and Wenner et al. (17–20). They analyzed the influence of the position of attachment, the salt concentration, the temperature, and the pH on the B-S transition. If the DNA molecule was attached to the cantilever tip and the gold surface with both strands simultaneously, the overstressing transition was shifted to higher force values of 105 pN and showed less

Submitted February 7, 2007, and accepted for publication May 29, 2007.

Address reprint requests to Julia Morfill, Tel.: 49-89-2180-2306; Fax: 49-89-2180-2050; E-mail: julia@morfill.de.

Kerstin Blank's present address is Institut de Science et d'Ingénierie Supramoléculaires (ISIS), Laboratoire de Biologie Chimique, 8, allée Gaspard Monge, BP 70028, 67083 Strasbourg Cedex, France.

Editor: Petra Schwille.

© 2007 by the Biophysical Society

0006-3495/07/10/2400/10 \$2.00

doi: 10.1529/biophysj.107.106112

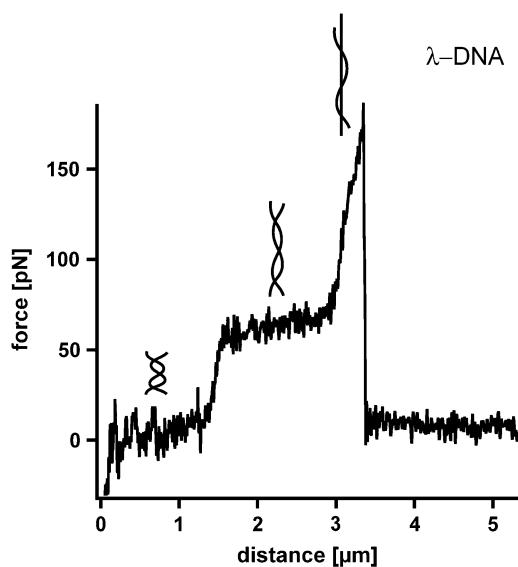


FIGURE 1 Force-extension curve of double-stranded  $\lambda$ -DNA. While retracting the cantilever from the surface with a velocity of  $16 \mu\text{m/s}$  the double-stranded  $\lambda$ -DNA is stretched. At a force between 65 and 70 pN the well-known highly cooperative B-S transition is observed. During this transition the DNA duplex lengthens by a factor of 1.7. After this transition the force increases to a value of  $\sim 170$  pN where the DNA finally ruptures.

cooperativity. For salt (NaCl) concentrations higher than 150 mM, the B-S transition occurred at forces of 65 pN. For salt concentrations lower than 150 mM the force decreased and the B-S transition exhibited less cooperativity. Without any salt, the DNA molecules denatured upon stretching and very short or no B-S plateaus were observed. Further measurements showed, that the force of the B-S transition was reduced when the temperature was increased. In addition, higher and lower pH than the physiological pH of 7.4 led to lower B-S transition forces.

Whereas all above experiments have been carried out with long double-stranded DNA, which was attached randomly to gold surfaces, a different approach was followed in the experiments of Strunz et al. (21) and Pope et al. (22). Instead of attaching double-stranded DNA to a surface and picking it up nonspecifically with the cantilever tip two complementary single strands were covalently coupled to the cantilever tip and the surface. Upon approach of the cantilever tip to the surface, the complementary DNA strands hybridized and formed a duplex. Upon retraction of the cantilever tip the hybridized DNA was loaded with an increasing force until the hydrogen bonds between the two complementary strands ruptured. An advantage of this kind of measurement is that the DNA duplex is coupled to the surface and the cantilever at a defined position and that the interaction can be probed many times to gain high statistics. In addition, if oligonucleotides are used the entire sequence of the DNA duplex is known.

In Strunz et al. the measured unbinding forces of short oligonucleotides (30, 20, and 10 basepairs) were found to be a function of the applied loading rate and the number of

basepairs. This indicates that the dissociation is a non-equilibrium process. In many cases the unbinding process of receptor ligand interactions can be described with a two-state model where one state represents the bound and the other state the unbound conformation of the interaction. Based on the work of Bell (23), Evans et al. developed a model to describe a two-state system under an externally applied force (24). The externally applied force reduces the unbinding barrier, which the ligand has to overcome by thermal fluctuations. This well-known Bell-Evans model was applied to analyze the obtained data for the different DNA duplexes. Because no B-S transition was observed in the measurements of Strunz et al. the unbinding of the DNA duplexes could be approximated with a two-state system and the unbinding forces showed the expected dependence on the loading rate. However, it was pointed out, that the B-S transition might be present, but could not be resolved due to experimental noise.

In this study, we performed single molecule force spectroscopy using high-resolution cantilevers to investigate DNA duplexes containing 20 and 30 basepairs concerning their conformational change during dissociation. In addition, these results were compared with measurements of 1000-basepair-long DNA duplexes.

These lengths for the short duplexes were chosen, because the data of Strunz et al. (21) suggest that the rupture forces of a 20 basepair duplex do not reach the critical force value of 65 pN whereas some rupture events for a 30 basepair duplex reach rupture forces higher than 65 pN. The measurements were performed at various loading rates to obtain a detailed picture of the presence of the B-S transition in short oligonucleotides.

## MATERIALS AND METHODS

### Preparation of slides and cantilevers for the measurements with $\lambda$ -DNA

$\lambda$ -BsrEII digest DNA (length distribution, 117–8454 basepairs) was purchased from Sigma (Deisenhofen, Germany). A solution containing  $123 \mu\text{g/ml}$   $\lambda$ -DNA in phosphate buffered saline (PBS) was incubated on a freshly evaporated gold surface for 30 min at a temperature of  $70^\circ\text{C}$ . Finally the gold surface was rinsed with PBS (10 mM Na phosphate, pH 7.4, 137 mM NaCl, 2.7 mM KCl) and stored in PBS until use. The force spectroscopy experiments were performed with cantilevers (Bio-lever, Olympus, Tokyo, Japan) additionally coated with gold at room temperature.

### Preparation of slides and cantilevers for the measurements with 1000-basepair-long DNA

A 1000-basepair-long DNA duplex (DNA1000s) was generated with polymerase chain reaction using 5' thiol-modified primers. The polymerase chain reaction product was purified with gel electrophoresis followed by gel extraction. The final DNA concentration, as determined from the absorbance at 260 nm was  $15 \text{ ng}/\mu\text{l}$ . The DNA, diluted in  $\text{H}_2\text{O}$ , was incubated on a gold surface in a humid chamber for 1 h. In the same way, the DNA was coupled to the cantilever (Bio-lever, Olympus) additionally coated with gold. After washing with  $\text{H}_2\text{O}$ , the cantilever and the surface, covered with  $\text{H}_2\text{O}$  were

heated up to 90°C to separate the double-stranded DNA into single strands. Finally, the surfaces were rinsed with PBS to remove unbound DNA and stored in PBS until use.

## Preparation of slides and cantilevers for the measurements with short oligonucleotides

Oligonucleotides modified with a thiol group at their 5'-termini (for details see Table 1; IBA GmbH, Göttingen, Germany; metabion GmbH, Martinsried, Germany) were immobilized on amino-functionalized surfaces using a heterobifunctional poly(ethylene glycol) (PEG) spacer (25). One oligonucleotide was immobilized on the cantilever and the oligonucleotide with the complementary sequence was coupled to the surface. The cantilevers (Bio-lever, Olympus) were cleaned as described (26). Amino-modified surfaces on the cantilevers were prepared using 3-aminopropyltrimethoxysilane (ABC R GmbH, Karlsruhe, Germany) (26). Commercially available amino-functionalized slides (Slide A, Nexterion, Mainz, Germany) were used. From now on, both surfaces (cantilever and slide) were treated in parallel as described previously (27). They were incubated in borate buffer pH 8.5 for 1 h. This step was necessary to deprotonate the amino groups for coupling to the *N*-hydroxysuccinimide (NHS) groups of the heterobifunctional NHS-PEG-maleimide (molecular weight, 5000 g/mol; Nektar, Huntsville, AL). The PEG was dissolved in a concentration of 50 mM in borate buffer at pH 8.5 and incubated on the surfaces for 1 h. In parallel, the oligonucleotides were reduced using tris (2-carboxyethyl) phosphine hydrochloride beads (Perbio Science, Bonn, Germany) to generate free thiols. After washing the surfaces with ultrapure water, a solution of the oligonucleotides (1.75 μM) was incubated on the surfaces for 1 h. Finally, the surfaces were rinsed with PBS to remove noncovalently bound oligonucleotides and stored in PBS until use.

## Force spectroscopy

All force measurements were performed in PBS containing 150 mM NaCl at room temperature using an MFP-3D AFM (Asylum Research, Santa Barbara, CA). Cantilever spring constants ranged from 7 to 20 pN/nm (B-Bio-Lever and B-Bio-Lever coated with gold) and from 30 to 40 pN/nm (A-Bio-Lever and A-Bio-Lever coated with gold) and were measured as described previously (28,29). During one experiment, the approach and retract velocity were held constant, whereas the contact time on the surface was adjusted to obtain single binding events. To achieve satisfactory statistics, several hundreds of approach-retract cycles were carried out. To obtain measurements over a broad range of different loading rates, several experiments were performed each at a different retract velocity ranging from 50 nm/s to 10 μm/s.

## Data extraction

The obtained data were converted into force-extension curves. From these force-extension curves, the rupture force (the force at which the DNA strands open), the rupture length, and the corresponding loading rate were determined using the software Igor Pro 5.0 (Wavemetrics, Lake Oswego, OR) and a custom-written set of procedures. The rupture force was defined as described previously (24,30). To determine the loading rate, the freely

jointed chain fit (FJC) to the force-extension curve was used, according to previous studies (31).

## Data analysis

To analyze the data set of one experiment, which was recorded at a constant retract velocity, the rupture forces and the corresponding loading rates were plotted in two histograms. The histograms were analyzed with two methods, which are based on the well-known Bell-Evans-model (23,24,30). For analysis of the data with the loading-rate-based method, the force and the loading rate (plotted logarithmically) histogram were fitted with a Gaussian distribution to determine the maxima of the respective histograms. These maxima were determined for each data set, ergo for each retract velocity and finally plotted in a force versus loading rate (pictured logarithmically) diagram. The maximum force represents the most probable force  $F^*$ :

$$F^* = \frac{k_B \times T}{\Delta x} \ln \frac{\dot{F} \times \Delta x}{k_B \times T \times k_{\text{off}}}, \quad (1)$$

with  $k_B$  is the Boltzmann constant,  $T$  is the temperature,  $\Delta x$  is the potential width,  $k_{\text{off}}$  is the natural dissociation rate at zero force, and  $\dot{F} = dF/dt$  is the loading rate. From a linear fit of the force versus loading rate (pictured logarithmically) plot and Eq. 1, the natural dissociation rate  $k_{\text{off}}$  and the potential width  $\Delta x$  of the DNA complex can be determined. Whereas the above-mentioned method requires measurements at different retract velocities, the values for  $k_{\text{off}}$  and  $\Delta x$  can be obtained from one data set measured at one retract velocity when using the following method, which was introduced by Friedsam et al. (30). It takes into account a distribution of the spacer lengths between the interaction, which needs to be measured and the surfaces. The bond rupture probability density function  $p(F)$  was calculated according to Eq. 2 for every spacer length in the measured rupture length histogram.

$$p(F) = k_{\text{off}} \times \exp\left(\frac{F \times \Delta x}{k_B \times T}\right) \frac{1}{F} \times \exp\left(-k_{\text{off}} \int_0^F dF' \exp\left(\frac{F' \times \Delta x}{k_B \times T}\right) \frac{1}{F'}\right). \quad (2)$$

According to the obtained rupture force histogram the  $p(F)$  functions were weighted and finally added up. This results in a semihypothetical rupture force histogram based on the two input parameters  $k_{\text{off}}$  and  $\Delta x$ , which were varied to find the best fit to the measured rupture force histogram. Therefore, the  $p(F)$ -based method also considers the shape of the measured rupture force histogram. Additionally, the probability density function  $p(F)$  was convolved with a Gaussian distribution to consider the detection noise. The standard deviation of the Gaussian distribution equals the typical noise value of the cantilever, which was used in the experiment (32).

## Proof of specificity

To prove the specificity of the interactions for the measurements with DNA30s and DNA20s, the following experiments were performed. First, single-stranded DNA was measured against surfaces or cantilevers without the complementary oligonucleotide. Less than 1% nonspecific interactions were detected in ~1000 force-extension curves. Second, measurements

**TABLE 1 DNA sequences**

DNA duplex	Sequence (cantilever)	Sequence (slide)
DNA30s	5'SH-TTTTTTTTTTTTTTTTTTTTCG TTGGTGC GGATATCTCGGTAGTG GGATACGACGATACCGAAGACAG CTCATGTTATATTATG-3'	5'SH-TTTTTTTTTTTTATCCCACTA CCGAGATATCCGACCAACG-3'
DNA20s	5'SH-TTTTTTTTTTTTTTTTTTTTCG TTGGTGC GGATATCTCGGTAGTG GGATACGACGATACCGAAGACAG CTCATGTTATATTATG-3'	5'SH-TTTTTTTTTTTCCGAGATATC CGCACCAACG-3'

were performed with noncomplementary DNA strands. Thereby <4% interactions were detected. In contrast, 47% interactions were found for two complementary DNA oligonucleotides.

In addition, force clamp experiments were performed for DNA20s and DNA30s to distinguish the measured unbinding process from a so-called bulge-slipping process, dominated by the slippage of bulges in the backbone of repetitive DNA, as shown in Kühner et al. (25,33). The obtained force plateaus for DNA30s displayed equilibrium properties and did not show any discrete lengthening steps of the DNA duplex (data not shown). In addition, the obtained plateaus, which refer to the B-S transition, occurred at much higher forces than the forces of the slipping process.

## RESULTS

To analyze the interaction between complementary DNA strands with various lengths (1000 basepairs, 30 basepairs, and 20 basepairs), single molecule force spectroscopy measurements were performed with an AFM.

### DNA1000s

The analysis of DNA containing 1000 basepairs (DNA1000s) required the following setup (see Fig. 2 *a*, inset). Complementary single-stranded DNA was covalently attached to a surface and a cantilever tip at its 5' terminus. In the next step the surface was approached with the tip of the cantilever, allowing two complementary single strands to hybridize and form a duplex. Subsequently the cantilever was retracted and the DNA duplex was loaded with an increasing force until it finally ruptured and the cantilever relaxed back into its equilibrium position. The force applied to the DNA duplex was recorded as a function of the distance between the cantilever tip and the surface. Fig. 2 *a* shows an example of a so-called force-extension curve of a DNA duplex with <1000 basepairs. At 65 pN the force-extension curve exhibits a region of constant force, which corresponds to the transition between B-DNA and the highly overstretched S-DNA (B-S transition). During this transition the DNA duplex lengthens by a factor of 1.7. In the example shown, incomplete hybridization of the DNA duplex results in a B-S transition length of only 25 nm. This corresponds to a hybridized DNA duplex containing 105 basepairs. The number of basepairs can be obtained from the length difference between the unstretched and the stretched conformation of the DNA duplex. The length of the unstretched DNA duplex can be calculated from the distance between two basepairs in double-stranded B-DNA,  $l_d = 0.34$  nm. Correspondingly a DNA duplex with 105 basepairs has a length of  $105 \times 0.34$  nm = 35.7 nm. The length of the stretched DNA duplex at the end of the B-S transition then corresponds to  $35.7 \times 1.7 = 60.7$  nm. The length difference between these two conformations (i.e., the length of the plateau) is 25 nm. Upon further extension the force increases to a value of ~130 pN where the DNA duplex finally dissociates.

Fig. 2 *b* shows the rupture force histogram of double-stranded DNA with up to 1000 basepairs, recorded at a

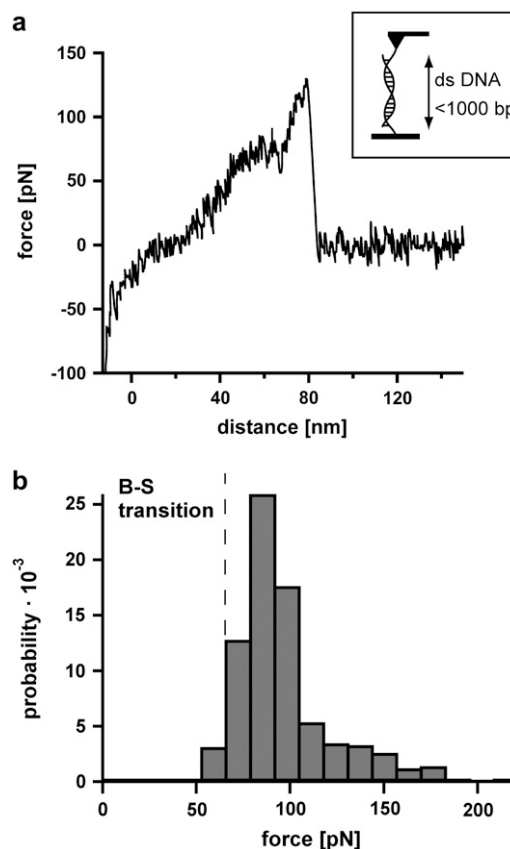


FIGURE 2 Measurements with 1000-basepair-long double-stranded DNA (DNA1000s). (*a*) Example of a typical force-extension curve. The inset shows the experimental setup. Complementary single strands are attached to the tip of a cantilever and the surface. By lowering the cantilever, the two single strands hybridize and form a duplex. By retracting the cantilever from the surface the DNA duplex is loaded with force until it finally ruptures. The force-extension curve (recorded at a velocity of 632 nm/s) exhibits a B-S transition between 65 and 75 pN. Due to incomplete hybridization the B-S transition only shows a lengthening of 25 nm, which corresponds to a DNA duplex with 105 basepairs. After the B-S transition the force increases to a value of ~130 pN where the DNA finally ruptures. (*b*) Histogram of the rupture forces of DNA1000s. The histogram ( $FWHM = 37.8$  pN) clearly shows that the DNA duplex ruptures at forces higher than the B-S transition force.

velocity of 632 nm/s. The dissociation process of double-stranded DNA with up to 1000 basepairs peaks at ~85 pN, which is significantly above the B-S transition. This leads to the conclusion that double-stranded DNA in the highly overstretched and underwound S-conformation still has a certain stability and is not separated by the transition itself. This is in accordance with Rief et al. (5), who found a second force-induced melting transition at forces higher than 65 pN. The measured rupture forces are broadly distributed (full-width at half-maximum (FWHM) is 37.8 pN). The width of this distribution is most likely the result of nonperfect hybridization of the long oligonucleotides or by their fragmentation during the harsh coupling reaction to the surfaces.

### DNA30s

The experimental setup in Fig. 3 was used for the analysis of the short oligonucleotides containing 30 basepairs (DNA30s) and 20 basepairs (DNA20s). As stated above, the length of these duplexes was chosen because the data of Strunz et al. (21) suggest that the B-S transition might be present in a 30-basepair duplex but not in a 20-basepair duplex. The sequences of these oligonucleotides have been checked carefully to minimize self-complementarity. To reduce uncertainties due to the surface chemistry the oligonucleotides were coupled to a polyethylene glycol (PEG)-modified surface and cantilever via a thiol group at their 5' termini. The usage of the elastic spacer PEG minimizes nonspecific interactions and maximizes the probability of detecting specific and single rupture events. Moreover, it prevents a shift to lower unbinding forces otherwise caused by thermal fluctuations of the cantilever.

In all experiments the surface was approached with the tip of the cantilever, allowing two single complementary DNA strands to hybridize and to form a duplex. The cantilever tip was then retracted from the surface and the DNA duplex was loaded with an increasing force until it finally ruptured. Subsequently the cantilever relaxed into its equilibrium position. The force applied to the DNA duplex was recorded as a function of the distance between the cantilever tip and the surface. The elastic properties of PEG lead to a characteristic force-extension curve if an external force is applied. This force-extension curve of the PEG spacer can be fitted with a two-state FJC model with the values from the literature (31). As the complementary oligonucleotides were coupled via a PEG spacer specific interactions can be selected based on the characteristic shape of the force-extension curve resulting from the PEG spacer and the expected length of the PEG spacer.

The B-S transition for an oligonucleotide with 30 basepairs (DNA30s) would lead to an extension of 6.3 nm from 9 nm in the B-conformation to 15.3 nm in the S-conformation and therefore should be detectable with high-resolution force spectroscopy. Fig. 4 shows two typical force-extension

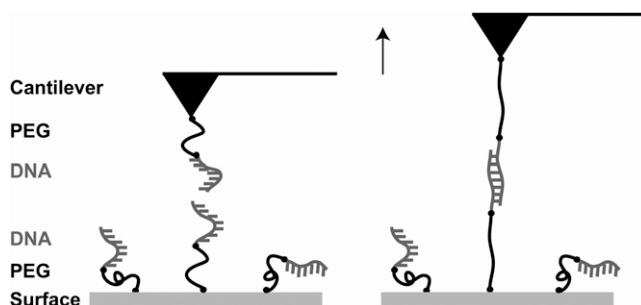


FIGURE 3 Experimental setup for the measurements with the short DNA duplexes DNA30s and DNA20s. The complementary single strands possessing a thiol-group at their 5'-termini were covalently immobilized on amino-functionalized glass slides/cantilevers using a heterobifunctional PEG spacer.

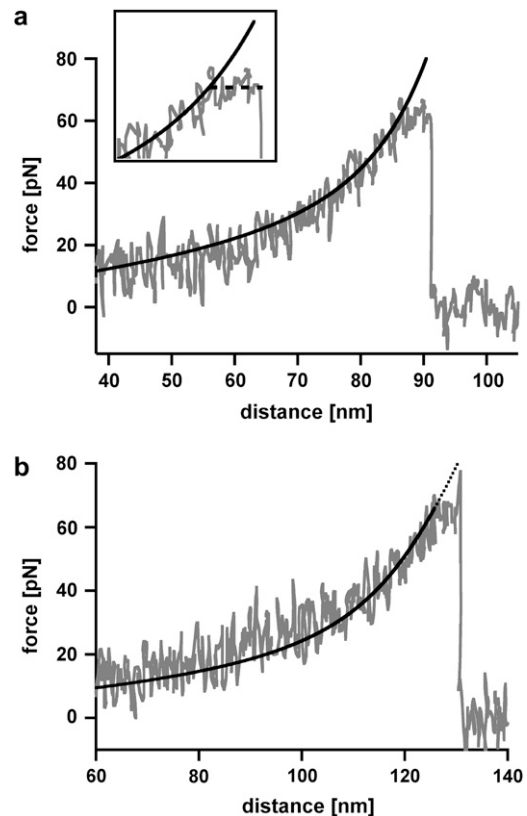


FIGURE 4 Measurements with 30-basepair-long double-stranded DNA (DNA30s). (a) Example of a force-extension curve of DNA30s possessing a B-S transition. The force-extension curve shows a rupture event of a hybridized 30 basepair DNA duplex, recorded at a retract velocity of 895 nm/s. At a force of 64 pN, the force-extension curve shows a short plateau with a length of  $\sim 6$  nm (see inset; it spans an area of 40 pN and 18 nm), which corresponds to the B-S transition. During this transition the double-stranded DNA dissociates. The black curve shows a two-state FJC-fit to the force-extension curve, which describes the elastic behavior of the PEG-DNA complex. The FJC-fit follows the force-extension curve up to the point where the DNA elongates due to the B-S transition. This region of constant force diverges from the FJC-fit by a value of up to 6 nm (shortly before rupture). (b) Example of a force-extension curve of DNA30s possessing a B-S transition followed by an additional force increase. At a force of 64 pN, the force-extension curve, which has been recorded at a retract velocity of 895 nm/s, shows a short plateau with a length of  $\sim 6$  nm. Again, this plateau corresponds to the B-S transition. After this transition the force increases to a value of 78 pN, where the DNA duplex finally dissociates. The elastic behavior of the PEG-DNA complex is described with a two-state FJC-fit (black curve), which follows the force-extension curve up to the plateau of the B-S transition. This example curve is representative for  $\sim 10\%$  of the measurements.

curves of DNA30s, recorded at a retract velocity of 895 nm/s. At a force of 64 pN the force-extension curve in Fig. 4 a shows a short plateau corresponding to a length of  $\sim 6$  nm. This plateau refers to the transition between the B-conformation and the S-conformation of the DNA duplex. During this B-S transition the DNA duplex dissociates. The force-extension curve in Fig. 4 b again shows a B-S transition at a force of 64 pN represented by a short plateau with a length of

~6 nm. Upon further extension, the force increases to a value of 78 pN, where the DNA duplex finally dissociates. The black curves in Fig. 4, *a* and *b*, represent the theoretical extension behavior of the PEG spacer, modeled with a two-state FJC function, which describes the enthalpic and entropic behavior of polymers under an externally applied force (31). For both cases the FJC curve follows the force-extension curve up to the plateau of the B-S transition. At this point the DNA molecule gets elongated and the FJC-fit therefore deviates from the obtained force-extension curve.

Fig. 5 *a* shows the measured rupture force distribution, recorded at a retract velocity of 895 nm/s. The force histogram ( $FWHM = 14.2$  pN) contains ~860 single rupture events and covers forces lower and higher than the critical B-S transition force. More than 50% of the experimentally obtained force-extension curves in this experiment ruptured at forces below 65 pN and therefore did not show the B-S transition. About 30% of the rupture events had short plateaus with lengths between 3 and 7 nm, before dissociating. Less than 10% of the force-extension curves exhibited rupture forces above the B-S transition and showed an additional force increase to 70–80 pN (see Fig. 4 *b*). The rupture force histogram was fitted in two ways: First, a Gaussian fit (not

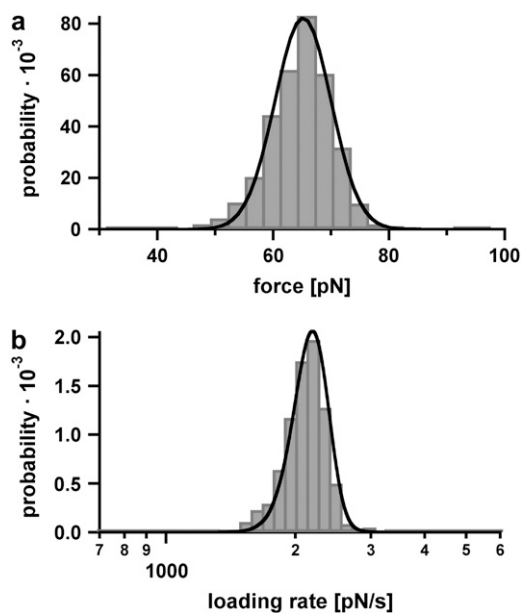


FIGURE 5 Example of the measured rupture force and loading rate distributions for the 30-basepair duplex. (*a*) Histogram of the unbinding forces of DNA30s. The histogram ( $FWHM = 14.2$  pN) contains ~860 rupture events and exhibits rupture forces above the B-S transition of 65 pN. The histogram is fitted with the calculated probability density function  $p(F)$  (black) with  $\Delta x = 4.4$  nm and  $k_{\text{off}} = 7 \times 10^{-28} \text{ s}^{-1}$ . To consider the detection noise, the probability density function was convolved with a Gaussian distribution. The standard deviation of the Gaussian distribution equals the typical noise value of the cantilever that was used (4.7 pN). (*b*) Histogram of the loading rates of DNA30s. The obtained loading rate distribution, plotted logarithmically, is compared with the calculated probability density function  $p(\ln \dot{F})$  (black).

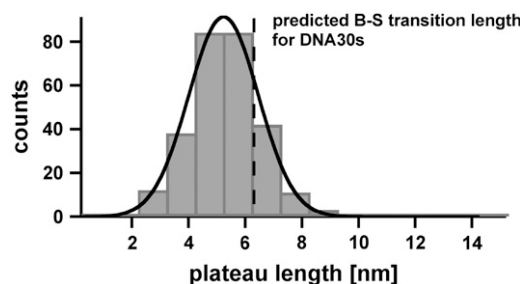


FIGURE 6 Histogram of the plateau lengths of DNA30s. The histogram ( $FWHM = 3.4$  nm) contains ~280 rupture events and shows the corresponding plateau lengths, which refer to the B-S transition. The histogram was fitted with a Gaussian curve (black) and yielded a most probable value of 5.2 nm. The theoretically predicted value equals 6.3 nm, which is compatible with the measurements within an overlap probability of 66.5%. The smaller experimental value is most likely due to melting of the DNA duplex during the B-S transition.

shown here) was used to determine the most probable rupture force  $F_{\text{max}}$  of 65 pN. Second, the rupture force histogram was fitted with the calculated probability density function  $p(F)$  (black curve) as described in the Materials and Method section, yielding a potential width of  $\Delta x = 4.4$  nm and a natural dissociation rate of  $k_{\text{off}} = 7 \times 10^{-28} \text{ s}^{-1}$ . Fig. 5 *b* shows the corresponding histogram of the loading rates (plotted logarithmically) as computed from the FJC-fits. For the cases where the FJC-fit follows the force-extension curve until the final rupture event, the determined loading rates are reliable. However, if a B-S plateau is present, the loading rate cannot be determined precisely with this procedure. Because the analysis methods are based on a two-state model, a conformational change during the dissociation process distorts the values for  $k_{\text{off}}$  and  $\Delta x$ . Therefore, the histogram in Fig. 5 *b* contains a certain error. The obtained histograms of the loading rates (plotted logarithmically) were fitted with a Gaussian distribution. This fit yields a maximum probability at  $2697 \text{ pN s}^{-1}$ .

Fig. 6 shows the histogram of the measured plateau lengths for DNA30s, which refer to the B-S transition. The histogram ( $FWHM = 3.4$  nm) contains ~280 rupture events and was fitted with a Gaussian curve (black), which has a maximum probability at 5.2 nm. The theoretical predicted value for DNA30s equals 6.3 nm and corresponds to a probability of overlap of 66.5%. This difference is significant. The shift of the distribution of the received plateau lengths to shorter lengths is most likely due to melting of the double-stranded DNA during the B-S transition.

## DNA20s

In contrast to the results obtained for DNA30s, the force-extension curves of the DNA duplex containing 20 basepairs (DNA20s) only show a sharp rupture. Fig. 7 shows a typical force-extension curve of DNA20s, recorded at a retract velocity of 1007 nm/s. The force-extension curve does not

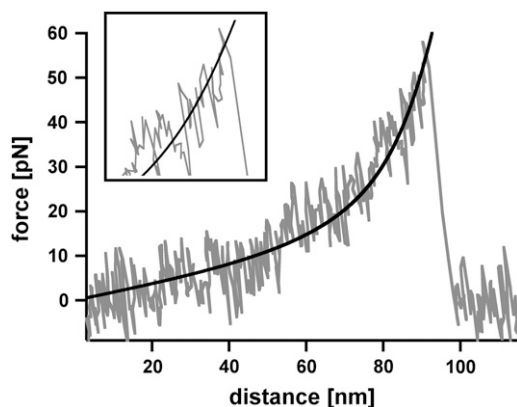


FIGURE 7 Example of a typical force-extension curve of the 20-basepair DNA duplex (DNA20s). The force-extension curve shows a rupture event of a hybridized 20-basepair DNA duplex, recorded at a retract velocity of 1007 nm/s. The DNA duplex dissociates at a force of 53 pN, without showing any evidence of the B-S transition (see *inset*). The force-extension curve of the PEG-DNA complex follows the two-state FJC-fit (*black*) without possessing a measurable deviation.

show any evidence of a B-S transition and dissociates at a force of 53 pN. Fig. 8, *a* and *b*, show the obtained rupture force and loading rate distributions, which contain  $\sim 350$  single rupture events. From a Gaussian fit to the rupture force histogram (FWHM = 13.9 pN) we obtained a most probable force of 54 pN (not shown here), which is clearly below the most probable force of DNA30s. Additionally, the rupture force distribution was fitted with the calculated probability density function  $p(F)$  (*black curve*) with  $\Delta x = 2.7$  nm and  $k_{\text{off}} = 6 \times 10^{-13} \text{ s}^{-1}$ . The histogram of the loading rates (plotted logarithmically) exhibits a maximum probability at  $1808 \text{ pN s}^{-1}$ . Compared with DNA30s, the force distribution obtained for DNA20s, which was recorded at a similar loading rate, exhibits a maximum probability at a lower force. Therefore, under equal conditions, the probability to detect the B-S transition for DNA20s is much smaller than for DNA30s, because 97% of the rupture events already take place at forces below the critical B-S transition force of 65 pN. Again the measurements were performed at various loading rates.

### Loading rate dependence

Further measurements for both DNA30s and DNA20s were performed to quantify the frequency at which B-S plateaus are observed at different loading rates and to be able to evaluate the data with a second analysis method (loading-rate-based method) to extract  $\Delta x$  and  $k_{\text{off}}$ . Each data set for DNA20s and DNA30s was measured in one single experiment with one cantilever to avoid spring calibration errors. (If data measured with different cantilevers would be combined, the spring calibration errors could lead to an imprecise analysis of the slope.)

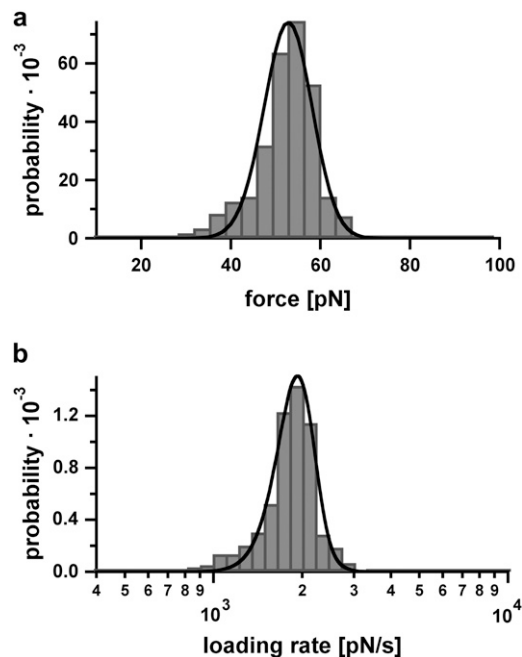


FIGURE 8 Example of the measured rupture force and loading rate distributions for the 20-basepair duplex. (*a*) Histogram of the unbinding forces of DNA20s. The histogram (FWHM = 13.9 pN) contains  $\sim 350$  rupture events. More than 97% of the rupture events occur at forces smaller than the B-S transition of 65 pN. The histogram is fitted with the calculated probability density function  $p(F)$  (*black*) with  $\Delta x = 2.7$  nm and  $k_{\text{off}} = 6 \times 10^{-13} \text{ s}^{-1}$ . To consider the detection noise, the probability density function was convolved with a Gaussian distribution. The standard deviation of the Gaussian distribution equals the typical noise value of the cantilever, which was used (5.0 pN). (*b*) Histogram of the loading rates of DNA20s. The obtained loading rate distribution, plotted logarithmically, is compared with the calculated probability density function  $p(\ln \dot{F})$  (*black*).

Measurements at faster loading rates result in higher rupture forces as described by the Bell-Evans model (23,24). Therefore, higher loading rates should increase the probability of reaching forces above 65 pN for DNA30s. This would result in a higher fraction of force-extension curves, which exhibit the B-S transition. Unfortunately, from the measured data we cannot confirm this effect unambiguously because the analysis of the detected plateaus for very high loading rates is difficult due to the limitation of the sampling rate of the data recording hardware. Interestingly, the data points still can be fitted with a straight line (Fig. 9). However, the inclination of the fit for DNA30s in the force versus loading rate diagram (plotted logarithmically) is very flat as would be expected when more and more DNA duplexes rupture during the B-S transition for faster loading rates.

Because the data sets for both DNA30s and DNA20s could be fitted with a straight line,  $\Delta x$  and  $k_{\text{off}}$  were obtained with the loading-rate-based method in addition. Although the  $p(F)$ -based method is an established method for the determination of  $\Delta x$  and  $k_{\text{off}}$  (30,34) (J. Morfill, K. Blank, C. Zahnd, B. Luginbühl, F. Kühner, K. Gottschalk, A. Plückthun, and H. E. Gaub, unpublished data), the loading-rate-based

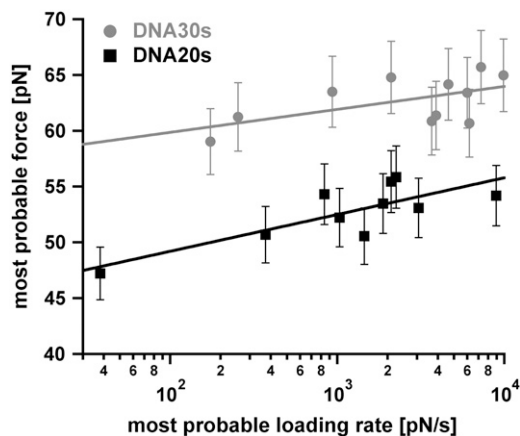


FIGURE 9 Diagram showing the most probable rupture force plotted against the appropriate most probable loading rate (pictured logarithmically) for DNA30s and DNA20s. The data points were gained from the Gaussian fits of the rupture force histogram and the histogram of the loading rates, plotted logarithmically. The gray data points (*circles*) refer to the measurements with DNA30s, the black data points (*squares*) correspond to DNA20s. These respective data points are fitted with a straight line according to the loading-rate-based analysis method. The values for  $\Delta x$  and  $k_{\text{off}}$  are obtained from Eq. 1. For DNA30s the values are  $\Delta x = (4.63 \pm 2.25)$  nm and  $k_{\text{off}} = (9.62 \times 10^{-28} \pm 3.23 \times 10^{-26})$  s $^{-1}$ . For DNA20s the values are  $\Delta x = (2.89 \pm 0.77)$  nm and  $k_{\text{off}} = (8.11 \times 10^{-14} \pm 7.77 \times 10^{-13})$  s $^{-1}$ .

method is the commonly used method. For DNA20s the following values for  $\Delta x$  and  $k_{\text{off}}$  were obtained:  $\Delta x = (2.89 \pm 0.77)$  nm and  $k_{\text{off}} = (8.11 \times 10^{-14} \pm 7.77 \times 10^{-13})$  s $^{-1}$ . For DNA30s the values are  $\Delta x = (4.63 \pm 2.25)$  nm and  $k_{\text{off}} = (9.62 \times 10^{-28} \pm 3.23 \times 10^{-26})$  s $^{-1}$ . These values are in good agreement with the values obtained with the  $p(F)$ -based analysis method.

## DISCUSSION

As indicated in the introduction, Strunz et al. measured the unbinding forces of short complementary oligonucleotides with 30, 20, and 10 basepairs (21). In their measurements they did not observe the B-S transition. However, it was pointed out, that a few unbinding events of the duplex, consisting of 30 basepairs, occur at forces higher than the critical force of the B-S transition. Due to experimental noise the B-S transition could not be resolved in their study. To analyze this critical force regime in greater detail, we performed single molecule force spectroscopy experiments with short DNA duplexes consisting of 20 basepairs (DNA20s) and 30 basepairs (DNA30s) with high-resolution cantilevers. To obtain good statistics, both complementary DNA strands were covalently immobilized to a cantilever tip and a surface. The use of identical chemistry on both sides (cantilever tip and surface) and the use of PEG as a spacer reduce the probability of nonspecific binding events to a minimum. Therefore, a high frequency of specific interactions allowed the measurement of a high number of force-extension curves at various

loading rates. The usage of Bio-levers ensured a high force resolution and therefore a detailed analysis of the obtained data.

The recorded force-extension curves for DNA30s clearly show a deviation from the two-state FJC-fit and exhibit a region of constant force at 65 pN. By assuming that PEG follows its characteristic extension curve, we conclude that the DNA duplex is elongated by 3–7 nm (see Fig. 6) and that this lengthening refers to the transition between the B-conformation and the highly overstretched S-conformation of the DNA. The obtained force-extension curves for the oligonucleotide DNA20s do not show any deviation from the two-state FJC-fit (see Fig. 7) for all applied loading rates and mainly exhibit rupture forces below the B-S transition. We conclude that in our experimental setup the applied loading rates are not high enough to reach the critical force of the B-S transition for DNA20s. Therefore, DNA20s can be approximated with a two-state system and the methods used for the analysis of the data are applicable to this system. As expected, higher loading rates shift the rupture force distribution for DNA20s to higher values and therefore to higher rupture forces. The determined value for  $k_{\text{off}}$  can be considered to represent the natural off-rate of this particular DNA duplex.

In contrast, many rupture events for DNA30s exhibit the typical force plateau of the B-S transition. This leads to the following problems for the analysis of the data. First, as the most probable force increases with the loading rate, one would expect, that a higher fraction of duplexes reaches the critical force of the B-S transition for higher loading rates. As indicated earlier, from the measured data we cannot confirm this effect unambiguously. However, an increasing fraction of duplexes, which reaches the B-S transition, would jolt the rupture force histogram and therefore would shift the maximum probability of the rupture force to lower forces. Second, due to the occurrence of the B-S transition for DNA30s, the determination of the loading rate by means of the two-state FJC-fit is inaccurate. Third, the fact that S-DNA is present with a certain frequency marks a “third state”. Hence, the data analysis based on a two-state system, leads to imprecise values for the potential width  $\Delta x$  and the dissociation rate  $k_{\text{off}}$ . All these effects can contribute to the relatively flat slope of DNA30s in the plot of the most probable rupture forces against the corresponding most probable loading rates (Fig. 9). Therefore, for DNA30s the obtained value for  $k_{\text{off}}$  most likely does not represent the natural off-rate although the data can be fitted with a straight line (within the statistical errors) when using the loading-rate-based analysis method.

As has been shown recently by Kühner et al. (36,37), different pulling angles  $\phi$  will affect the measured rupture forces, detected by the cantilever, of short DNA duplexes. These measured rupture forces decrease by a factor of  $\cos(\phi)$  for increasing pulling angles and reduce the most probable rupture force of a 30-basepair duplex to a value of  $\sim 30$  pN for a pulling angle of  $\sim 65^\circ$ . In these experiments the DNA

hybridizes when the cantilever comes in contact with the surface. Because the PEG-DNA complexes form random coils at the surface and the cantilever tip (see Fig. 3), the anchor points for the two hybridizing oligos are in close proximity so that the applied force is nearly vertical when the cantilever is retracted. Thus, within a window of  $\pm 10^\circ$  the pulling angle has very little influence and only results in 2% smaller rupture forces. This shift in the rupture force is below the error of measurement. Therefore, small variations in the pulling angle will hardly affect the measured rupture and also B-S transition forces.

The finding that the B-S transition can be observed in short oligonucleotides has various important implications for force-based experiments with DNA oligonucleotides. Oligonucleotides have been used as DNA handles for the immobilization of RNA to different surfaces (38). In addition, DNA can be used as a force standard. This force standard can be used for detection purposes if an unknown molecular interaction exhibits a higher or lower rupture force (39). In both cases, one has to consider that the rupture of double-stranded DNA cannot be described accurately with the existing models for rupture forces above 65 pN. Whereas the existence of the B-S transition in short duplexes complicates the use of DNA oligonucleotides for the above-mentioned applications, it also opens up new opportunities for the analysis of the mechanism of sequence-specific DNA binders. The effects of cisplatin on the B-S transition (40) have been investigated in detail using  $\lambda$ -DNA. The possibility of using oligonucleotides provides control over the length and the sequence of the DNA duplex. Therefore, the number of potential binding sites of sequence-specific binders can be controlled exactly. Sequence-specific DNA binders are an important class of molecules because they can influence the DNA replication. Many of these are used for cancer therapies (41,42). The opportunity to investigate existing drugs and potential drug candidates may provide new insights into the binding mechanism to DNA and in turn provide design principles for new DNA binding molecules.

## SUPPLEMENTARY MATERIAL

To view all of the supplemental files associated with this article, visit [www.biophysj.org](http://www.biophysj.org).

The authors thank Angelika Kardinal for the preparation of the DNA1000s, and Gregor Neuert, Elias Puchner, Ludmila Mendelevitch, and Kay Gottschalk for helpful discussions.

This work was supported by the European Union and the Deutsche Forschungsgemeinschaft.

## REFERENCES

- Smith, S. B., L. Finzi, and C. Bustamante. 1992. Direct mechanical measurements of the elasticity of single DNA-molecules by using magnetic beads. *Science*. 258:1122–1126.
- Cluzel, P., A. Lebrun, C. Heller, R. Lavery, J. L. Viovy, D. Chatenay, and F. Caron. 1996. DNA: an extensible molecule. *Science*. 271:792–794.
- Smith, S. B., Y. J. Cui, and C. Bustamante. 1996. Overstretching B-DNA: the elastic response of individual double-stranded and single-stranded DNA molecules. *Science*. 271:795–799.
- Wang, M. D., H. Yin, R. Landick, J. Gelles, and S. M. Block. 1997. Stretching DNA with optical tweezers. *Biophys. J.* 72:1335–1346.
- Rief, M., H. Clausen-Schaumann, and H. E. Gaub. 1999. Sequence-dependent mechanics of single DNA molecules. *Nat. Struct. Biol.* 6: 346–349.
- Lebrun, A., and R. Lavery. 1996. Modelling extreme stretching of DNA. *Nucleic Acids Res.* 24:2260–2267.
- Lavery, R., and A. Lebrun. 1999. Modelling DNA stretching for physics and biology. *Genetica*. 106:75–84.
- Lebrun, A., and R. Lavery. 1998. Modeling the mechanics of a DNA oligomer. *J. Biomol. Struct. Dyn.* 16:593–604.
- Konrad, M. W., and J. I. Bolonick. 1996. Molecular dynamics simulation of DNA stretching is consistent with the tension observed for extension and strand separation and predicts a novel ladder structure. *J. Am. Chem. Soc.* 118:10989–10994.
- Ahsan, A., J. Rudnick, and R. Bruinsma. 1998. Elasticity theory of the B-DNA to S-DNA transition. *Biophys. J.* 74:132–137.
- MacKerell, A. D., and G. U. Lee. 1999. Structure, force, and energy of a double-stranded DNA oligonucleotide under tensile loads. *Eur. Biophys. J.* 28:415–426.
- Marko, J. F. 1997. Stretching must twist DNA. *Europhys. Lett.* 38: 183–188.
- Kosikov, K. M., A. A. Gorin, V. B. Zhurkin, and W. K. Olson. 1999. DNA stretching and compression: large-scale simulations of double helical structures. *J. Mol. Biol.* 289:1301–1326.
- Rouzina, I., and V. A. Bloomfield. 2001. Force-induced melting of the DNA double helix. 1. Thermodynamic analysis. *Biophys. J.* 80:882–893.
- Rouzina, I., and V. A. Bloomfield. 2001. Force-induced melting of the DNA double helix. 2. Effect of solution conditions. *Biophys. J.* 80: 894–900.
- Williams, M. C., I. Rouzina, and V. A. Bloomfield. 2002. Thermodynamics of DNA interactions from single molecule stretching experiments. *Acc. Chem. Res.* 35:159–166.
- Clausen-Schaumann, H., M. Rief, C. Tolksdorf, and H. E. Gaub. 2000. Mechanical stability of single DNA molecules. *Biophys. J.* 78:1997–2007.
- Williams, M. C., J. R. Wenner, I. Rouzina, and V. A. Bloomfield. 2001. Entropy and heat capacity of DNA melting from temperature dependence of single molecule stretching. *Biophys. J.* 80:1932–1939.
- Williams, M. C., J. R. Wenner, I. Rouzina, and V. A. Bloomfield. 2001. Effect of pH on the overstretching transition of double-stranded DNA: evidence of force-induced DNA melting. *Biophys. J.* 80:874–881.
- Wenner, J. R., M. C. Williams, I. Rouzina, and V. A. Bloomfield. 2002. Salt dependence of the elasticity and overstretching transition of single DNA molecules. *Biophys. J.* 82:3160–3169.
- Strunz, T., K. Oroszlan, R. Schäfer, and H. J. Güntherodt. 1999. Dynamic force spectroscopy of single DNA molecules. *Proc. Natl. Acad. Sci. USA*. 96:11277–11282.
- Pope, L. H., M. C. Davies, C. A. Laughton, C. J. Roberts, S. J. Tendler, and P. M. Williams. 2001. Force-induced melting of a short DNA double helix. *Eur. Biophys. J.* 30:53–62.
- Bell, G. I. 1978. Models for specific adhesion of cells to cells. *Science*. 200:618–627.
- Evans, E., and K. Ritchie. 1999. Strength of a weak bond connecting flexible polymer chains. *Biophys. J.* 76:2439–2447.
- Kühner, F., J. Morfill, R. A. Neher, K. Blank, and H. E. Gaub. 2007. Force-induced DNA slippage. *Biophys. J.* 92:2491–2497.

26. Neuert, G., C. Albrecht, E. Pamir, and H. E. Gaub. 2006. Dynamic force spectroscopy of the digoxigenin-antibody complex. *FEBS Lett.* 580:505–509.
27. Blank, K., J. Morfill, and H. E. Gaub. 2006. Site-specific immobilization of genetically engineered variants of *Candida Antarctica* lipase B. *ChemBioChem.* 7:1349–1351.
28. Butt, H. J., and M. Jaschke. 1995. Calculation of thermal noise in atomic-force microscopy. *Nanotechnology.* 6:1–7.
29. Hugel, T., and M. Seitz. 2001. The study of molecular interactions by AFM force spectroscopy. *Macromol. Rapid Commun.* 22:989–1016.
30. Friedsam, C., A. K. Wehle, F. Kühner, and H. E. Gaub. 2003. Dynamic single-molecule force spectroscopy: bond rupture analysis with variable spacer length. *J. Phys. Condens. Matter.* 15:S1709–S1723.
31. Oesterhelt, F., M. Rief, and H. E. Gaub. 1999. Single molecule force spectroscopy by AFM indicates helical structure of poly(ethylene-glycol) in water. *N. J. Phys.* 1:1–11.
32. Kühner, F., and H. E. Gaub. 2006. Modelling cantilever-based force spectroscopy with polymers. *Polym.* 47:2555–2563.
33. Neher, R. A., and U. Gerland. 2004. Dynamics of force-induced DNA slippage. *Phys. Rev. Lett.* 93:198102.
34. Kühner, F., L. T. Costa, P. M. Bisch, S. Thalhammer, W. M. Heckl, and H. E. Gaub. 2004. LexA-DNA bond strength by single molecule force spectroscopy. *Biophys. J.* 87:2683–2690.
35. Reference deleted in proof.
36. Kühner, F., M. Erdmann, L. Sonnenberg, A. Serr, J. Morfill, and H. E. Gaub. 2006. Friction of single polymers at surfaces. *Langmuir.* 22: 11180–11186.
37. Kühner, F., M. Erdmann, and H. E. Gaub. 2006. Scaling exponent and Kuhn length of pinned polymers by single molecule force spectroscopy. *Phys. Rev. Lett.* 97:218301.
38. Liphardt, J., S. Dumont, S. B. Smith, I. Tinoco, and C. Bustamante. 2002. Equilibrium information from nonequilibrium measurements in an experimental test of Jarzynski's equality. *Science.* 296:1832–1835.
39. Albrecht, C., K. Blank, M. Lalic-Multhaler, S. Hirler, T. Mai, I. Gilbert, S. Schiffmann, T. Bayer, H. Clausen-Schaumann, and H. E. Gaub. 2003. DNA: a programmable force sensor. *Science.* 301:367–370.
40. Krautbauer, R., H. Clausen-Schaumann, and H. E. Gaub. 2000. Cisplatin changes the mechanics of single DNA molecules. *Angew. Chem. Int. Ed. Engl.* 39:3912–3915.
41. Baraldi, P. G., A. Bovero, F. Fruttarolo, D. Preti, M. A. Tabrizi, M. G. Pavani, and R. Romagnoli. 2004. DNA minor groove binders as potential antitumor and antimicrobial agents. *Med. Res. Rev.* 24:475–528.
42. Reddy, B. S., S. K. Sharma, and J. W. Lown. 2001. Recent developments in sequence selective minor groove DNA effectors. *Curr. Med. Chem.* 8:475–508.

## **P5**

### **8.5 Force induced DNA slippage**

F. Kühner, J. Morfill, R. A. Neher, K. Blank and H. E. Gaub

*Biophysical Journal (2007) 92: 2491-2497*

## Force-Induced DNA Slippage

Ferdinand Kühner,\* Julia Morfill,\* Richard A. Neher,<sup>†</sup> Kerstin Blank,\* and Hermann E. Gaub\*

\*Chair for Applied Physics and Center for NanoScience, and <sup>†</sup>Arnold Sommerfeld Center for Theoretical Physics and Center for Nanoscience, Ludwig-Maximilians Universität München, Munich, Germany

**ABSTRACT** DNA containing repetitive sequences displays richer dynamics than heterogeneous sequences. In the genome the number of repeat units of repetitive sequences, known as microsatellites, may vary during replication by DNA slippage and their expansion gives rise to serious disorders. We studied the mechanical properties of repetitive DNA using dynamic force spectroscopy and found striking differences compared with ordinary heterogeneous sequences. Repetitive sequences dissociate at lower forces and elongate above a certain threshold force. This yield force was found to be rate dependent. Following the rapid stretching of the DNA duplex, the applied force relaxes by stepwise elongation of this duplex. Conversely, contraction of the DNA duplex can be observed at low forces. The stepwise elongation and shortening is initiated by single slippage events, and single-molecule experiments might help to explain the molecular mechanisms of microsatellites formation. In addition to the biological importance, the remarkable properties of repetitive DNA can be useful for different nanomechanical applications.

### INTRODUCTION

Not only is DNA the key molecule for life, it has also become an extremely versatile tool kit for man made nanoscale structures and devices (1). Despite the fact that structure and dynamics of DNA were studied extensively, many of the discovered intramolecular processes, which exhibit complex dynamics and a distinct biological function, still lack satisfactory explanation. Microsatellites formation and bulge loop propagation in repetitive sequences are prominent examples (2). Two complementary DNA strands with heterogeneous sequences can only bind in a well-defined, unique conformation. Thermodynamic fluctuations lead to excitations in the double-stranded DNA, which results in a fast opening and closing of short stretches of basepairs (3,4). These fluctuations are localized and do not propagate through the DNA duplex.

In contrast, double-stranded DNA, containing short repetitive sequences, so-called microsatellites, displays a more complex dynamic behavior (5–9) with potential applications in nanotechnology. Two complementary strands can hybridize in various different conformations in which sufficiently long stretches are aligned to build up thermodynamically stable structures. Rapid transitions between these different conformations may occur. This so-called bulge loop formation and propagation (see Fig. 1) is called DNA slippage. It is considered to play a central role in the evolution of microsatellites, which can be found throughout the genome (10).

The repeat units of these microsatellites usually consist of one to six bases, e.g., (A)<sub>N</sub>, (GT)<sub>N</sub>, or (GTT)<sub>N</sub>. The corresponding length of the microsatellites, i.e., the number of consecutive identical repeat units, *N*, changes rapidly in evolution, presumably due to DNA slippage events during

replication. Because of this length variability, the microsatellites frequently are used as genetic markers, e.g., for forensic purposes, or to determine the genetic similarity between different populations. On the other hand, certain human neurodegenerative diseases, such as fragile X or Chorea Huntington, are related to expansions of trinucleotide repeats of microsatellites beyond certain thresholds (11).

Investigations of DNA slippage in vitro (2,12) showed that DNA bulge loop formation at the end of the duplex occurs on a timescale of microseconds. As a result, the two strands can be shifted relative to each other by propagation of a bulge loop toward the other end of the duplex (compare Fig. 1). In recent years, single molecule techniques have been used to study the mechanical properties of single DNA molecules. For example, the elasticity (13–16) and unzipping of λ-phage DNA (17,18), the interactions between proteins and double-stranded DNA (19,20) and the dissociation forces of short DNA duplexes (21–23) have been measured using different experimental setups. Recently, a theoretical work suggested studying DNA slippage with an atomic force microscope (AFM) (24): The two complementary strands of a DNA duplex with a repetitive sequence are predicted to move relative to each other if the externally applied force exceeds a critical force, the slipping threshold *f<sub>c</sub>*. This slipping threshold can be estimated by balancing the work performed by the external force with the binding free energy, which is lost if both strands are shifted relative to each other by one repeat unit. When shifting the two strands, the contour length of the single-stranded parts of the duplex elongates by twice the length of one repeat, whereas the double-stranded part shortens by one repeat unit. This simple argument leads to the slipping threshold *f<sub>c</sub>*:

$$f_c = \frac{\epsilon_b}{2l_s - l_d}, \quad (1)$$

Submitted August 24, 2006, and accepted for publication December 1, 2006.

Address reprint requests to Ferdinand Kühner, E-mail: ferdinand.kuehner@physik.uni-muenchen.de.

© 2007 by the Biophysical Society

0006-3495/07/04/2491/07 \$2.00

doi: 10.1529/biophysj.106.095836



In all experiments the slide was approached with the tip of the cantilever, allowing the two single strands to hybridize and form a duplex. To avoid double rupture events the binding probability was adjusted to  $<30\%$  by the applied force and duration time on the surface. Subsequently, the cantilever was retracted and the DNA duplex was loaded with a gradually increasing force until it finally ruptured and the cantilever relaxed back into its equilibrium position. The force applied to the DNA duplex via the PEG spacers was recorded as a function of the distance between the cantilever tip and the surface (Fig. 2). This curve was fitted with a two-state freely jointed chain (FJC) model, which describes the enthalpic and entropic behavior of polymers under an applied force (27).

Because most biologically relevant interactions are comparable in strength to thermal energies, force-induced processes such as the separation of receptor-ligand systems or in our case DNA duplexes are fluctuation-assisted processes (28). Therefore the distribution of the unbinding forces is broadened significantly (29). At a given force rate and at a fixed bond energy, a shift of the histograms directly reflects the difference in the effective width of the binding potentials (30,31) and indicates different unbinding pathways in the energy landscape.

To investigate, whether DNA duplexes with repetitive sequences have different unbinding pathways and therefore show different unbinding forces than heterogeneous sequences, both systems were analyzed. Fig. 3 shows the resulting distributions of the rupture forces of a heterogeneous ( $X$ )<sub>30</sub> and a repetitive DNA sequence ( $GT$ )<sub>15</sub> recorded at approximately the same pulling speed. Although both sequences have similar thermodynamic properties, which mainly correlate with the GC content of the sequence, their rupture force distributions differ drastically. The histogram for the repetitive DNA sequence (blue) is shifted toward lower dissociation forces. The DNA complex typically dissociates at forces below 40 pN. We conclude that an

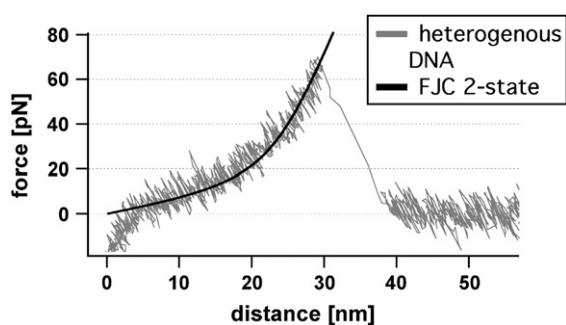


FIGURE 2 Example of a force-extension curve of a heterogeneous DNA duplex. While retracting the cantilever from the surface the polymer spacer and the DNA duplex are set under stress. The elastic behavior of the polymer-DNA duplex can be described with the FJC fit (black dashed line). At a force of 62 pN the double-stranded DNA dissociates and the cantilever drops back into its relaxed state.

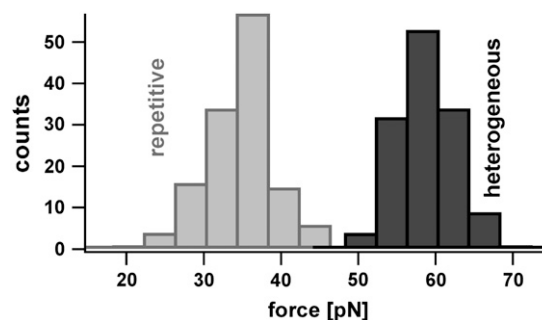


FIGURE 3 Histograms of the unbinding forces of DNA duplexes with a heterogeneous ( $X$ )<sub>30</sub> and a repetitive ( $GT$ )<sub>15</sub> sequence measured at similar pulling speeds. The duplex with the repetitive sequence dissociates at markedly lower forces, although its binding energy equals the binding energy of the heterogeneous sequence. The force distribution of the repetitive DNA is detruncated at a force of 40 pN. This gives evidence for an additional unbinding path, which is favored if an external force is applied.

additional dissociation path is available for the repetitive sequence. Note that the repetitive sequence might also bind fractionally and therefore might lead to lower dissociation forces. But without the assumption of an additional unbinding path this effect would lead to a broadening of the force distribution containing also higher forces similar to those of the heterogeneous sequence. The specificity of the measured interactions was proven, by replacing one single DNA strand with a noncomplementary sequence. This leads to  $<0.5\%$  interactions.

Having established that repetitive DNA has characteristics, which are absent in heterogeneous sequences, two repetitive sequences with a different number of bases per repeat unit were compared with a heterogeneous sequence. The study of the unbinding mechanism of ( $GTT$ )<sub>10</sub> and ( $GT$ )<sub>15</sub> should reveal more detailed insights in the unbinding mechanism.

The theoretically predicted unbinding path represents a stepwise elongation of the repetitive DNA duplex by moving both strands against each other (see Fig. 1) as soon as the externally applied force exceeds a certain threshold (slipping threshold  $f_c$ ). Such an elongation can indeed be observed in the recorded force-extension curves. Fig. 4 shows several typical force-extension curves obtained for two different repetitive and one heterogeneous DNA sequence. The force-extension curves for repetitive DNA deviate from the FJC behavior at forces above 40 pN, whereas the curves for heterogeneous DNA follow the FJC fit up to much higher forces. Apparently, repetitive DNA gets elongated at a slipping threshold between 35 and 40 pN. In the following we will use the expression “slipping threshold” for the value of the applied force beyond which the DNA duplex starts to slip or creep.

Whereas the results described above show further proof that repetitive sequences slip under load, the following experiment was carried out to examine the dependence of the slipping process on the length of the elementary repeat unit

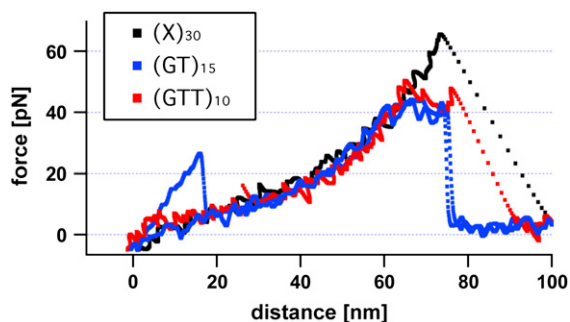


FIGURE 4 Typical force-extension curves of a heterogeneous  $(X)_{30}$ , a repetitive  $(GT)_{15}$ , and a  $(GTT)_{10}$  sequence. In contrast to the force-extension curve of the heterogeneous DNA sequence, which follows the two-state FJC behavior, the repetitive DNA duplexes elongate at a force (slipping threshold) of  $\sim 35$ – $40$  pN until they finally dissociate (rupture force).

and the number of repeats. These experiments were carried out with the following sequences:  $(GTT)_{10}$ ,  $(GT)_{10}$ , and  $(GT)_{15}$ . These DNA duplexes were probed at different pulling speeds because the slipping threshold is expected to be speed dependent. Because the slipping thresholds only differ by a few piconewtons, each data set was recorded with one cantilever to avoid calibration errors. In Fig. 5 the maxima of the slipping force distributions are plotted against the pulling speed of the cantilever. As can be seen in this figure, the slipping threshold shows a weaker dependence on the pulling speed for dinucleotide than for trinucleotide repeat units. Furthermore, the slipping thresholds are lower for the shorter repetitive sequence  $(GT)_{10}$  than for the sequence containing 15 repeat units. In a linear response, the velocity of a particle in a viscous environment is given by the product, containing the mobility of the particle and the applied force. Close to the slipping threshold  $f_c$ , the relationship between the measured force and the velocity of DNA slippage can be treated similarly. Here an effective friction for relative strand motion

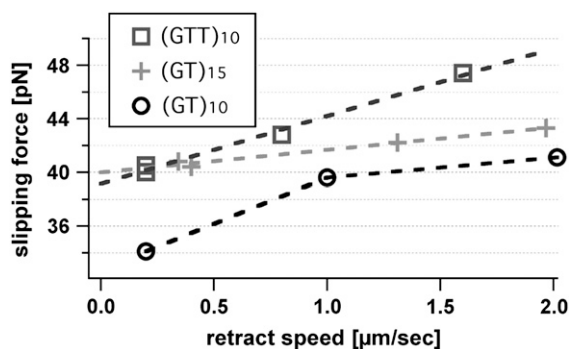


FIGURE 5 Pulling speed dependence of the slipping threshold for different repetitive DNA sequences. To avoid spring calibration errors every data set for one sequence is performed in a single experiment with the same cantilever. The maxima of the slipping threshold histograms, containing 80–150 force curves, are plotted against the pulling speed of the cantilever. The slipping threshold depends on the pulling speed and shows a linear time dependency as a first approximation.

arises from the need to nucleate bulge loops to shift both strands.

Close to slipping threshold  $f_c$  the slipping velocity  $v(f)$  increases linearly with the measured force due to  $v(f) = dv/df \times (f - f_c)$ . The variable  $u_0 = dv/df$  represents the effective slipping mobility, which depends on the bulge loop nucleation rate, microscopic slipping rate, and the number of repeat units. In our experiments, we correlated the slipping velocity  $v(f)$  with the retract speed of the cantilever and measured the resulting slipping threshold.

From a linear fit, we achieve a slipping mobility  $u_0$  of 580 nm/s·pN for a dinucleotide and 250 nm/s·pN for a trinucleotide sequence. This is in agreement with the theoretical predictions and with bulk experiments that observed faster expansions for shorter repeat units. To form a bulge loop in a dinucleotide sequence, fewer basepairs have to open up than in a trinucleotide sequence and hence the rate to create these defects is smaller for longer repeat units. However, the additional length increase per step for longer repeat units does not compensate the lower rate.

So far the experimental results confirm that repetitive DNA strands can slide against each other and that the slipping threshold can be determined for different retract speeds. The values obtained for the slipping mobility are in good agreement with theoretical predictions. However, the time resolution in an usual force-extension measurement is not sufficient enough to discriminate individual steps, which would give direct evidence of the stepwise microscopic sliding mechanism.

Initial force clamp (32) measurements (data not shown) performed with the AFM only showed a lengthening of the different DNA duplexes at forces of 35–40 pN, but failed to resolve the expected individual steps. Therefore, a new measurement protocol was implemented, whose time resolution is limited only by the relaxation of the cantilever. These measurements were carried out as follows: i), The cantilever was lowered, to allow the DNA to hybridize and form a duplex. ii), The cantilever was gradually retracted from the surface allowing a certain force, well below the slipping threshold, to build up. iii), Then, in one step, the cantilever was retracted an additional 3–7 nm away from the surface. As a result of this distance jump, the force acting on the DNA duplex rises almost instantaneously to a new higher value. Initially, the contour length, which gives the total length under force, does not change. If, in response, the DNA duplex elongates due to slipping, an increase of the contour length is observed. In addition, the applied force drops, which can be detected by the cantilever.

Fig. 6 A shows two typical curves, force versus time and distance versus time, for a 15-times repetitive dinucleotide DNA duplex  $(GT)_{15}$  recorded with the measurement protocol described above. First, the force acting on the DNA molecule is fluctuating around 38 pN, a value close to the previously observed slipping threshold. As indicated with the blue arrow in the force versus time graph a 4-nm distance

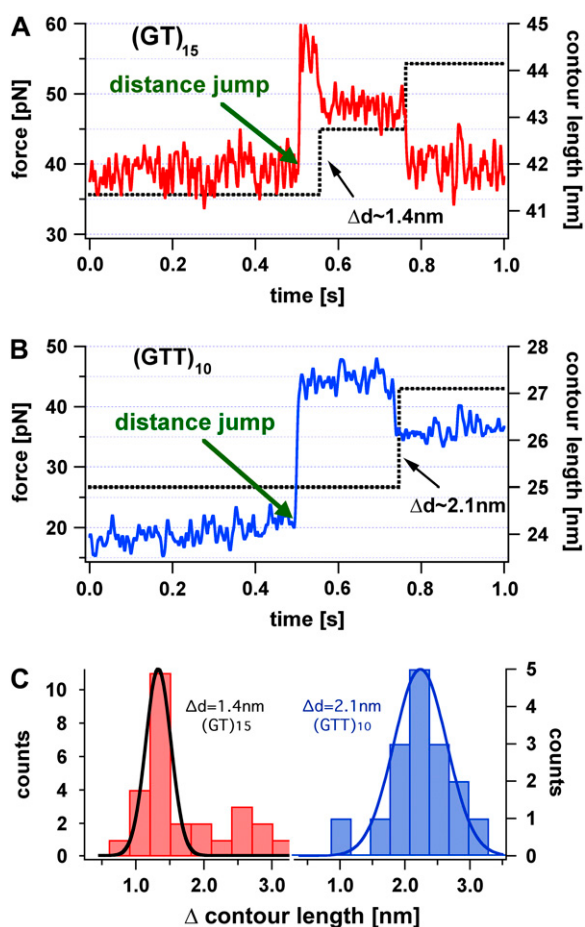


FIGURE 6 Force versus time (*red*) and contour length versus time curve (*black*) of a repetitive (GT)<sub>15</sub> and (GTT)<sub>10</sub> DNA duplex, initially held at a force below the slipping threshold. After 0.5 s a distance jump of the cantilever was performed resulting in a force step above the slipping threshold, but leaving the contour length of the molecule constant. In panel A the contour length of the (GT)<sub>15</sub> DNA complex relaxes in two discrete elongation steps and the force acting on the duplex drops below the slipping threshold. In panel B the contour length (*black curve*) of the (GTT)<sub>10</sub> DNA complex elongates in one discrete step and the force drops below the slipping threshold. Panel C shows the distribution of the contour length change for the di- and trinucleotide sequence. The additional peak at ( $\sim 2.8$  nm) in the dinucleotide sequence may occur from double slipping events.

jump was performed. As a result of the distance jump the force (*red*) increases to nearly 57 pN, but the contour length stays constant. Within a fraction of a second the measured force decreases to a value below 40 pN in discrete steps. The final force is again close to the observed slipping threshold. This rapid and discrete decrease of the force can only be explained with a stepwise lengthening of the DNA molecule, which compensates the performed distance jump. These observations show that a single relaxation process increases the contour length of the dinucleotide DNA system by  $\sim 1.4 \pm 0.3$  nm. This value was obtained by a Gaussian fit of the contour length increase histogram (see Fig. 6 C) of several experiments, with a confidence interval of 90% certainty. This effect can be well explained by a relative sliding of one

repeat unit ( $dl = 2l_s - l_d = 4 \times 0.5 \text{ nm} - 2 \times 0.34 \text{ nm} = 1.4 \text{ nm}$ ). Unfortunately, only a limited number of steps can be observed, because the probability of holding these DNA duplexes under such a high force for a long time is very low and decreases further with every step.

Fig. 6 B shows the equivalent experiment for a trinucleotide (GTT)<sub>10</sub> sequence. As expected, the contour length increase of  $\sim 2.1 \pm 0.3$  nm, determined analogous to the (GT) sequence, is higher than for the dinucleotide sequence. Analogous experiments performed with the heterogeneous sequence did not show any discrete steps (data not shown).

To exclude the possibility, that the observed steps are artifacts of multiple binding the following arguments are pointed out. First of all the overall elasticity of the measured PEG polymer spacer would be much stiffer. Secondly, the presumption of three bound molecules in parallel mimicking the three steps of the single molecule shown in Fig. 5 would require the respective PEG polymer spacers to differ in length by  $< 2$  nm. This would mean that the total force acting on the cantilever would be distributed on three duplexes and as a consequence the lifetime for the duplexes would be much longer than our experimental findings. Dissociation of one duplex increases the split force applied to the remaining duplexes and reduces their lifetime drastically. For this reason multiple binding as potential artifact can be excluded with a very high certainty.

Having shown that all characteristic parameters describing the slipping process can be determined experimentally, we wanted to obtain more detailed information about the behavior near the slipping threshold. The system for the native and elongated conformation of the repetitive DNA duplex can be described with a two-state potential illustrated in Fig. 7. Application of an external force allows the tuning of the potential, so that the Gibbs free energy of these two states is the same as shown with the dashed line in Fig. 7. If this force equals the slipping threshold  $f_c$  the system can fluctuate in equilibrium. This was achieved in the measurement shown in Fig. 8. Using the above-mentioned measurement protocol a distance jump is performed and the force on the DNA duplex first increases over the slipping threshold limit  $f_c$ . As a result the DNA duplex elongates and the force drops to the slipping threshold. At this force the system starts to perform multiple back and forth slipping events. An additional distance jump forces the DNA duplex in its elongated conformation until it finally ruptures completely.

These fluctuations of the DNA duplex between the two states can be analyzed with random telegraph noise analysis similar to ion channel recordings (Fig. 8, *black curve*). The hidden Markovian process can be characterized with the transition rates from one state to the other (33). The data trace shown in Fig. 8 exhibits mean lifetimes of 0.031 s for the elongated and 0.022 s for the shortened state. Note that these lifetimes are very dependent on the applied force. The energy difference between these two states varies between the binding energy of the DNA duplex and the bending energy

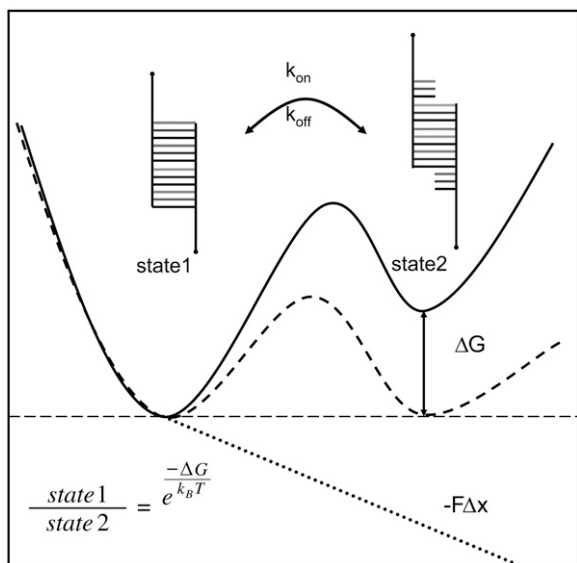


FIGURE 7 Gibbs free energy of a two-state system under an external force. The model describes the completely bound and the first lengthened state of a repetitive DNA duplex. The potential is tilted due to an externally applied force. This results in a leveling of the energy of the two states, allowing the DNA duplex to fluctuate between the two states in equilibrium.

of the cantilever. The energy was found to be  $\sim 7 k_B T$ , which is close to well-established values of about  $\sim 8 k_B T$  for a trinucleotide GTT repeat unit. Other experiments underline this value. Due to the sensitivity of the system regarding the applied force and the low detection probability a closer examination will require substantial instrumental improvements. The observed multiple forward and backward jumps in Fig. 8 could be detected with short polymer spacers with lengths between 15 and 20 nm only. A possible reason for this finding could be that the fluctuations of the cantilever allow the duplex to form a bulge loop at lower forces, which eventually diffuses to the other end. For longer spacers these

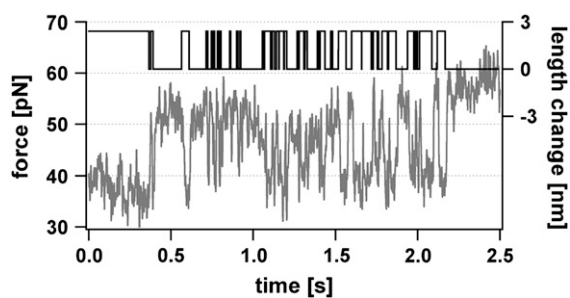


FIGURE 8 Example for the slipping of the DNA duplex between the elongated and the short state. A repetitive  $(GTT)_{10}$  DNA duplex is held at a constant force analogous to Fig. 6. A distance jump drives the force above the slipping threshold. This results in a lengthening of the DNA duplex and the force drops down to the slipping threshold. Consequently, the duplex lengthens and shortens due to forward and backward slipping. The measured time trace (red) of the fluctuation process was analyzed with a telegraph noise algorithm to extract the dynamics of the length changes (black). The mean lifetimes were found to be 0.031 s for the fully hybridized state and 0.022 s for the lengthened state.

fluctuations are averaged by the elasticity of the polymer (34). The alternative scenario, that the observed shortening is a simple transient bulge loop formation at the stretched end, can be ruled out because the lifetime of these bulge loops, even if they travel some steps into the molecule, is orders of magnitude too small to explain the observed frequencies.

## DISCUSSION

The data presented here show that repetitive DNA duplexes elongate under an applied shear force and dissociate at significantly lower forces of  $\sim 38$  pN than for heterogeneous DNA sequences. Because of the possibility of fractional binding for repetitive sequences, lower dissociation forces are possible in regular force distance curves (see Fig. 2). This is due to an additional unbinding path that allows the repetitive DNA duplex to increase its contour length without having to overcome a large free energy barrier. It should be pointed out that this unbinding path energetically is not favored over other paths but gets populated by force.

The theoretically predicted length increase occurs in discrete slipping steps. We could show that the resulting length increase of the whole DNA duplex is consistent with the length increase obtained by shifting both strands of di- and trinucleotide sequences by one repeat unit. Slippage is faster for shorter repeat units and smaller repeat numbers. This is consistent with the theory of bulge loop diffusion because the expected slipping velocity decreases with the energy needed to produce a bulge loop. In addition, the diffusion of a bulge loop through the molecule is faster for shorter duplexes. The mechanism of relative strand motion caused by the creation, diffusion, and absorption of bulge loop defects is similar to defect propagation in crystal lattices.

The slipping threshold determined in the measurements was found to be larger than the theoretically predicted slipping threshold  $f_c$ . This may be due to the small number of repeat units used in the experiments and to the simplistic model used for the theory. For instance, deformations and conformational changes in the backbone of the DNA duplex resulting from an externally applied force are not included in the model.

The slipping velocity is expected to scale inversely with the number of repeat units. This prediction could not be unambiguously confirmed because only rather short sequences were available. Further experiments are necessary to quantify the dependence of the slipping dynamics on the repeat number and flanking sequences. More detailed experiments will shed some light on the kinetics of the processes involved in expansion of microsatellites during replication. Because of its bidirectional property DNA slippage, itself, is not the cause for the asymmetric increase effect of repeat units in the human genome.

Besides the biological importance of repetitive sequences, the remarkable properties of repetitive DNA might also be useful for different nanomechanical applications (35–37). Because the rupture force distribution for repetitive

sequences is truncated sharply at forces close to 40 pN, repetitive DNA could serve as a programmable force sensor, with a threshold force that can be fine tuned by sequence composition. Adjustable viscoelastic building blocks in DNA self-assembly structures can be realized with repetitive sequences.

Furthermore, the relaxation of a large force to a slipping threshold force  $f_c$  with a time constant that can be chosen by length and sequence composition could be used as a length independent force normal. Conversely, if extended, repetitive double-stranded DNA contracts until the slipping threshold force  $f_c$  is built up if the initial force is below  $f_c$ . Therefore, complementary repetitive single-stranded DNA could be applied for self-tightening connections in nanostructures. After initial hybridization, two single strands tend to maximize their overlap, i.e., the number of basepairs, until a tension of the order of the slipping threshold  $f_c$  is built up. These adjustable force-induced tensions at confident locations establish completely new features in nanoscale structures.

We thank Ulrich Gerland and Stefan Thalhammer for helpful discussions and Steffen Mihatsch for help with the data analysis.

This study was supported by the German Science Foundation DFG and by the Fond der Chemischen Industrie.

## REFERENCES

- Seeman, N. C. 2003. DNA in a material world. *Nature*. 421:427–431.
- Schlotterer, C., and D. Tautz. 1992. Slippage synthesis of simple sequence DNA. *Nucleic Acids Res.* 20:211–215.
- Altan-Bonnet, G., A. Libchaber, and O. Krichevsky. 2003. Bubble dynamics in double-stranded DNA. *Phys. Rev. Lett.* 90:138101.
- Neher, R. A., and U. Gerland. 2006. Intermediate phase in DNA melting. *Phys. Rev. E.* 73:030902.
- Lyer, R. R., A. Pluciennik, V. Burdett, and P. L. Modrich. 2006. DNA mismatch repair: functions and mechanisms. *Chem. Rev.* 106:302–323.
- Heidenfelder, B. L., A. M. Makhov, and M. D. Topal. 2003. Hairpin formation in Friedreich's ataxia triplet repeat expansion. *J. Biol. Chem.* 278:2425–2431.
- Karthikeyan, G., K. V. R. Chary, and B. J. Rao. 1999. Fold-back structures at the distal end influence DNA slippage at the proximal end during mononucleotide repeat expansions. *Nucleic Acids Res.* 27:3851–3858.
- Levinson, G., and G. A. Gutman. 1987. Slipped-strand mispairing: a major mechanism for DNA-sequence evolution. *Mol. Biol. Evol.* 4:203–221.
- Trinh, T. Q., and R. R. Sinden. 1991. Preferential DNA secondary structure mutagenesis in the lagging strand of replication in *Escherichia coli*. *Nature*. 352:544–547.
- Li, Y. C., A. B. Korol, T. Fahima, and E. Nevo. 2004. Microsatellites within genes: structure, function, and evolution. *Mol. Biol. Evol.* 21:991–1007.
- Schlotterer, C. 2000. Evolutionary dynamics of microsatellite DNA. *Chromosoma*. 109:365–371.
- Porschke, D. 1974. Model calculations on the kinetics of oligonucleotide double helix coil transitions. Evidence for a fast chain sliding reaction. *Biophys. Chem.* 2:83–96.
- Smith, S. B., Y. J. Cui, and C. Bustamante. 1996. Overstretching B-DNA: the elastic response of individual double-stranded and single-stranded DNA molecules. *Science*. 271:795–799.
- Perkins, T. T., S. R. Quake, D. E. Smith, and S. Chu. 1994. Relaxation of a single DNA molecule observed by optical microscopy. *Science*. 264:822–826.
- Rief, M., H. Clausen-Schaumann, and H. E. Gaub. 1999. Sequence-dependent mechanics of single DNA molecules. *Nat. Struct. Biol.* 6:346–349.
- Cui, S., C. Albrecht, F. Kühner, and H. E. Gaub. 2006. Weakly bound water molecules shorten single-stranded DNA. *J. Am. Chem. Soc.* 128:6636–6639.
- EssevazRoulet, B., U. Bockelmann, and F. Heslot. 1997. Mechanical separation of the complementary strands of DNA. *Proc. Natl. Acad. Sci. USA*. 94:11935–11940.
- Lubensky, D. K., and D. R. Nelson. 2002. Single molecule statistics and the polynucleotide unzipping transition. *Phys. Rev. E.* 65:031917.
- Friedsam, C., A. K. Wehle, F. Kühner, and H. E. Gaub. 2003. Dynamic single-molecule force spectroscopy: bond rupture analysis with variable spacer length. *J. Phys. Condens. Matter*. 15:S1709–S1723.
- Kühner, F., L. T. Costa, P. M. Bisch, S. Thalhammer, W. M. Heckl, and H. E. Gaub. 2004. LexA-DNA bond strength by single molecule force spectroscopy. *Biophys. J.* 87:2683–2690.
- Krautbauer, R., M. Rief, and H. E. Gaub. 2003. Unzipping DNA oligomers. *Nano Lett.* 3:493–496.
- Strunz, T., K. Oroszlan, R. Schafer, and H. J. Guntherodt. 1999. Dynamic force spectroscopy of single DNA molecules. *Proc. Natl. Acad. Sci. USA*. 96:11277–11282.
- Kühner, F., M. Erdmann, L. Sonnenberg, A. Serr, J. Morfill, and H. E. Gaub. 2006. Friction of single polymers at surfaces. *Langmuir*. 22:11180–11186.
- Neher, R. A., and U. Gerland. 2004. Dynamics of force-induced DNA slippage. *Phys. Rev. Lett.* 93:198102.
- Neuert, G., C. Albrecht, E. Pamir, and H. E. Gaub. 2006. Dynamic force spectroscopy of the digoxigenin-antibody complex. *FEBS Lett.* 580:505–509.
- Blank, K., J. Morfill, and H. E. Gaub. 2006. Site-specific immobilization of genetically engineered variants of Candida Antarctica Lipase B. *American Chemical Society*. 7:1349–1351.
- Oesterhelt, F., M. Rief, and H. E. Gaub. 1999. Single molecule force spectroscopy by AFM indicates helical structure of poly(ethylene-glycol) in water. *New J. Phys.* 1:6.
- Evans, E., and K. Ritchie. 1997. Dynamic strength of molecular adhesion bonds. *Biophys. J.* 72:1541–1555.
- Friedsam, C., A. K. Wehle, uuml, F. hner, and H. E. Gaub. 2003. Dynamic single-molecule force spectroscopy: bond rupture analysis with variable spacer length. *J. Phys. Condens. Matter*. S1709–S1723.
- Evans, E. 2001. Probing the relation between force-lifetime and chemistry in single molecular bonds. *Annu. Rev. Biophys. Biomol. Struct.* 30:105–128.
- Heymann, B., and H. Grubmuller. 2000. Dynamic force spectroscopy of molecular adhesion bonds. *Phys. Rev. Lett.* 84:6126–6129.
- Oberhauser, A. F., P. K. Hansma, M. Carrion-Vazquez, and J. M. Fernandez. 2001. Stepwise unfolding of titin under force-clamp atomic force microscopy. *Proc. Natl. Acad. Sci. USA*. 98:468–472.
- Venkataramanan, L., and F. J. Sigworth. 2002. Applying hidden Markov models to the analysis of single ion channel activity. *Biophys. J.* 82:1930–1942.
- Kühner, F., and H. Gaub. 2006. Modelling cantilever based force spectroscopy with polymers. *Polym.* 47:2555–2563.
- Neher, R. A., and U. Gerland. 2005. DNA as a programmable viscoelastic nanoelement. *Biophys. J.* 89:3846–3855.
- Albrecht, C., K. Blank, M. Lalic-Multhaler, S. Hirler, T. Mai, I. Gilbert, S. Schiffmann, T. Bayer, H. Clausen-Schaumann, and H. E. Gaub. 2003. DNA: a programmable force sensor. *Science*. 301:367–370.
- Simmel, F. C., and W. U. Dittmer. 2005. DNA nanodevices. *Small*. 1:284–299.

## **P6**

### **8.6 Site-Specific Immobilization of Genetically Engineered Variants of *Candida Antarctica* Lipase B**

K. Blank, J. Morfill and H. E. Gaub

*ChemBioChem* (2006) 7: 1349-1351

DOI: 10.1002/cbic.200600198

## Site-Specific Immobilization of Genetically Engineered Variants of *Candida antarctica* Lipase B

Kerstin Blank, Julia Morfill, and Hermann E. Gaub<sup>\*[a]</sup>

The immobilization of proteins on solid surfaces has been a topic of intensive research for many years. Numerous methods have been developed to immobilize proteins for bioseparation, biosensors, diagnostic tests and single-molecule experiments.<sup>[1]</sup> With the growing need for miniaturization and parallelization, new methods are needed for the immobilization of proteins with high functional density and specificity.<sup>[2,3]</sup> Most of the methods used so far do not allow the covalent immobilization of a protein at a well-defined position. In this study, cysteines, introduced by genetic engineering, have been used for site-specific immobilization of a model enzyme to a glass surface by means of a heterobifunctional poly(ethylene glycol) (PEG) spacer.<sup>[4]</sup> While PEG is used for a broad range of applications to render surfaces protein resistant,<sup>[5–7]</sup> only a few reports describe its use as a linker for attaching proteins to surfaces.<sup>[8–13]</sup> However, the use of a heterobifunctional PEG spacer would provide a protein-resistant surface displaying reactive groups for the covalent attachment of proteins in a controlled manner. In addition, the coupling of PEG to proteins has been shown to increase the stability of the protein and maintain it in an active conformation.<sup>[14]</sup>

To evaluate the usefulness of this concept, *Candida antarctica* lipase B (CalB; EC 3.1.1.3) was used as a model enzyme.<sup>[15]</sup> CalB is an industrially important lipase that is used for various applications in bioorganic synthesis.<sup>[16]</sup> It is a 35 kDa monomer with three disulfide bridges. CalB has been immobilized on surfaces for various applications, but these methods are mainly based on the adsorption of hydrophobic or charged amino acids to supports.<sup>[17]</sup> Site-specific immobilization of lipases would be advantageous because it has been shown that the properties of lipases depend on their orientation on a surface.<sup>[18]</sup> In this study, mutants of CalB have been prepared that display a free cysteine at a defined position on the molecule

(Figure 1). Based on recent results obtained for the expression of CalB in *Escherichia coli*,<sup>[19]</sup> one mutant has been produced that contains an additional cysteine at the C terminus of the protein after the His tag (CalB-HisGGC). The other mutant is based on the results of Velonia et al.<sup>[20]</sup> who were able to selectively reduce one disulfide bond (Cys293–Cys311) on the surface of the protein. In the following step, the reduced cysteines were used to couple the protein to polystyrene. Since there is no way to control which cysteine is reacting with the maleimide-functionalized polystyrene, another approach was performed in this study here: Cys311 was replaced by alanine (CalB-C311A-His) to leave only one free cysteine for coupling. In addition, an N-terminal FLAG tag was attached to the lipase variants for detection purposes.

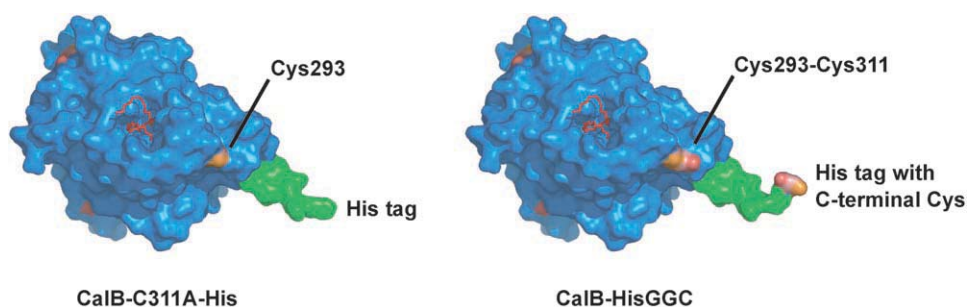


**Figure 1.** Mutants of the lipase CalB (PDB ID: 1LBT) possessing one free cysteine for the oriented coupling of the enzyme to surfaces. For CalB-C311A-His, one cysteine from a disulfide bridge on the surface of CalB was mutated to alanine. CalB-HisGGC contains an additional cysteine at the C terminus.

The mutants and an unmodified CalB containing a C-terminal His tag (CalB-His) were expressed in *E. coli* at 25 °C, as described previously.<sup>[19]</sup> The expression levels of the mutants were compared with the unmodified enzyme by Western blot analysis by using two different antibodies (Figure S1). The free cysteines reduce the yield of the functionally expressed lipase by approximately a factor of 10. This effect is known for the expression of other proteins containing free cysteines in the periplasm of *E. coli*.<sup>[21]</sup> The different lipase variants were purified from periplasmic extracts by using Ni<sup>2+</sup>-NTA columns. A washing step with 1 mM Tris(2-carboxyethyl)phosphine hydrochloride (TCEP) was included to remove all impurities that might have coupled to the free cysteine during expression and preparation of the cell extracts.<sup>[22]</sup> The eluted fraction was dialyzed against coupling buffer (50 mM sodium phosphate, pH 7.2, 50 mM NaCl and 10 mM EDTA) and concentrated afterwards. The purity was analyzed by using reducing and nonreducing SDS-PAGE (Figure S2). Pure enzymes can be obtained after just one chromatography step. The purification procedure yields a certain amount of dimers, which is dependent on the position of the free cysteine on the molecule. Finally, the activity of the variants was measured by using the substrate *para*-nitrophenol butyrate. The tests showed that neither the additional cysteine at the C terminus nor the mutated disulfide bridge has any significant influence on the specific activity and the kinetic constants of CalB (Table S1).

Before the CalB variants were coupled to the surface, the proteins were reduced by using TCEP beads in order to gener-

[a] K. Blank, J. Morfill, Prof. Dr. H. E. Gaub  
Lehrstuhl für Angewandte Physik and Center for Nanoscience  
LMU München  
Amalienstrasse 54, 80799 München (Germany)  
Fax: (+49) 89-2180-2050  
E-mail: hermann.gaub@physik.uni-muenchen.de

Supporting information for this article is available on the WWW under <http://www.chembiochem.org> or from the author.

ate free thiols. In parallel, amino-functionalized slides were incubated with borate buffer (pH 8.5). This step was necessary to deprotonate the amino groups for coupling to the *N*-hydroxy-succinimide groups (NHS) of the heterobifunctional NHS-PEG-maleimide ( $M_w = 3400 \text{ g mol}^{-1}$ ), which was used as spacer for the immobilization of the CalB variants. The PEG was dissolved at a concentration of 50 mM in borate buffer and incubated on the surface for 1 hour. After the surfaces had been washed with ultrapure water, the CalB variants were spotted on them. A sample containing a 10000-fold excess of free cysteine was spotted as a negative control. In addition, these spotting solutions were prepared with nonreduced enzyme variants. After the spotted protein solutions had been incubated on the surface for 1 hour, the density of the immobilized CalB variants was detected by using an anti-FLAG antibody. The activity of the immobilized lipase variants was tested by using agar plates containing Tween 80 and  $\text{CaCl}_2$ . The slide was put upside down on the agar plates and incubated on the plates overnight.

Both enzyme variants possessing the free cysteine could be immobilized to the maleimide-activated surfaces in an oriented and functional way (Figure 2). The binding of CalB-HisGGC and CalB-C311A-His is highly specific. No significant binding was detected for the negative controls: CalB-His without any free cysteine shows only very little binding to the surface, and the addition of free cysteine to the spotting solution blocks the binding of the enzyme variants very efficiently. The fact that only a very low signal is detected for CalB-His proves that the enzyme variants do not bind through the cysteines of the disulfide bridges, which might be reduced during incubation with the TCEP beads. The immobilization density of CalB-HisGGC is much higher than that of CalB-C311A-His. As the preparation of CalB-HisGGC contains a higher number of dimers, we conclude that the cysteine is much more accessible if it is located at the C terminus. In this case, the His tag serves as a spacer between the surface of the protein and the reactive cysteine. The image of the activity test with the Tween 80 plate shows an identical pattern. This corroborates the hypothesis that both enzyme variants are immobilized on a surface in an active conformation.

The use of PEG as a spacer for the oriented and covalent immobilization of proteins to surfaces yields very good ratios of specific to nonspecific binding. This method can be applied to every material for which amino groups can be generated by silanization or other procedures. Here, we have used a lipase as a model system to prove the applicability of this procedure. The site-specific immobilization of CalB represents a good basis for the optimization of reaction conditions. Because each enzyme is immobilized in the same orientation it should display identical characteristics. In addition, this method may be used for many other biomolecules such as oligonucleotides, peptides and other proteins. If the introduction of a cysteine is not possible by genetic engineering, then thiol groups can be introduced by chemical modification.<sup>[23]</sup> However, the attachment of a cysteine to the C terminus of a protein is a very general strategy that can be employed for a variety of different proteins. An expression vector can be constructed that con-

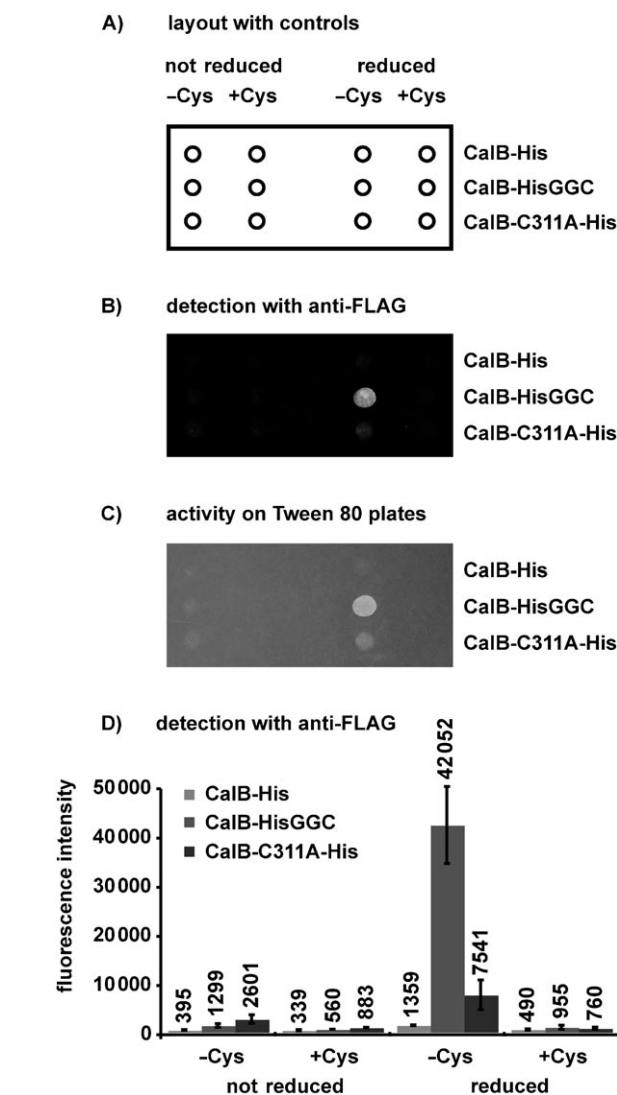


**Figure 2.** A) Schematic of the position of the different spots on the slide. Each enzyme variant was spotted with or without reduction and in a buffer with or without an excess of free cysteine. B) Fluorescence scan of the bound anti-FLAG antibody showing the density of the enzyme variants on the surface. C) Photograph of the Tween 80 agar plate showing the activity of the enzyme variants on the surface. D) Summary of the immobilization density detected with the anti-FLAG antibody (mean of three different slides).

tains the sequence of the His tag, the two glycines and the cysteine, thus allowing convenient cloning of the proteins of interest. Therefore, as no modification of the protein itself is necessary, the strategy is particularly useful if many different proteins need to be immobilized in parallel.

## Acknowledgements

The authors thank Novozymes A/S for the gift of the calB gene, A. Plückthun for pAK400, K. Gottschalk for the help in preparing the figures and E. Puchner, H. Gump, T. Nicolaus, M. Skjot, A. Svendsen, N. Hatzakis and A. E. Rowan for helpful discussions.

This work was supported by the European Union and the Deutsche Forschungsgemeinschaft.

**Keywords:** CalB · immobilization · poly(ethylene glycol) · protein engineering · surface chemistry

- [1] L. Cao, *Carrier-Bound Immobilized Enzymes*, Wiley-VCH, Weinheim, **2005**.
- [2] K. Y. Tomizaki, K. Usui, H. Mihara, *ChemBioChem* **2005**, *6*, 782–799.
- [3] I. Sielaff, A. Arnold, G. Godin, S. Tugulu, H. A. Klok, K. Johnsson, *ChemBioChem* **2006**, *7*, 194–202.
- [4] M. J. Roberts, M. D. Bentley, J. M. Harris, *Adv. Drug Delivery Rev.* **2002**, *54*, 459–476.
- [5] S. I. Jeon, J. H. Lee, J. D. Andrade, P. G. Degennes, *J. Colloid Interface Sci.* **1991**, *142*, 149–158.
- [6] "Poly(ethylene glycol) Chemistry and Biological Applications", S. J. Sofia, E. W. Merrill, *ACS Symp. Ser.* **1997**, *680*, 342–360.
- [7] N. A. Alcantar, E. S. Aydil, J. N. Israelachvili, *J. Biomed. Mater. Res.* **2000**, *51*, 343–351.
- [8] J. Piehler, A. Brecht, R. Valiokas, B. Liedberg, G. Gauglitz, *Biosens. Bioelectron.* **2000**, *15*, 473–481.
- [9] C. D. Hodneland, Y. S. Lee, D. H. Min, M. Mrksich, *Proc. Natl. Acad. Sci. USA* **2002**, *99*, 5048–5052.
- [10] C. Albrecht, K. Blank, M. Lalic-Mülthaler, S. Hirler, T. Mai, I. Gilbert, S. Schiffmann, T. Bayer, H. Clausen-Schaumann, H. E. Gaub, *Science* **2003**, *301*, 367–370.
- [11] K. Blank, T. Mai, I. Gilbert, S. Schiffmann, J. Rankl, R. Zivin, C. Tackney, T. Nicolaus, K. Spinnler, F. Oesterhelt, M. Benoit, H. Clausen-Schaumann, H. E. Gaub, *Proc. Natl. Acad. Sci. USA* **2003**, *100*, 11 356–11 360.
- [12] G. L. Zhen, V. Eggli, J. Voros, P. Zammaretti, M. Textor, R. Glockshuber, E. Kuennemann, *Langmuir* **2004**, *20*, 10 464–10 473.
- [13] G. Neuert, C. Albrecht, E. Pamir, H. E. Gaub, *FEBS Lett.* **2006**, *580*, 505–509.
- [14] L. Cao, *Curr. Opin. Chem. Biol.* **2005**, *9*, 217–226.
- [15] J. Uppenberg, N. Ohrner, M. Norin, K. Hult, G. J. Kleywegt, S. Patkar, V. Waagen, T. Anthonsen, T. A. Jones, *Biochemistry* **1995**, *34*, 16 838–16 851.
- [16] E. M. Anderson, K. M. Larsson, O. Kirk, *Biocatal. Biotransform.* **1998**, *16*, 181–204.
- [17] T. Nakaoki, Y. Mei, L. M. Miller, A. Kumar, B. Kalra, M. E. Miller, O. Kirk, M. Christensen, R. A. Gross, *Ind. Biotechnol.* **2005**, *1*, 126–134.
- [18] J. M. Palomo, G. Muñoz, G. Fernández-Lorente, C. Mateo, M. Fuentes, J. M. Guisan, R. Fernández-Lafuente, *J. Mol. Catal. B* **2003**, *21*, 201–210.
- [19] K. Blank, J. Morfill, H. Gump, H. E. Gaub, *J. Biotechnol.* **2006**, published on-line 19th May 2006.
- [20] K. Velonia, A. E. Rowan, R. J. M. Nolte, *J. Am. Chem. Soc.* **2002**, *124*, 4224–4225.
- [21] K. Blank, P. Lindner, B. Diefenbach, A. Plückthun, *Protein Expression Purif.* **2002**, *24*, 313–322.
- [22] E. M. K. Hedin, S. A. Patkar, J. Vind, A. Svendsen, K. Hult, P. Berglund, *Can. J. Chem.* **2002**, *80*, 529–539.
- [23] V. Grazu, O. Abian, C. Mateo, F. Batista-Viera, R. Fernández-Lafuente, J. M. Guisan, *Biotechnol. Bioeng.* **2005**, *90*, 597–605.

Received: May 9, 2006

Published online on July 26, 2006

## **P7**

### **8.7 Functional expression of *Candida antarctica* lipase B in *Escherichia coli***

K. Blank, J. Morfill, H. Gump and H. E. Gaub

*Journal of Biotechnology* (2006) 125: 474-483



## Functional expression of *Candida antarctica* lipase B in *Escherichia coli*

Kerstin Blank, Julia Morfill, Hermann Gumpp, Hermann E. Gaub\*

*Lehrstuhl für Angewandte Physik & Center for Nanoscience, LMU München, Amalienstrasse 54, 80799 München, Germany*

Received 6 November 2005; received in revised form 24 March 2006; accepted 4 April 2006

### Abstract

*Candida antarctica* lipase B (CalB) is an important catalyst in bio-organic synthesis. To optimize its performance, either the reaction medium is changed or the lipase itself is modified. In the latter case, mutants are generated in *Escherichia coli* and subsequently expressed in fungal hosts for their characterization. Here we present the functional expression of CalB in the periplasm of *E. coli*. By step-wise deletion of the CalB signal and propeptide we were able to express and purify two different variants of CalB (mature CalB and CalB with its propeptide). A N-terminal FLAG and a C-terminal His tag were used for the purification. For the substrates *para*-nitrophenol butyrate (*p*-NPB), *para*-nitrophenol laurate (*p*-NPL) and carboxyfluorescein diacetate (CFDA) the specific activity was shown to be similar to CalB expressed in *Aspergillus oryzae*. The kinetic constants  $k_M$ ,  $v_{max}$  and  $k_{cat}$  were determined using the substrates *p*-NPB and *p*-NPL. Almost identical  $k_{cat}/k_M$  values ( $0.423$ – $0.466 \text{ min}^{-1} \mu\text{M}^{-1}$  for *p*-NPB and  $0.068$ – $0.071 \text{ min}^{-1} \mu\text{M}^{-1}$  for *p*-NPL) were obtained for the CalB variants from *E. coli* and *A. oryzae*. The results clearly show that CalB can be functionally expressed in *E. coli* and that the attachment of tags does not alter the properties of the lipase.

© 2006 Elsevier B.V. All rights reserved.

**Keywords:** CalB; *Candida antarctica*; Lipase activity; Periplasmic expression; Propeptide

### 1. Introduction

Lipases (EC 3.1.1.3) are enzymes that catalyze the hydrolysis of neutral lipids in biological systems. However many lipases have been found to catalyze a variety

of reactions, which can be very different from the reaction for which the enzyme has evolved to in nature. As these enzymes are naturally acting at an oil–water interface they are, generally, very compatible with organic solvents. Their ability to accept a wide range of substrates (lipids, sugars, alcohols, acids and esters) and their capability to maintain activity and selectivity in organic solvents has enabled their wide use as biocatalysts in industrial applications: In aqueous solvents lipases are used for hydrolyzing esters and in

\* Corresponding author. Tel.: +49 89 21803172; fax: +49 89 21802050.

E-mail address: [Hermann.Gaub@physik.uni-muenchen.de](mailto:Hermann.Gaub@physik.uni-muenchen.de) (H.E. Gaub).

organic solvents they are catalyzing the reverse reaction achieving esterification, transesterification, aminolysis or thioesterification (Anderson et al., 1998; Schmid and Verger, 1998).

Lipase B from *Candida antarctica* (CalB) (Patkar et al., 1992) is one of the most widely used biocatalysts (Anderson et al., 1998). Its structure has been resolved 1994 (Uppenberg et al., 1994, 1995). As many other lipases CalB shows the typical  $\alpha/\beta$  hydrolase fold. Its active site is composed of a Ser-His-Asp catalytic triad. The active site pocket is composed of two channels. The structure of these channels is responsible for the high regio- and stereo-selectivity of CalB towards secondary alcohols (Magnusson et al., 2005). In contrast to other lipases CalB displays no interfacial activation (Overbeeke et al., 2000; Rotticci et al., 2000) and does not possess a typical lid domain (Martinelle et al., 1995; Rotticci et al., 2000).

Because of the importance of CalB in organic synthesis, especially for the kinetic resolution of racemates, numerous approaches have been used to optimize the activity, specificity, selectivity and stability of CalB. This has been achieved either by changing the microenvironment of the enzyme or by optimizing the enzyme itself using random or site-directed mutagenesis. Factors influencing the microenvironment are, for example, supports for immobilization (Fernandez-Lafuente et al., 1998), the content of water in an organic solvent (Piyatheerawong et al., 2004) or the nature of the organic solvent itself (Wescott and Klivanov, 1994; Ottosson et al., 2002). CalB mutants have been generated using site-directed mutagenesis (Patkar et al., 1997; Rotticci et al., 2001; Magnusson et al., 2005), circular permutation (Qian and Lutz, 2005) or directed evolution (Zhang et al., 2003; Suen et al., 2004; Chodorge et al., 2005).

While all cloning steps are always carried out in *Escherichia coli* screening for the desired mutants, in most cases, involves expression in the fungal hosts *Aspergillus oryzae* (Hoegh et al., 1995), *Pichia pastoris* (Rotticci-Mulder et al., 2001) or *Saccharomyces cerevisiae* (Zhang et al., 2003; Suen et al., 2004). In all cases CalB is expressed together with its own (Hoegh et al., 1995) or a host specific signal peptide (Rotticci-Mulder et al., 2001), which directs the lipase to the medium. Following the expression, the supernatant containing the lipase is analyzed for enzymatic activity. The fact that different fungal hosts are used suggests that there

have been problems in expressing CalB in *E. coli*. Only one recent report (Chodorge et al., 2005) describes the use of *E. coli* expressed CalB for a screening assay. However, the improved mutants are not purified and characterized in vitro. The possibility of using *E. coli* expressed CalB directly for screening of the mutants would greatly simplify the process of generating optimized variants. Especially the time span to get from the cloned construct to the functional test of the desired mutant would be much shorter if CalB could be expressed in a functional form in *E. coli*.

Here, we report the soluble expression of CalB in the periplasm of *E. coli*. The influence of the signal and propeptide of CalB was analyzed by sequentially removing these peptides. The possibility of attaching a N-terminal FLAG tag and a C-terminal His tag to allow the use of well-established protocols for purification and detection was investigated. Finally, the specific activity and the kinetic constants of the purified enzymes were compared with a reference sample of CalB expressed in *A. oryzae*.

## 2. Materials and methods

### 2.1. Cloning of expression plasmids

The plasmids for the periplasmic expression of CalB (Fig. 1) are based on the pAK series (Krebber et al., 1997). The plasmid pAK400, which contains a strong RBS, a pelB signal sequence and a His tag, was used. The *NcoI* site in the *cat* gene was removed and an *EcoRI* site was introduced in front of the His tag using site directed mutagenesis. Based on this plasmid (pKB3) three different constructs of CalB were cloned. The *calB* gene was amplified from a plasmid obtained from Novozymes using the following primers: For CalBSP-His the forward primer was chosen such that the signal and propeptide of CalB remain attached to the *calB* gene. For CalBP-His the primer included the sequence of the propeptide. And for CalB-His the sequence of mature CalB was amplified. All forward primers contained the sequence of a short FLAG tag (Knappik and Plückthun, 1994) and a *NcoI* site as in the original pAK400 plasmid. The forward primers had the following sequences: CalBSP\_forw 5'-CATGCCATGGCGGACTACAAAGATATGAAGCTACTCTCTGACCGG-3', CalBP\_forw 5'-CATG

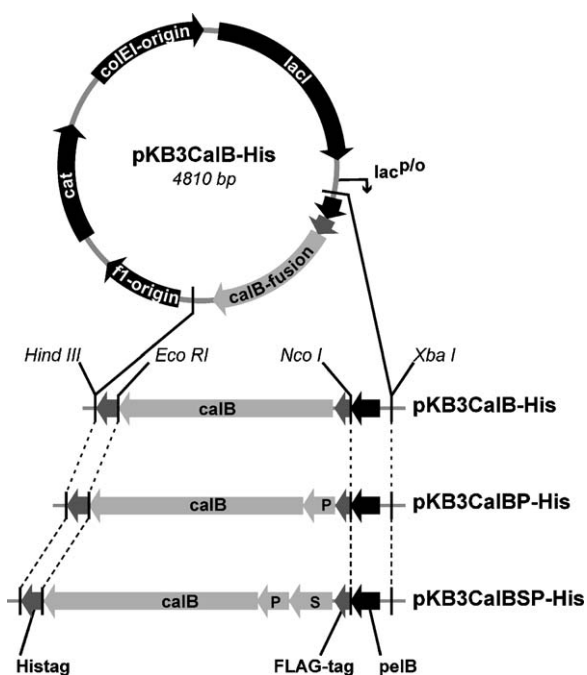


Fig. 1. Plasmids for the periplasmic expression of the different CalB variants. The plasmid is a derivative of the pAK series. It contains a *lac* promoter, the strong RBS T7G10 and the signal peptide pelB. After cleavage of the signal peptide the CalB variants possess a N-terminal FLAG tag in front of the respective *calB* sequence. To obtain the construct pKB3CalBSP-His the *calB* sequence was cloned together with its signal and propeptide. The construct pKB3CalBP-His only contains the propeptide in front of the *calB* sequence. For the construct pKB3CalB-His the sequence of mature CalB was cloned after the FLAG tag. All constructs contain a C-terminal His tag.

CCATGGCGGACTAGAAAGATGCCACTCCTTTG  
GTGAAGC-3', CalB\_forw 5'-CATGCCATGGCGG  
ACTACAAACATCTACCTTCGGTTCGGACC-3'  
(The *Nco*I site is underlined, the sequence of the  
*calB* gene is written in italics.) An identical reverse  
primer introducing an *Eco*RI site after the *calB*  
gene was used for all constructs: CalB\_*Eco*RI\_rev  
5'-CCGGAATTCGGGGGTGACGATGCCG-3'. The  
PCR fragments were purified, cut with *Nco*I and  
*Eco*RI and cloned into the pKB3 plasmid resulting in  
the plasmids pKB3CalBSP-His, pKB3CalBP-His and  
pKB3CalB-His.

## 2.2. Expression of CalB variants

The plasmids encoding the three different variants of CalB were transformed in the *E. coli* K12

strain TB1 (New England Biolabs, Frankfurt, Germany). Small scale expressions for Western blot analysis were performed at 37 or 25 °C and 250 rpm using 50 ml of SB medium (20 g l<sup>-1</sup> tryptone, 10 g l<sup>-1</sup> yeast extract, 5 g l<sup>-1</sup> NaCl, 50 mM K<sub>2</sub>HPO<sub>4</sub>) containing 30 μg ml<sup>-1</sup> chloramphenicol. The cultures for the purification of the lipase variants were grown in 200 ml of SB medium at 25 °C and 250 rpm. These cultures were inoculated from a 20 ml preculture to OD<sub>600</sub> = 0.1. Expression was induced with 1 mM isopropyl-β-D-thiogalactopyranosid (IPTG) at an OD<sub>600</sub> between 1.0 and 1.5. The cells were harvested 3 h after induction by centrifugation at 5000 × g and 4 °C for 10 min.

## 2.3. Western blot analysis

The obtained cell pellets were resuspended in loading buffer (50 mM sodium phosphate pH 8.0, 300 mM NaCl, 10 mM imidazole), normalized to their end OD<sub>600</sub> using 2.5 ml buffer per 1 unit OD<sub>600</sub>. Whole cell extracts were prepared by French Press lysis at 10,000 psi and 1 ml of the crude extract was centrifuged for 60 min at 16,000 × g and 4 °C. The supernatants containing the soluble proteins were transferred to a new vessel and the pellet was resuspended in 1 ml of buffer. These samples were analyzed using anti-FLAG antibody M1 (Sigma, Taufkirchen, Germany) and anti-His antibody Penta-His (Qiagen, Hilden, Germany): SDS-PAGE was carried out under reducing conditions according to standard protocols using 15% polyacrylamide gels. The proteins were transferred to a PVDF membrane (Millipore, Eschborn, Germany). For the detection with the anti-FLAG antibody the membrane was blocked with 5% bovine serum albumin (BSA) in FLAG-Ca<sup>2+</sup> buffer (50 mM Tris/HCl pH 8.0, 10 mM NaCl, 1 mM CaCl<sub>2</sub>) for 30 min. The anti-FLAG M1 antibody was diluted by a factor of 4000 in FLAG-Ca<sup>2+</sup> buffer containing 0.5% BSA and 0.05% Tween 20. The membrane was incubated in this solution for 60 min followed by washing the membrane 3 × 5 min in FLAG-Ca<sup>2+</sup> buffer with 0.05% Tween 20. For detection purposes the secondary rabbit anti-mouse antibody carrying a fluorescence label (Alexa Fluor 647; Invitrogen, Karlsruhe, Germany) was diluted 1:2000 in FLAG-Ca<sup>2+</sup> buffer containing 0.5% BSA and 0.05% Tween 20. After shaking the membrane with this solution for 30 min, the membrane

was again washed three times with buffer. Western blots with the anti-His antibody were carried out using an Alexa Fluor 647 labeled antibody according to the manufacturer's instructions. Fluorescence images were taken using a LS300 scanner (Tecan, Crailsheim, Germany).

#### 2.4. Two-step purification

Cell pellets were resuspended in loading buffer. After adding DNase I (Roche Diagnostics, Mannheim, Germany), cell disruption was achieved by French Press lysis. The suspension was clarified by centrifugation at maximum speed for 60 min at 4 °C and filtration through a 0.22 µm filter. This crude extract was loaded onto a Ni<sup>2+</sup>-NTA column (Qiagen, Hilden, Germany) equilibrated with loading buffer. The column was washed with 30 column volumes of loading buffer and 5 column volumes of a washing buffer (50 mM sodium phosphate pH 8.0, 300 mM NaCl, 30 mM imidazole). Elution was achieved by adding five column volumes of elution buffer (50 mM sodium phosphate pH 8.0, 300 mM NaCl, 200 mM imidazole). The eluted fraction was dialyzed against FLAG-Ca<sup>2+</sup> buffer and loaded onto an anti-FLAG affinity column (M1 antibody; Sigma, Taufkirchen, Germany) equilibrated with the same buffer. The column was washed with 30 column volumes of FLAG-Ca<sup>2+</sup> buffer. The protein was eluted by adding 10 times 2 ml of FLAG-EDTA buffer (50 mM Tris/HCl pH 8.0, 10 mM NaCl, 10 mM EDTA). Finally, the fractions containing the pure enzyme were dialyzed against assay buffer (50 mM sodium phosphate pH 7.0, 150 mM NaCl) and concentrated using Centricon YM-10 (Millipore) to a final concentration of approximately 1 mg ml<sup>-1</sup>. Samples from each step were analyzed by reducing SDS-PAGE using 15% polyacrylamide gels. The actual concentration of the purified lipases was determined by measuring the absorbance at 280 nm. The extinction coefficients of the different CalB variants have been calculated using the program Vector NTI (Invitrogen). Finally, identical amounts of the lipase variants were compared to a glycosylated and deglycosylated sample of CalB from *A. oryzae* using reducing SDS-PAGE. Deglycosylation was carried out using PNGase F (New England Biolabs, Frankfurt, Germany) using the protocol supplied by the manufacturer.

#### 2.5. Activity measurements

To compare the activity of the different CalB variants three different substrates were used: *para*-nitrophenol butyrate (*p*-NPB; Sigma, Taufkirchen, Germany), *para*-nitrophenol laurate (*p*-NPL; Sigma) and carboxyfluorescein diacetate (CFDA; Invitrogen). Before the measurements could take place, calibration curves were determined to correlate the absorption at 405 nm (*p*-NPB and *p*-NPL) or fluorescence at 517 nm (CFDA) with the concentration of the generated product. The extinction coefficient for *para*-nitrophenol determined for the buffer used was 9100 (1 mol<sup>-1</sup> cm<sup>-1</sup>). For the measurements with *p*-NPB and *p*-NPL stock solutions of the substrates were prepared with a concentration of 20 mM in isopropanol. The assay mixture contained 50 mM sodium phosphate pH 7.0, 150 mM NaCl, 0.5% Triton X-100, 5% isopropanol. The following substrate concentrations were used: 1000, 200, 80 and 50 µM. The reaction was started by adding the respective lipase to a final concentration of 100 nM. The temperature was kept constant at 25 °C. The generation of the product could be followed by measuring the increase in absorbance every 10 s for a total time of 300 s. For the CFDA measurements a 25 mM stock solution was prepared in DMSO. The assay mixture contained 50 mM sodium phosphate pH 7.0, 150 mM NaCl, 10% DMSO and 100 nM lipase. The reaction was started by adding CFDA to a final concentration of 1000 µM. Again the temperature was kept constant at 25 °C and the increase in fluorescence was measured for 300 s in time intervals of 10 s. All measurements were carried out in triplicate. Assay mixtures containing BSA instead of lipase were used as reference samples. The increase in absorbance or fluorescence of the BSA samples was subtracted from the values obtained from the lipase samples. These corrected curves were used to calculate the reaction velocity *v*, which describes the concentration of the generated product per minute.

### 3. Results

CalB is an extracellular protein, which contains three disulfide bonds. To allow the correct formation of these disulfide bonds in *E. coli* it is necessary to target the protein to the periplasmic space. Therefore, the *calB*

gene was cloned into an expression plasmid containing a pelB signal sequence, which is recognized from the *E. coli* transport machinery. In its natural host *Candida antarctica* CalB is expressed in form of a preproprotein. Its 18 amino acid long signal peptide targets the protein to the secretory pathway. The function of the seven amino acid long propeptide is not known yet (Hoegh et al., 1995). As nothing is known about the processing of fungal preproteins in *E. coli* three different constructs were cloned as described before (Fig. 1): One construct contains the complete sequence of the preproprotein (CalBSP-His), the second construct misses the signal peptide (CalBP-His) and the third construct represents the sequence of the mature protein (CalB-His). In order to check if the respective peptides are still present at the N-terminus of the expressed protein the sequence of a FLAG tag was attached in front of the respective lipase sequence. In addition, the FLAG tag can be used to investigate if the protein is transported to the periplasmic space correctly (Knappik and Plückthun, 1994): Since the anti-FLAG antibody M1 only binds to the tag if the tag is located at the N-terminus, the protein can be recognized only if the pelB signal peptide is processed during transport to the periplasm. All constructs were cloned with a C-terminal His tag to allow purification and detection of the proteins.

The expression was carried out at 37 and 25 °C. At 37 °C precultures could be grown to a high density over night and the expression cultures reached an OD<sub>600</sub> of 1.0 after 4 h (starting at OD<sub>600</sub> = 0.1). At 25 °C the growth rate was much slower. The precultures needed 48 h and the expression culture had to grow over night before the culture could be induced (data not shown). In both cases the cells grew for another 3 h after the induction took place. The cells were normalized to their end OD<sub>600</sub> and lysed. The soluble and the insoluble fractions were analyzed on Western blots using both anti-FLAG (Fig. 2) and anti-His antibodies (data not shown). Both blots are almost identical and show one strong band of the same size indicating that the three different variants are full-length protein and that the CalB signal and propeptides are not cleaved in *E. coli*. Comparing the amount of soluble and insoluble protein at the different expression temperatures, no protein can be detected in the soluble fractions at 37 °C. In contrast, at 25 °C the soluble fractions of CalB-His and CalBP-His contain a certain amount of soluble protein, which

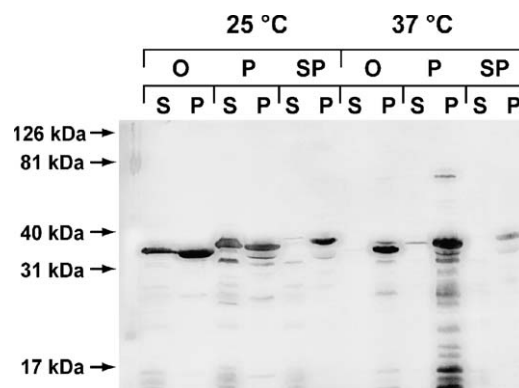


Fig. 2. Anti-FLAG blot showing the expression levels of the CalB variants at 25 and 37 °C. *E. coli* cells expressing the different CalB variants were grown at 25 and 37 °C. The cells were normalized to their end OD<sub>600</sub> and lysed. Soluble proteins (S) were separated from the insoluble fraction (P) by centrifugation. The insoluble fraction was resuspended in the original volume. The same volume of the soluble and the insoluble fraction was loaded onto the gel. The CalB variants contain a N-terminal FLAG tag. The blot shows one major band proving that all variants are translocated to the periplasmic space and that the CalB signal peptide and propeptide are not cleaved by the *E. coli* transport machinery. Except for CalBP-His only little degradation of the proteins occurs. For CalB-His (O) and for CalBP-His (P) soluble protein is detected at 25 °C. CalBSP-His (SP) does not show any soluble expression at this temperature. At 37 °C no soluble expression can be seen for all three variants.

equals the amount of insoluble protein. No expression can be detected for CalBSP-His.

Since CalB-His and CalBP-His are expressed as soluble proteins at 25 °C the next step was to grow larger cultures and purify these two variants of CalB. The most convenient way to purify these proteins was to make use of their His tag and FLAG tag (Fig. 3A and B). The crude extract was loaded onto a Ni<sup>2+</sup>-NTA column to remove most of the contaminants. After dialysis against a buffer containing Ca<sup>2+</sup> the eluted fractions from the Ni<sup>2+</sup>-NTA column were loaded onto the anti-FLAG column. Due to the Ca<sup>2+</sup> dependent binding of the M1 antibody, the protein could be eluted under mild conditions with a buffer containing EDTA. The eluted fractions contain one single band with a size of approximately 35 kDa, which refers to the size of the cloned CalB variants with the two tags. After concentrating the protein preparations, the concentrations were determined by measuring the absorbance at 280 nm. To analyze the purity of these two CalB variants, the same amount of protein was analyzed

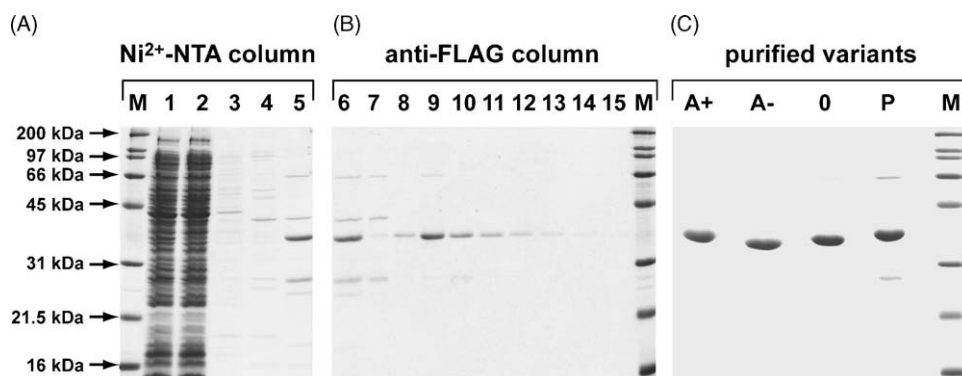


Fig. 3. SDS-PAGE showing the fractions of the two-step purification procedure for CalB-His and the purified lipase variants. (A) For the first step a  $\text{Ni}^{2+}$ -NTA column was used: 1—crude extract, 2—flow through, 3—washing with 10 mM imidazole, 4—washing with 30 mM imidazole, 5—elution with 200 mM imidazole. (B) Fraction 5 was dialyzed against FLAG- $\text{Ca}^{2+}$  buffer, Fraction 6 shows the sample after dialysis. Fraction 6 is loaded onto an anti-FLAG affinity column in the next step. Fraction 7 represents the flow trough, fraction 8 a washing step with FLAG- $\text{Ca}^{2+}$  buffer. Fractions 9–15 represent the eluted fractions using FLAG-EDTA buffer. Fractions 10–15 were pooled for further analysis. (C) The purity of the enzyme variants used for the activity tests (A+: CalB from *A. oryzae*, 0: CalB-His and P: CalBP-His) and of a deglycosylated sample of CalB from *A. oryzae* (A–) was compared using SDS-PAGE. The references from *A. oryzae* (A+ and A–) show only one single band. CalB-His (0) contains a very little amount of other proteins. In the preparation of CalBP-His (P) two other bands are present. The different bands show slight differences in the size of the proteins. It can be clearly seen that P is larger than the version without the propeptide (0). Comparing the size of the variants from *E. coli* (0) and *A. oryzae* (A–), CalB from *E. coli* has a higher molecular weight than the deglycosylated enzyme from *A. oryzae* since it contains a FLAG and a His tag.

by SDS-PAGE. In addition, the size was compared to glycosylated and deglycosylated CalB expressed in *A. oryzae* (Hoegh et al., 1995) without any tags (Fig. 3C). Whereas the preparation of CalB-His is almost pure, the preparation of CalBP-His contains two additional bands. As expected the variants with the attached tags expressed in *E. coli* are bigger than the deglycosylated CalB from *A. oryzae*. CalBP-His is larger than the construct without the propeptide (CalB-His) again proving that the propeptide is still attached to CalBP-His.

Using the preparations previously analyzed by SDS-PAGE the specific activities of the enzymes were determined for three different substrates (Table 1). For CalB from *A. oryzae* the glycosylated enzyme was used. To determine the specific activities the reaction velocities  $v$  at the highest substrate concentration (1000  $\mu\text{M}$ ) were

divided by the amount of enzyme in the reaction mixtures. For all three substrates similar specific activities were obtained for CalB-His and CalB from *A. oryzae*. The specific activity of CalBP-His is a factor of 1.2 lower for all three substrates. This might refer to this particular preparation, which contains a few contaminating proteins. The specific activities for *p*-NPB and *p*-NPL have an error of approximately 10% of the measured value. The error for CFDA is much higher. This is due to the fast auto-hydrolysis of the substrate, which competes with the enzyme-catalyzed reaction.

Therefore, the kinetic constants for the different enzyme variants have been measured only for *p*-NPB and *p*-NPL (Fig. 4). Here the reaction velocity was plotted against the substrate concentration. The data was fitted with the Michaelis–Menten equation to obtain

Table 1  
Specific activities of the different CalB variants

	Specific activity <i>p</i> -NPB ( $\mu\text{mol min}^{-1} \text{mg}^{-1}$ )	Specific activity <i>p</i> -NPL ( $\mu\text{mol min}^{-1} \text{mg}^{-1}$ )	Specific activity CFDA ( $\text{nmol min}^{-1} \text{mg}^{-1}$ )
<i>Aspergillus</i>	$10.52 \pm 1.07$	$0.936 \pm 0.136$	$1.69 \pm 0.37$
<i>E. coli</i> CalB	$10.57 \pm 0.28$	$0.941 \pm 0.075$	$1.58 \pm 0.85$
<i>E. coli</i> CalBP	$8.75 \pm 0.24$	$0.746 \pm 0.048$	$1.30 \pm 0.73$

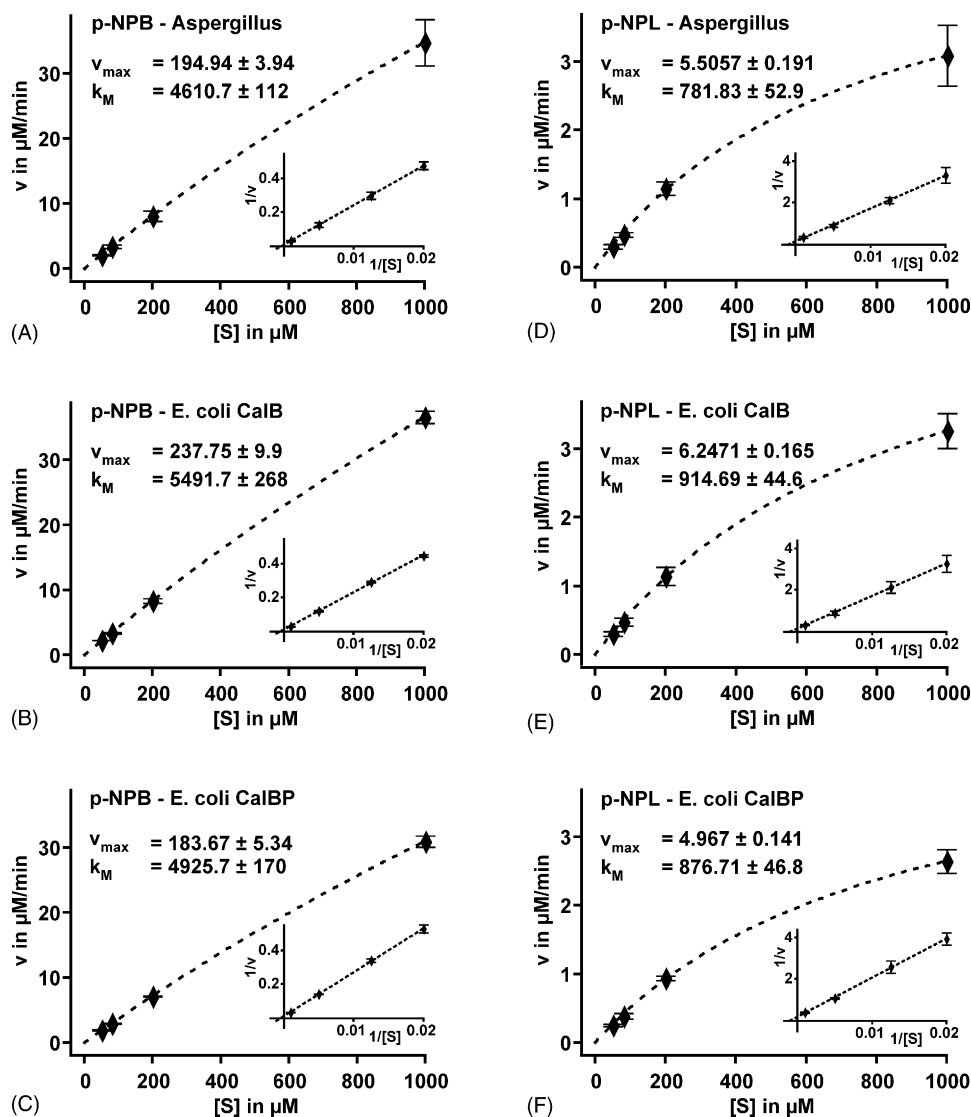


Fig. 4. Michaelis–Menten and Lineweaver–Burk plots for the *p*-NPB and *p*-NPL substrates. The big plots show the Michaelis–Menten plots for the different substrates and enzyme variants. The points (◆) show the measured values with their standard deviation. The dashed line (---) represents the fit using the Michaelis–Menten equation. The small plots show the corresponding Lineweaver–Burk plots. The linearity of the Lineweaver–Burk plots proves that the hydrolysis of the substrates is a first order reaction and therefore the data can be fitted with the Michaelis–Menten equation to obtain the values for  $v_{\max}$  and  $k_M$ . For *p*-NPB (A, B, C) as a substrate the values for  $v_{\max}$  and  $k_M$  differ only slightly for the different enzyme variants. This also applies for the substrate *p*-NPL (D, E, F).

the Michaelis–Menten constant  $k_M$  and  $v_{\max}$ . To determine whether the enzymatic hydrolysis of the different substrates is a first order reaction, the data was analyzed with the Lineweaver–Burk plot. For both substrates, the three different enzyme variants show a straight line in the Lineweaver–Burk plot proving that the reaction is a

first order reaction and therefore the achieved data can be fitted with the Michaelis–Menten equation. Other lipases, which are interfacially activated, do not follow a first order reaction with the *p*-NPL substrate under similar reaction conditions (Redondo et al., 1995).  $k_{\text{cat}}$  and the specificity constant  $k_{\text{cat}}/k_M$  were calculated

Table 2  
Summary of kinetic constants of the different CalB variants

Substrate	Enzyme	$v_{\max}$ ( $\mu\text{M min}^{-1}$ )	$k_M$ ( $\mu\text{M}$ )	$k_{\text{cat}}$ ( $\text{min}^{-1}$ )	$k_{\text{cat}}/k_M$ ( $\text{min}^{-1} \mu\text{M}^{-1}$ )
<i>p</i> -NPB	<i>Aspergillus</i>	194	4612	1949	0.423
	<i>E. coli</i> CalB	237	5492	2378	0.433
	<i>E. coli</i> CalBP	183	4930	2298	0.466
<i>p</i> -NPL	<i>Aspergillus</i>	5.51	781	55.1	0.070
	<i>E. coli</i> CalB	6.25	915	62.5	0.068
	<i>E. coli</i> CalBP	4.97	877	62.1	0.071

based on the obtained values for  $k_M$  and  $v_{\max}$  (Table 2). Having a more detailed look at the data one can see that all constants are in the same range for the different enzyme variants. The specificity constant is the same for all three different enzymes.

#### 4. Discussion

The data clearly shows that CalB can be functionally expressed in *E. coli*. The strategy of lowering the expression temperature from 37 to 25 °C (Baneyx and Mujacic, 2004) yields soluble and functional protein for CalB with or without the propeptide. These variants of CalB from *E. coli* show identical catalytic activity compared with the enzyme from *A. oryzae*. This indicates that the structures of their active sites are the same. In addition, tags can be attached to the N-terminus and to the C-terminus without changing the properties of the enzyme. These tags can be used for detection and purification of the enzyme.

Although CalB has been the subject of intensive research, the function of some important structural features is still not known. The propeptide, as has been shown for proteases (Wiederanders et al., 2003) and the lipase of *Rhizopus oryzae* (Beer et al., 1998), can act as an inhibitor or assist in folding of the protein into its native state. The experiments, which are presented here, could not detect a difference between the variants with and without the propeptide. This data and the fact that propeptides involved in folding are normally much larger (Beer et al., 1998; Wiederanders et al., 2003) lead to the conclusion that the propeptide is not involved in folding. The construct lacking the propeptide can also fold into a native and active conformation. However, for the lipase from *R. oryzae* it has been shown that the enzyme with the propeptide has improved fold-

ing kinetics and a higher stability. We cannot eliminate the possibility of similar contributions of the propeptide since in vitro unfolding and refolding experiments would be necessary to obtain more detailed information. Furthermore, an inhibitory effect of the propeptide principally cannot be excluded since the construct used in this study does not possess the original propeptide because of the presence of the FLAG tag. Based on the data presented here, no conclusion can be drawn about the function of the propeptide. This also applies to the glycosylation. CalB from *E. coli* lacks the glycosylation. However, no difference in the enzymatic activity can be seen compared to the glycosylated enzyme from *A. oryzae*.

Further on it also remains unclear if the enzyme is active within *E. coli*. In the other expression systems used CalB is secreted to the culture medium. In *E. coli* the lipase remains inside the cell and could in principle degrade lipids in *E. coli*. This does not seem to be the case since no difference in growth can be seen when the lipase is expressed in soluble or insoluble form (data not shown). Other lipases possess a lid, which shields the active site from the solvent in an aqueous environment. During contact with a hydrophobic interface, the lipase undergoes a conformational change and the active site becomes accessible. In contrast, CalB does not have a typical lid domain and does not show interfacial activation (Overbeeke et al., 2000; Rotticci et al., 2000). However, Velonia et al. (2005) could show that one enzyme can exist in catalytically active and catalytically inactive conformations. The question if CalB only exists in an inactive conformation in *E. coli* and if this is actively regulated is going beyond the scope of this study.

Having a more detailed look at the kinetic constants for the different substrates, one can see that CalB has a higher specificity constant for *p*-NPB, a short fatty

acid chain. This result is in contrast to other reports in the literature. A similar specificity for C<sub>4</sub> (*p*-NPB) and C<sub>12</sub> (*p*-NPL) fatty acid chains was observed in cyclohexane (Garcia-Alles and Gotor, 1998). Another report describes a preference for fatty acid chains longer than 10 carbon atoms in hexane (Kirk et al., 1992). Since the specificity of the enzyme is dependent on the solvent no conclusion can be drawn from these findings. Probably, the reaction rates for different substrates are not only a matter of specificity of the enzyme but also depend on the solubility of the substrate in the respective solvent. The solubility of the substrate is a critical point for the activity tests, which were performed. The range of concentrations is limited by the detection limit of the generated product and by the solubility of the substrate in the reaction buffer.

The possibility of expressing CalB in *E. coli* opens up new ways for screening and rational design of improved variants. For example, by using phage display (Danielsen et al., 2001; Fernandez-Gacio et al., 2003) a higher number of mutants can be screened in order to obtain the desired molecule. The use of phage display would in addition circumvent the drawback that CalB is expressed intracellularly in *E. coli*. Furthermore, the possibility to make fusion proteins will allow numerous new options for the immobilization of the enzyme. Especially methods for directed immobilization will make the optimization of reaction conditions more reliable since the enzyme will always be immobilized in the same orientation with the active site pointing away from the immobilization matrix. Directed immobilization will also be an important tool for single molecule studies of the enzyme, which can gain further insights of the mechanism how CalB switches between the active and inactive conformations.

### Acknowledgements

The authors thank Novozymes A/S for the gift of the *calB* gene and purified CalB from *Aspergillus*, Andreas Plückthun for the gift of pAK400, Angelika Kardinal for dedicated initial work to this project, Elias Punchner, Michael Skjot, Allan Svendsen, Nikos Hatzakis and Alan Rowan for helpful discussions as well as Gregor Neuert for critically reading the manuscript. This work was supported by the European Union and the Deutsche Forschungsgemeinschaft.

### References

- Anderson, E.M., Larsson, K.M., Kirk, O., 1998. One biocatalyst-many applications: The use of *Candida antarctica* B-Lipase in organic synthesis. *Biocatal. Biotransform.* 16, 181–204.
- Baneyx, F., Mujacic, M., 2004. Recombinant protein folding and misfolding in *Escherichia coli*. *Nat. Biotechnol.* 22, 1399–1408.
- Beer, H.D., McCarthy, J.E.G., Bornscheuer, U.T., Schmid, R.D., 1998. Cloning, expression, characterization and role of the leader sequence of a lipase from *Rhizopus oryzae*. *Biochim. Biophys. Acta* 1399, 173–180.
- Chodorge, M., Fourage, L., Ullmann, C., Duvivier, V., Masson, J.M., Lefevre, F., 2005. Rational strategies for directed evolution of biocatalysts—Application to *Candida antarctica* lipase B (CALB). *Adv. Synth. Catal.* 347, 1022–1026.
- Danielsen, S., Eklund, M., Deussen, H.J., Graslund, T., Nygren, P.A., Borchert, T.V., 2001. In vitro selection of enzymatically active lipase variants from phage libraries using a mechanism-based inhibitor. *Gene* 272, 267–274.
- Fernandez-Gacio, A., Uguen, M., Fastrez, J., 2003. Phage display as a tool for the directed evolution of enzymes. *Trends Biotechnol.* 21, 408–414.
- Fernandez-Lafuente, R., Armisen, P., Sabuquillo, P., Fernandez-Lorente, G., Guisan, J.M., 1998. Immobilization of lipases by selective adsorption on hydrophobic supports. *Chem. Phys. Lipids* 93, 185–197.
- Garcia-Alles, L.F., Gotor, V.V., 1998. Alcohol inhibition and specificity studies of lipase B from *Candida antarctica* in organic solvents. *Biotechnol. Bioeng.* 59, 163–170.
- Hoegh, I., Patkar, S., Halkier, T., Hansen, M.T., 1995. 2 Lipases from *Candida antarctica*—cloning and expression in *Aspergillus oryzae*. *Can. J. Bot.* 73, S869–S875.
- Kirk, O., Björkling, F., Godtfredsen, S.E., Larsen, T.O., 1992. Fatty acid specificity in lipase-catalyzed synthesis of glucoside esters. *Biocatalysis* 6, 127–134.
- Knappik, A., Plückthun, A., 1994. An improved affinity tag based on the FLAG peptide for the detection and purification of recombinant antibody fragments. *Biotechniques* 17, 754–761.
- Krebber, A., Bornhauser, S., Burmester, J., Honegger, A., Willuda, J., Bosshard, H.R., Plückthun, A., 1997. Reliable cloning of functional antibody variable domains from hybridomas and spleen cell repertoires employing a reengineered phage display system. *J. Immunol. Meth.* 201, 35–55.
- Magnusson, A.O., Rotticci-Mulder, J.C., Santagostino, A., Hult, K., 2005. Creating space for large secondary alcohols by rational redesign of *Candida antarctica* lipase B. *Chembiochem* 6, 1051–1056.
- Martinelle, M., Holmquist, M., Hult, K., 1995. On the interfacial activation of *Candida antarctica* lipase-a and lipase-b as compared with *humicola-lanuginosa* lipase. *Biochim. Biophys. Acta* 1258, 272–276.
- Ottosson, J., Fransson, L., King, J.W., Hult, K., 2002. Size as a parameter for solvent effects on *Candida antarctica* lipase B enantioselectivity. *Biochim. Biophys. Acta* 1594, 325–334.
- Overbeeke, P.L.A., Govardhan, C., Khalaf, N., Jongejan, J.A., Heijnen, J.J., 2000. Influence of lid conformation on lipase enantioselectivity. *J. Mol. Catal. B: Enzym.* 10, 385–393.

- Patkar, S., Bjorkling, F., Zundell, M., Schulein, M., Svendsen, A., Hansen, H.H., Gormsen, E., 1992. Purification of two lipases from *Candida antarctica* and their inhibition by various inhibitors. *Indian J. Chem.* 32B, 76–80.
- Patkar, S.A., Svendsen, A., Kirk, O., Clausen, I.G., Borch, K., 1997. Effect of mutation in non-consensus sequence Thr-X-Ser-X-Gly of *Candida antarctica* lipase B on lipase specificity, specific activity and thermostability. *J. Mol. Catal. B: Enzym.* 3, 51–54.
- Piyatheerawong, W., Iwasaki, Y., Xu, X.B., Yamane, T., 2004. Dependency of water concentration on ethanolysis of trioleoyl-glycerol by lipases. *J. Mol. Catal. B: Enzym.* 28, 19–24.
- Qian, Z., Lutz, S., 2005. Improving the catalytic activity of *Candida antarctica* lipase B by circular permutation. *J. Am. Chem. Soc.* 127, 13466–13467.
- Redondo, O., Herrero, A., Bello, J.F., Roig, M.G., Calvo, M.V., Plou, F.J., Burguillo, F.J., 1995. Comparative kinetic-study of lipase-a and lipase-b from *candida-rugosa* in the hydrolysis of lipid *p*-nitrophenyl esters in mixed micelles with triton-X-100. *Biochim. Biophys. Acta* 1243, 15–24.
- Rotticci, D., Norin, T., Hult, K., Martinelle, M., 2000. An active-site titration method for lipases. *Biochim. Biophys. Acta* 1483, 132–140.
- Rotticci, D., Rotticci-Mulder, J.C., Denman, S., Norin, T., Hult, K., 2001. Improved enantioselectivity of a lipase by rational protein engineering. *Chembiochem* 2, 766–770.
- Rotticci-Mulder, J.C., Gustavsson, M., Holmquist, M., Hult, K., Martinelle, M., 2001. Expression in *Pichia pastoris* of *Candida antarctica* lipase B and lipase B fused to a cellulose-binding domain. *Prot. Express. Purif.* 21, 386–392.
- Schmid, R.D., Verger, R., 1998. Lipases: Interfacial enzymes with attractive applications. *Angew. Chem. Int. Ed.* 37, 1609–1633.
- Suen, W.C., Zhang, N.Y., Xiao, L., Madison, V., Zaks, A., 2004. Improved activity and thermostability of *Candida antarctica* lipase B by DNA family shuffling. *Protein Eng. Des. Sel.* 17, 133–140.
- Uppenberg, J., Hansen, M.T., Patkar, S., Jones, T.A., 1994. Sequence, crystal-structure determination and refinement of 2 crystal forms of lipase-b from *Candida antarctica*. *Structure* 2, 293–308.
- Uppenberg, J., Ohrner, N., Norin, M., Hult, K., Kleywegt, G.J., Patkar, S., Waagen, V., Anthonsen, T., Jones, T.A., 1995. Crystallographic and molecular-modeling studies of lipase B from *Candida antarctica* reveal a stereospecificity pocket for secondary alcohols. *Biochemistry* 34, 16838–16851.
- Velonia, K., Flomenbom, O., Loos, D., Masuo, S., Cotlet, M., Engelborghs, Y., Hofkens, J., Rowan, A.E., Klafner, J., Nolte, R.J., de Schryver, F.C., 2005. Single-enzyme kinetics of CALB-catalyzed hydrolysis. *Angew. Chem. Int. Ed.* 44, 560–564.
- Wescott, C.R., Klivanov, A.M., 1994. The solvent dependence of enzyme specificity. *Biochim. Biophys. Acta* 1206, 1–9.
- Wiederanders, B., Kaulmann, G., Schilling, K., 2003. Functions of propeptide parts in cysteine proteases. *Curr. Prot. Pept. Sci.* 4, 309–326.
- Zhang, N.Y., Suen, W.C., Windsor, W., Xiao, L., Madison, V., Zaks, A., 2003. Improving tolerance of *Candida antarctica* lipase B towards irreversible thermal inactivation through directed evolution. *Prot. Eng.* 16, 599–605.

## 9 Curriculum vitae

### Julia Louise Zimmermann

#### Address

Chair for Applied Physics  
Center for Nanoscience  
LMU München  
Amalienstrasse 54  
80799 München  
Germany  
Tel.: +49 89 2180 2306  
Fax.: +49 89 2180 2050  
Email: julia@morfill.de

#### Personal Details

Date of Birth: 18.09.1977  
Place of Birth: Heidelberg  
Name at Birth: Morfill  
Nationality: German  
Marital status: married

#### Education

- |                           |   |
|---------------------------|---|
| <b>05/2005 to present</b> | <b>PhD in Physics</b><br>Chair for Applied Physics (Prof. Dr. Hermann E. Gaub)<br>Ludwig-Maximilians-Universität, Munich/Germany  |
| <b>09/1997 to 04/2005</b> | <b>Diploma in physics</b><br>Ludwig-Maximilians-Universität, Munich/Germany<br><br><b>Diploma thesis:</b> High-resolution single molecule force spectroscopy of double stranded DNA.<br><br>Chair for Applied Physics (Prof. Dr. Hermann E. Gaub)<br>Ludwig-Maximilians-Universität, Munich/Germany |
| <b>1988 to 1997</b>       | St.-Anna grammar school, Munich/Germany   |
| <b>1984 to 1988</b>       | primary school in the Gebelestrasse, Munich/Germany   |

## 10 Acknowledgements

Finally, I want to say “thanks” to a lot of people who have contributed to this work:

### **Prof. Dr. H. E. Gaub**

... for the opportunity to do my thesis in this group  
... for the motivation and many helpful discussions and ideas  
... for a very good “rapper-video” ☺

### **Dr. Kerstin Blank**

... for the perfect and extremely productive collaboration in all our projects  
... for all the biological advice  
... for the really good friendship  
... for the really good time in Munich - I miss you here

### **Dr. Ferdinand Kühner**

... for the good collaboration in the DNA project  
... for many helpful and inspiring discussions

### **Dr. Kay Gottschalk**

... for many discussions regarding the antibody project  
... for the inspiring coffee and “Amerikaner” breaks

### **Julia Sedlmair**

... for the measurements of antibody-peptide interactions  
... for the work on the metal-DNA project, which is not part of this thesis

### **Uta Steinbach**

... for the measurements of antibody-peptide interactions  
... for listening to all my little problems  
... for the really good friendship, which evolved in the last few months

**Robert Lugmaier and Elias Puchner**

... for many helpful discussions and ideas  
... for the nice atmosphere in our little room  
... for not going mad with all my pink stuff

**Jan Neumann**

... for the simulations of the antibody-peptide system

**Dr. Richard Neher und Dr. Ulrich Gerland**

... for the support regarding theoretical problems

**Thomas Nikolaus**

... for the help regarding surface chemistry

**Angelika Kardinal and Verena Thalhammer**

... for the perfect organization of the chemistry lab

**Prof. Dr. A. Plückthun, Dr. Christian Zahnd and Dr. Beatrice Luginbühl**

... for the collaboration in the antibody project

**Julia Schmitz, Katja Falter, Dr. Martin Benoit, Matthias Erdmann (alias Dobby) and Dominik Ho**

... for the nice and informative time in the Gaub lab

**The rest of the gambicrew**

... for the really good working atmosphere

In the end, I want to thank my parents, **Valerie** and **Gregor**, and my brother, **Gary**, who supported me over all the years and who never despaired when I said, that I would like to work as a cashier in ALDI.

I especially want to thank my husband and best friend, **Nikolai**, who always supported and motivated me. I love you.